Czech Technical University in Prague

Faculty of Mechanical Engineering

Doctoral Thesis

Dynamics of Heat Transfer During Cooling of Overheated Surfaces

---

Author

Ing. Jan Stepanek

Supervisor

doc. Ing. Vaclav Dostal, Sc.D.

Consultant

Ing. Vaclav Blaha, CSc.

Doctoral study programme:

Mechanical engineering

Field of study:

Power Engineering

May, 2018

Annotation Sheet

Author	Ing. Jan Štěpánek
English title	Dynamics of Heat Transfer During Cooling of Overheated Surfaces
Czech title	Dynamika přestupu tepla při vychlazování vysoce rozehřátých povrchů
Year	2018
Study programme	Mechanical Engineering / Strojní inženýrství
Field of study	Power Engineering / Energetické stroje a zařízení
Department	Dept. of Energy Engineering / Ústav energetiky
Supervisor	doc. Ing. Václav Dostál, Sc.D.
Consultant	Ing. Václav Bláha, CSc
Counters	Pages: 173

Figures: 86

Tables: 23

Equations: 100

Appendices: 2 |

Čestné prohlášení

Tímto prohlašuji, že jsem tuto disertační práci vypracoval samostatně a pouze za použití literatury uvedené v seznamu.

Statutory Declaration

I declare that I have developed and written the enclosed Doctoral Thesis completely by myself, and I have not used sources or means without declaration in the text.

V Praze dne 4.5.2018   Ing. Jan Štěpánek

Acknowledgments

I would like to thank everyone who supported me during my studies, especially my parents and extended family. My great thanks belong to my supervisor specialist Ing.Václav Bláha,CSc. for his wise advice related to the investigated phenomenon and to my supervisor doc.Ing.Václav Dostál,Sc.D. for overall leadership during my time at university. My special thanks belong to Jana Táborská for her motivation during thesis completion and psychological support in these challenging times.

Poděkování

Rád bych tímto poděkoval všem, kteří mě podporovali během mých studií, především rodičům a širší rodině. Mé velké díky patří mému školiteli-specialistovi Ing.Václavu Bláhovi,CSc. za jeho četné a užitečné rady týkající se zkoumaného jevu a mému školiteli doc.Ing.Václavu Dostálovi,Sc.D. za celkové vedení během mého působení na univerzitě. Mé zvláštní poděkování patří Janě Táborské za její motivaci během sepisování této práce a psychologickou podporu v těchto náročných časech.

Contents

List of Figures

List of Tables

List of Symbols

Symbol	Description	Unit
T_0	Initial wall temperature	$[°C]$
T_{0TC1}	Initial wall temperature at TC1	$[°C]$
T_{0TC2}	Initial wall temperature at TC2	$[°C]$
T_{0TC3}	Initial wall temperature at TC3	$[°C]$
T_{chf}	Critical heat flux temperature	$[°C]$
T_{cool}	Coolant temperature	$[°C]$
T_q	Quenching temperature	$[°C]$
T_g	Silica glass tube temperature	$[°C]$
T_{sat}/T_s	Saturation temperature	$[°C]$
T_{nb}	Nucleate boiling temperature	$[°C]$
T_w	Wall temperature	$[°C]$
T_t'	First order time derivation of temperature	$[°C.s^{-1}]$
T_t''	Second order time derivation of temperature	$[°C.s^{-2}]$
D_{go}	Silica tube outer diameter	$[m]$
D_{gi}	Silica tube outer diameter	$[m]$
D_h	Hydraulic diameter	$[m]$
d	Heated tube outer diameter	$[m]$
A_f	Flow area of annulus	$[m^2]/[mm^2]$
O_w	Wetted perimeter	$[m]$
h	Heat transfer coefficient	$[W.m^{-2}.K^{-1}]$
h_{dry}	Heat transfer coefficient in dry region	$[W.m^{-2}.K^{-1}]$

h_q	Heat transfer coefficient at quench point	$[W.m^{-2}.K^{-1}]$
h_{chf}	Heat transfer coefficient at critical heat flux point	$[W.m^{-2}.K^{-1}]$
h_{1f}	Heat transfer coefficient in wet region	$[W.m^{-2}.K^{-1}]$
h_{qnb}	Heat transfer coefficient between quench and NB point	$[W.m^{-2}.K^{-1}]$
k	Thermal conductivity	$[W.m^{-1}.K^{-1}]$
ρ	Density	$[kg.m^{-3}]$
C	Specific heat	$[J.kg^{-1}.K^{-1}]$
k_q	Thermal conductivity at quenching temperature	$[W.m^{-1}.K^{-1}]$
ρ_q	Density at quenching temperature	$[kg.m^{-3}]$
C_q	Specific heat at quenching temperature	$[J.kg^{-1}.K^{-1}]$
k_{150}	Thermal conductivity at $150\,^{\circ}C$	$[W.m^{-1}.K^{-1}]$
k_{q66}	Thermal conductivity at $0.66T_0$	$[W.m^{-1}.K^{-1}]$
ρ_{q66}	Density at $0.66T_0$	$[kg.m^{-3}]$
C_{q66}	Specific heat at $0.66T_0$	$[J.kg^{-1}.K^{-1}]$
k_{05}	Thermal conductivity at $0.5T_0$	$[W.m^{-1}.K^{-1}]$
ρ_{05}	Density at $0.5T_0$	$[kg.m^{-3}]$
C_{05}	Specific heat at $0.5T_0$	$[J.kg^{-1}.K^{-1}]$
C_g	Specific heat of silica glass	$[J.kg^{-1}.K^{-1}]$
ρ_g	Density of silica glass	$[kg.m^{-3}]$
u	Quench front velocity	$[m.s^{-1}]/[cm.s^{-1}]$
u_{12}	Mean quench front velocity TC1 to TC2	$[m.s^{-1}]/[cm.s^{-1}]$
u_{23}	Mean quench front velocity TC2 to TC3	$[m.s^{-1}]/[cm.s^{-1}]$
u_{13}	Mean quench front velocity TC1 to TC3	$[m.s^{-1}]/[cm.s^{-1}]$

U	Relative quench front velocity	$[-]$
G	Initial coolant mass flux	$[kg.m^{-2}.s^{-1}]$
G_{err}	Coolant mass flux error	$[kg.m^{-2}.s^{-1}]$
f	Flow meter frequency	$[Hz]$
r	Electrical resistance	$[\Omega.mm^2.m^{-1}]$
P_{in}	Welder output / Test section power input	$[W]$
U_{weld}	Welder el. voltage	$[V]$
I_{weld}	Welder el. current	$[A]$
I_{max}	Max. el. current at pressure measurement	$[A]$
I	El. current in heated tube	$[A]$
U_{press}	Voltage at pressure measurement	$[V]$
R_{press}	Electrical resistance at pressure measurement	$[\Omega]$
p_{relM}	Measured relative pressure	$[Pa]$
p_{corr}	Pressure correction	$[Pa]$
p_{rel}	Calibrated relative pressure	$[Pa]$
p_{max}	Maximum measurable pressure	$[Pa]$
p_h	Hydrostatic pressure	$[Pa]$
δp_{hstat}	Hydrostatic pressure drop	$[Pa]$
δp_{cold}	Cold section pressure drop	$[Pa]$
g	Gravitational acceleration	$[m.s^{-2}]$
$\dot{Q}$	Coolant flow rate	$[lpm]$
$\dot{Q}_{err}$	Coolant flow rate error	$[lpm]$
δ_{fr}	Relative coolant flow rate error	$[\%]$

q''	Heat flux	$[W.m^{-2}]$
δ	Wall thickness	$[m]$
Re	Reynolds number	$[-]$
Pr	Prandtl number	$[-]$
Bi	Biot number	$[-]$
Pe	Peclet number / Dimensionless quench front velocity	$[-]$
ν	Kinematic viskosity	$[m^2.s^{-1}]$
Θ	Dimensionless temperature	$[-]$
Θ_q	Modified dimensionless temperature	$[-]$
W_l	Window length for Savitzky-Golay filter	int
N_s	Number of nodes in filtered data sample	int
D_f	Degree of Savitzky-Golay filter	int
t	Time	$[s]$
t_{ichf}	Critical heat flux time at TCi	$[s]$
t_{inb}	Nucleate boiling time at TCi	$[s]$
Δt	Time step size	$[s]$
Δt_{ij}	Time interval between quenching of TCi and TCj	$[s]$
L_h	Heated length	$[m]$
L_{ij}	Pitch between TCi and TCj	$[m]$
L_{hi}	Heated length 0 to TCi	$[m]$
c_{in}	Coolant inlet velocity	$[m.s^{-1}]$
z	Axial position	$[m]$
Δz	Height of node	$[m]$

A_z	Axial cross-sectional area of heated tube	$[m^2]$
q_n	Conducted heat in the "North" direction	$[W]$
q_s	Conducted heat in the "South" direction	$[W]$
q_e	Internal node heat source	$[W]$
q_c	Removed heat by coolant from node	$[W]$
Q_c	Removed heat flux by coolant from node	$[W.m^{-2}]$
Q_g	Heat flux through silica glass tube	$[W.m^{-2}]$
A_o	Outer surface of the node	$[m^2]$
P_e	Internal heat source	$[W.m^{-3}]/[MW.m^{-3}]$
P_{e0}	Initial internal heat source	$[W.m^{-3}]/[MW.m^{-3}]$
P_{e0AB}	Initial internal heat source of models A and B	$[W.m^{-3}]/[MW.m^{-3}]$
P_{e0C}	Initial internal heat source of model C	$[W.m^{-3}]/[MW.m^{-3}]$
ΔH_{ij}	Enthalpy increase between TCi and TCj	$[J.kg^{-1}.K^{-1}]$

Abbreviations

Abbreviation	Meaning
1-D, 2-D	One-Dimensional, Two-Dimensional
BC	Boundary Conditions
CHF	Critical Heat Flux
DAS	Data Acquisition System
DC	Direct Current
ECCS	Emergency Core Cooling System
HBIM	Heat Balance Integral Method
HTC	Heat Transfer Coefficient
IAPWS	International Association for the Properties of Water and Steam
LB-LOCA	Large Break - Loss Of Coolant Accident
LOCA	Loss of Coolant Accident
MAE	Mean Absolute Error
PCHIP	Piecewise Cubic Hermite Interpolating Polynominal
PPL	Pulses Per Liter
PPR	PolyPRopylene
QF	Quench Front
QFV	Quench Front Velocity
RMAE	Relative Mean Absolute Error
RPM	Revolutions Per Minute
TC	Thermocouple

Abstract

Quenching phenomenon is one of the most unexplored phenomena in the field of heat transfer. However, quenching is known for a long time especially due to metal hardening. In the several last decades, the phenomenon has come to the fore of interest in connection with nuclear reactor safety and cryogenic technologies. Quenching is defined as an onset of rapid temperature decrease within cooled geometry by relatively cold liquid. The contact between cooled surface and coolant is not a straightforward process. If the surface temperature is high enough, liquid can't touch the surface directly, but it is separated by stable vapor layer. The layer acts as a thermal insulation barrier and the resulting heat transfer is very limited until surface temperature fails bellow so-called Leidenfrost temperature. The actual value of quenching temperature is influenced by many factors such as dynamics of the coolant, initial wall temperature, material properties of cooled geometry, etc.

An experimental loop with an annular flow channel has been built in order to deepen the knowledge on the quenching phenomenon. The flow channel is vertical and it is equipped with changeable electrically heated tubes (models) with the outer diameter of $9\,mm$ and length over $1.7\,m$ in three different geometrical configurations: Model A - wall thickness (δ) $0.5\,mm$, Model B - $\delta = 1.0\,mm$ and Model C with variable wall thickness. Each model was exposed to bottom flooding at initial wall temperature levels from $250\,°C$ to $700\,°C$ and with four different coolant mass fluxes for each temperature level ($80, 110, 190, 270\,kg.m^{-2}.s^{-1}$).

Results show the complexity of the phenomenon for given configurations and initial experiment parameters. Correlations for all important points in the process were developed i.e. correlations for quenching, critical and nucleate boiling temperature. Another part of the study is suggestion of heat transfer coefficients for the three-regional rewetting model. On top of that correlations for local heat transfer coefficients were proposed. There is also pointed out the effect of pressure pulsation during the flooding and its influence on the process. All these results together with raw experimental results can serve as an input for further investigations of the phenomena and for nuclear reactor safety analyses.

Keywords

Abstrakt

Jevy provázející smáčení vysoce rozehřátých povrchů jsou jedněmi z nejméně prozkoumaných jevů z oblasti přenosu tepla. Tyto procesy jsou jako takové známé již dlouhou dobu především díky tepelnému zpracování kovů (angl. quenching). V posledních několika dekádách se tento jev dostal do popředí zájmu především ve spojení s bezpečností jaderných reaktorů a kryogenní technikou. Smáčení je definované jako počátek prudkého poklesu teploty chlazeného objektu, který je způsobený kontaktem s relativně chladným chladivem, např. vodou. Přímý kontakt mezi rozehřátým povrchem a chladivem však není přímočarý proces. Pokud je teplota povrchu dostatečně vysoká, je kapalina oddělena od povrchu parní vrstvou, která brání přímému kontaktu povrch-chladivo. Tato parní vrstva se chová jako tepelně izolační vrstva a přestup tepla je tak značně snížen až do okamžiku, kdy teplota povrchu poklesne pod tzv. Leidenfrostovu teplotu, při které dojde ke kolapsu parní vrstvy. Vlastní hodnota této teploty je závislá na mnoha faktorech, jako například dynamice chladiva, počáteční teplotě povrchu, vlastnostech chlazeného objektu, geometrii, atd.

Za účelem prohloubení znalostí o tomto jevu bylo postaveno experimentální zařízení s anulárním průtočným kanálem. Testovací kanál má výšku přes $1.7\,m$ a je vybaven měnitelnými průchodem elektrického proudu vyhřívanými modely (trubkami) s vnějším průměrem $9\,mm$. Tyto modely byly použity ve třech variantách: Model A s tloušťkou stěny (δ) $0.5\,mm$, Model B - $\delta = 1.0\,mm$ a Model C s proměnnou tloušťkou stěny po výšce. Každý model byl vystaven sérii experimentů se zaplavováním zdola na počátečních tepelných hladinách povrchu od $250\,^{\circ}C$ do $700\,^{\circ}C$ se čtyřmi různými průtoky chladiva $80, 110, 190, 270\,kg.m^{-2}.s^{-1}$.

Výsledky ukazují komplexní charakter daného jevu pro danou konfiguraci a parametry. Byly vytvořeny korelace pro všechny důležité body v procesu smáčení, tj. korelace pro teplotu smočení, teplotu kritického tepelného toku a teplotu bublinkového varu. Další částí studie je návrh součinitelů přestupu tepla pro tří-oblastní model smáčení. Navíc jsou zde předloženy korelace pro lokální součinitele přestupu tepla. Poukázáno je ve studii také na efekt tlakových pulzací během zaplavování a jejich vliv na daný proces. Všechny tyto výsledky společně s naměřenými daty mohou sloužit jako vstup pro další studie zaměřené na tento jev, popřípadě pro bezpečnostní analýzy jaderných reaktorů.

Motivation and Thesis Goal

Cooling of overheated surfaces also known as quenching is still not well-known. It is a very chaotic transition process where every new experimental study is an important piece of the puzzle on the way to fully understand the phenomenon. The motivation for this study is to propose a detailed view on the quenching phenomenon, specifically bottom reflooding of an annular channel with a heated model of nuclear fuel pin. The result can serve as an input for other analytical studies in the field and it can point out several side effects accompanying the process of reflooding. These outputs can improve predictions of processes where quenching takes place, especially processes related to LOCA accident in nuclear reactor safety analyses.

The main goal of the study, in order to fulfill the motivation, is to collect quality experimental data using a new suitable experimental device with changeable test section. The changeable test section will allow to cover not only one geometry (i.e. wall thickness), but several geometries. These geometries, hand in hand with wide range of initial wall temperatures and coolant flow rates, will hopefully provide a complex view on the process.

Chapter 1

Rewetting

This chapter contains a description of quenching and rewetting phenomenon from the physical point of view and also from the perspective of nuclear reactor safety. Understanding of presented principles is crucial for a deeper understanding of the phenomenon.

1.1 The Rewetting Phenomenon

The quenching phenomenon is known to mankind for many centuries and it is still not too well-known. This phenomenon is known in many technical applications. Nowadays the quenching is under intense research not only from a metal processing point of view, where we need short times of surface cooling for unstable hard crystal structures near the surface but more and more the quenching research is crucial for nuclear reactor safety and for cryogenic applications.

The main difficulty in the quenching of hot surfaces with subcooled coolant is that the cooled surface is not in contact with coolant instantly, but the surface and the coolant are separated by vapor layer. The layer is generated by intense boiling of coolant near the cooled surface. The vapor layer prevents the intense heat transfer to the coolant due to its low density and conduction ability. Because of this, the hot surface is insulated from the coolant by heat insulating layer of vapor. This effect is shown in Figure 1.1. In this case, the surface is cooled down relatively slowly.
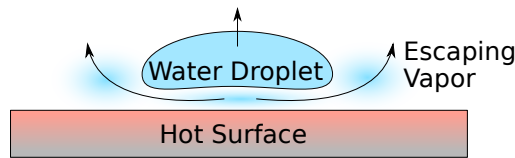
Figure 1.1: Water droplet floating over hot surface due to vapor layer

When the surface temperature falls below the so-called Leidenfrost temperature, the vapor layer collapses and liquid meets the surface. At this moment a high heat transfer rate takes place and the surface is cooled down much more effectively. The physical process when the vapor layer collapses and liquid rewetts the surface is called rewetting. The temperature at which rewetting can be observed (Leidenfrost temperature) is a function of its initial temperature, cooled geometry, coolant flow rate, a temperature of the coolant, surface roughness, etc. [1] The interface between the rewetted surface and still dry surface is called a quench front. As the rewetted part of geometry is effectively cooled, the heat accumulated in front of the quench front is conducted towards the rewetted region. This conduction generates a precooled dry region and this region can be rewetted in the next moment. This conduction and partially sputtering (precursory cooling) represent a mechanism for quench front propagation along the cooled surface. A velocity of the quench front propagation is called quench front velocity. The quench front velocity and its dynamics for different geometries, temperature ranges and coolants are main goals of the research worldwide. A physical model of conduction-controlled rewetting with typical temperature profile and supplemented with one of analytical heat transfer profiles [2] is shown in Figure 1.2.
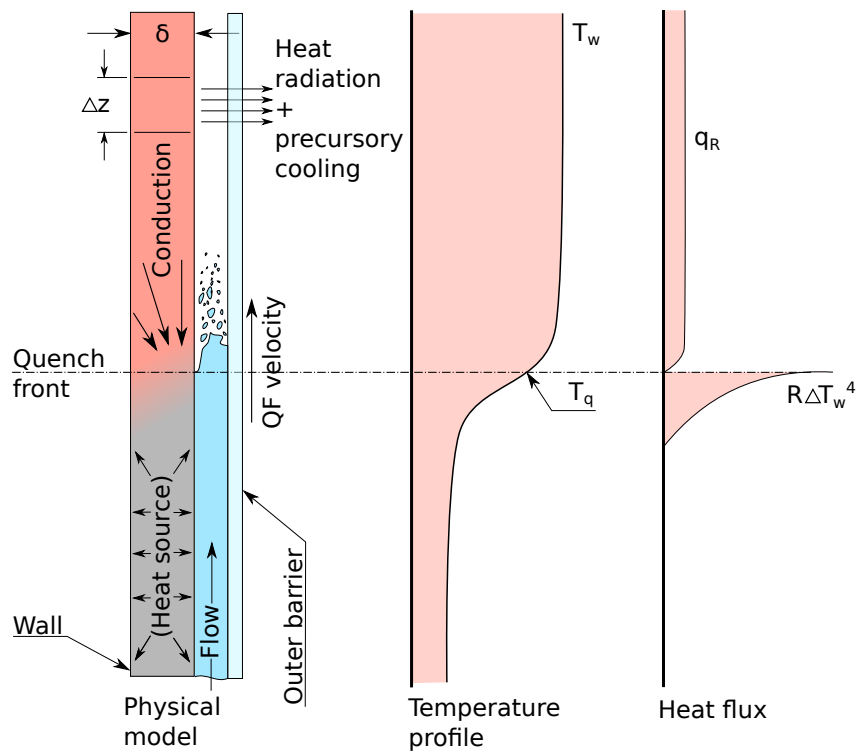
Figure 1.2: Physical model of conduction-controlled rewetting phenomenon for bottom flooding

1.2 Interaction of the Coolant and the Hot Surface Regimes

In the year 1986 Groenveld and Snoek [3] introduced six basic configurations of rewetting of hot surfaces. From their definitions, we have got several possible regimes. These regimes are:

- Top flooding

- Bottom flooding

- Vapour layer collapse

- Rewetting followed by disperse cooling

- Rewetting of horizontal surface by Leidenfrost cooling

- Collapse of film during pool boiling

In a nuclear reactor we can assume, corresponding to reactor design, three possible coolant inlet configurations:

- Top flooding

- Bottom flooding

- Horizontal flooding

These three regimes are described bellow.

1.2.1 Top Flooding

A coolant is fed from top to the cooled object in the case of top flooding. Previous experiments have shown, that axially advancing quench front is characterized by nearly constant quench front velocity. There is a high temperature gradient between dry and wet region due to a high axial heat conduction. The rewetting process is primarily controlled by axial conduction in this case. This process is also known as conduction controlled rewetting. Also, several types of boiling regimes can be observed during the top flooding. The case of top flooding can be seen in Figure 1.3.
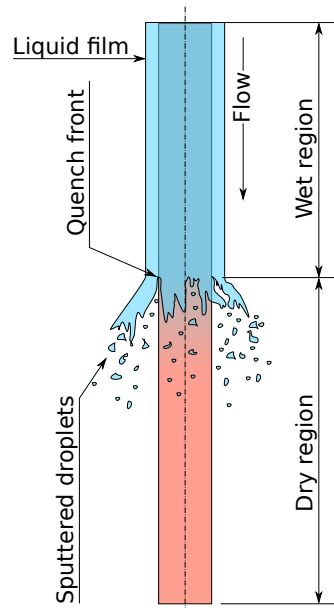
Figure 1.3: Top flooding

1.2.2 Bottom Flooding

A coolant is fed from the bottom into test section and the coolant advances upwards along the geometry in this case. Besides the axial conduction, this process is also characterized by complex hydrodynamics and by given geometry of flow cross-section of the test section. The bounded flow area prevents loss of droplets and they can touch and precool

the surface consequently. The bottom flooding is the main regime of rewetting present during the reflood phase of LOCA accident and this regime is the investigated subject of this thesis. Figure 1.4 shows the typical case of bottom flooding.
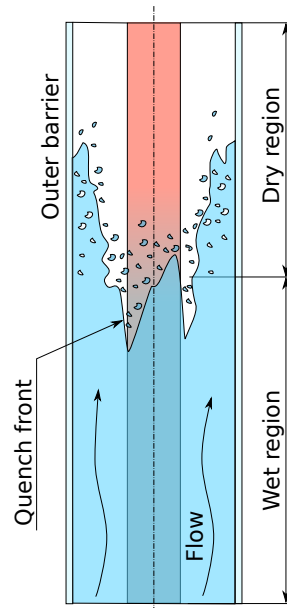
Figure 1.4: Bottom flooding in annular channel

1.2.3 Horizontal Flooding

In the case of horizontal flooding, a coolant is fed into flow channel horizontally, e.g. the axis of the cooled geometry and axis of the flow channel are both horizontal. The basic characteristics of this configuration is a stratification of flow forced by gravity. This flooding regime is shown in Figure 1.5.
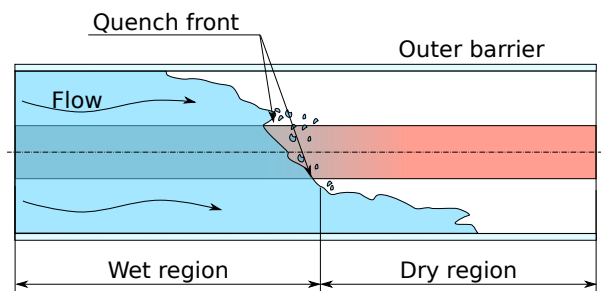
Figure 1.5: Horizontal flooding

1.3 Boiling Curve

Boiling of any liquid is a process at which liquid changes its phase from the liquid state into the gaseous phase. The beginning of the phase change is called boiling point and this point is defined by temperature and pressure. If the liquid temperature reaches its saturation temperature for given pressure, the vapor pressure of the liquid is equal to surrounding pressure. This is the reason, why liquid begin to expand into the gaseous phase. The boiling point can be also considered as a maximum temperature of liquid without the presence of vaporization.

In the year 1934 Shiro Nukiyama [4] proposed a dependence of heat flux from the heated wall into the water on the temperature difference between wall temperature and coolant temperature during boiling. The dependence is shown in Figure 1.6 and it is called - boiling curve.

Figure 1.6 contains several important points along the boiling curve. At the beginning of the coordinate system, there is wall temperature almost equal to the saturation temperature of water and heat flux is minimal. Natural single-phase convection takes place up to point A. A nucleate boiling is present between points A and C. This region is characterized by the rapid increase of heat flux i.e. increase of heat transfer coefficient, due to the improved circulation of the coolant caused by detaching and rising bubbles. Moreover, this region can be divided into two sub-regions. In the first one between points A and B, bubbles released from the surface enter surrounding liquid and implode due to insufficient conditions for boiling. In the second sub-region between points B and C, boiling conditions are met in the whole volume and bubbles can reach the free surface. The maximum value of heat transfer coefficient is located at point C. Beyond this point, newly born bubbles are getting bigger and they merge together. The connection of bubbles creates heat insulating areas and heat flux decreases. The decrease continues up to point D, which is called Leidenfrost point. At this point overheating of the surface, compared to the saturation temperature of water, is high enough to maintain continuous vapor layer. The vapor layer prevents water to cool the surface and wall overheating rises. There is no solid-liquid contact beyond this point and heat transfer is mediated by vapor and heat radiation.
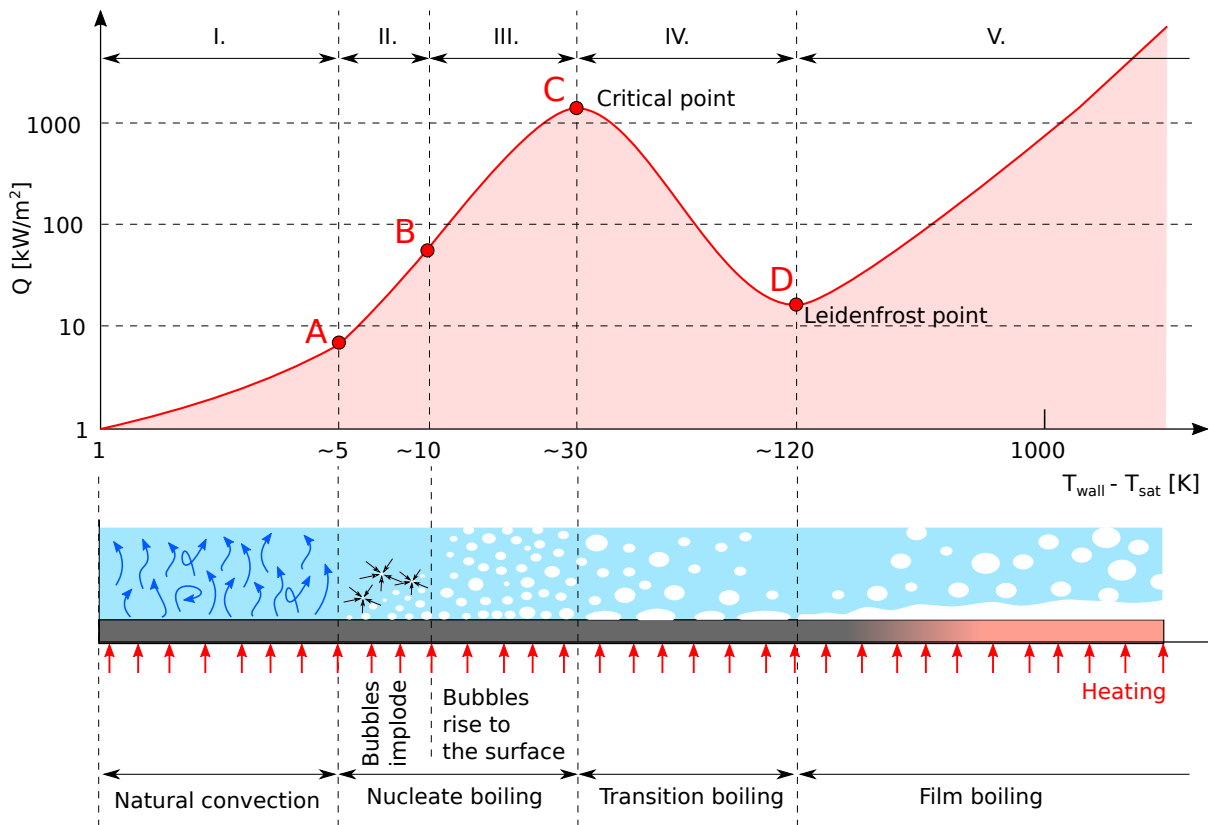
Figure 1.6: Pool boiling curve for water at atmospheric pressure with boiling regimes

1.4 Quenching and Rewetting Temperatures

There is no clear single definition of quenching and rewetting temperature in experimental efforts on the rewetting phenomenon. In general, the rewetting temperature is the maximum temperature which allows solid-liquid contact between the coolant and cooled wall. This definition is in agreement with Leidenfrost point from Figure 1.6 on page 27. We can find three definitions of rewetting and quenching temperature in literature:

1. Quenching and rewetting temperatures are one and the same temperature. The temperature is defined by maximum temperature decrease, i.e. the maximum of the first order derivative (Figure 1.7 point C)

2. Quenching and rewetting temperatures are one and the same temperature. The temperature is defined by the intersection of film boiling slope and transition boiling slope (Figure 1.7 point D1)

3. Quenching temperature is defined by intersection of film boiling slope and transition boiling slope (Figure 1.7 point D1) and rewetting temperature is defined by maximum of the first temperature derivative (Figure 1.7 point C)
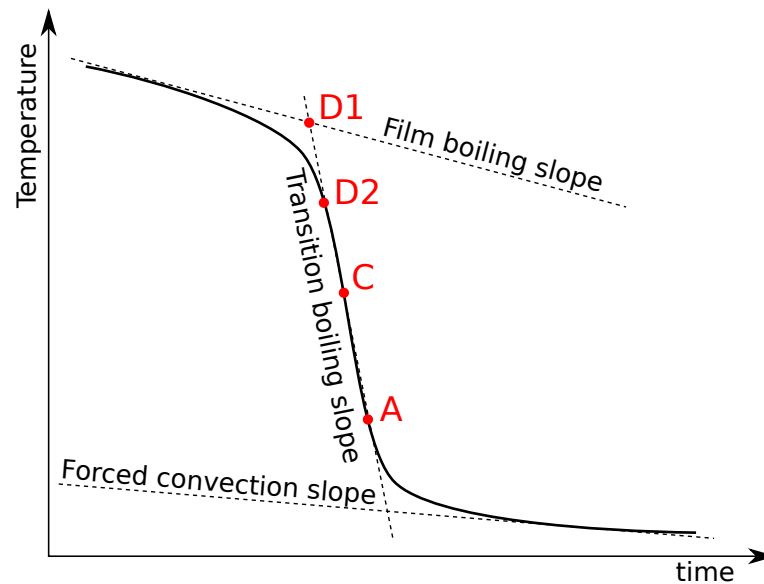
Figure 1.7: Positions of quenching and rewetting temperature

Note: Point letters correspond to boiling curve in Figure 1.6 on page 27

A modification of the last definition is adopted in this work. The last mentioned definition uses the intersection of two tangent lines as described above. This approach can be considered as a semi-graphical method and it is quite simple. The main reason for usage of this method can be probably historical because the semi-graphical approach doesn't need advanced numerical solutions and can be easily found even on paper. On the other hand, the resulting temperature simply does not lie on the temperature profile and thus it can't be physically correct.

For this reason, the quenching temperature is defined by the minimum value of the second order derivative of temperature profile (Figure 1.7 point D2). This method proved to be reliable and its justification is described in chapter 1.4.1 bellow and in results consequently.

The temperature defined through the maximum value of the first derivative (Figure 1.7 point C) represents temperature where heat transfer coefficient reaches its maximum value according to boiling curve. At this point, transient boiling passes into nucleate boiling.

Point A in Figure 1.7 represents temperature on the interface between nucleate boiling and forced convection region. This temperature is found, analogously to quenching temperature, through the maximum value of the second order derivative of the temperature profile.

1.4.1 Preliminary Verification Calculation

A simple two-dimensional transient calculation, in order to test the hypothesis of the minimum second derivative for quenching temperature, has been performed. In this calculation, a geometry was defined as a tube with outer diameter of $9\,mm$ and the wall thickness of $0.5\,mm$. The length of the domain was $40\,mm$ The internal heat source was set to $15.5\,MW.m^{-3}$. Temperature properties of the tube were taken as the same as for the other calculations, i.e. properties of Monel K-500 stainless steel.

Initial conditions were: initial wall temperature $600\,°C$, the temperature of the first line of nodes was $20\,°C$ for the quenching start-up.

The case was solved numerically as thee-regional geometry, where the first region is cooled by steam, the second region is cooled by saturated steam-water mixture and the last one is cooled by relatively cold water. Boundary conditions (BC) were as follows:

- Adiabatic condition at inner tube wall

- 1st (dry) region: temperature of the steam $100\,°C$; $600\,°C > T_w > 450\,°C \Rightarrow$ $h_1 = 100\,W.m^{-2}.K^{-1}$

- 2nd (quenching) region: temperature of the steam/water $100\,°C$; $450\,°C > T_w > 200\,°C \Rightarrow h_1 = 4000\,W.m^{-2}.K^{-1}$

- 3rd (forced convection) region: temperature of the water $35\,°C$; $200\,°C > T_w \Rightarrow$ $h_1 = 500\,W.m^{-2}.K^{-1}$

Note: The values are estimates based on later experience

Resulting temperature profiles, obtained by numerical probes at positions $10\,mm$, $20\,mm$ and $30\,mm$ from temperature array during iteration process, are shown in Figure 1.8. A boundary condition switches can be easily identified on these profiles due to the sudden change of the profile slope. It is evident, that the first boundary condition switch takes place at the end of the upper rounded part. This rounding is caused by axial and radial heat conduction. This is evidence, that this mechanism is responsible for quenching temperature achievement and resulting temperature decrease is ended by quenching onset. Analogously, the second boundary condition switch can be found at the second given temperature level, right at the maximum second derivative value position.
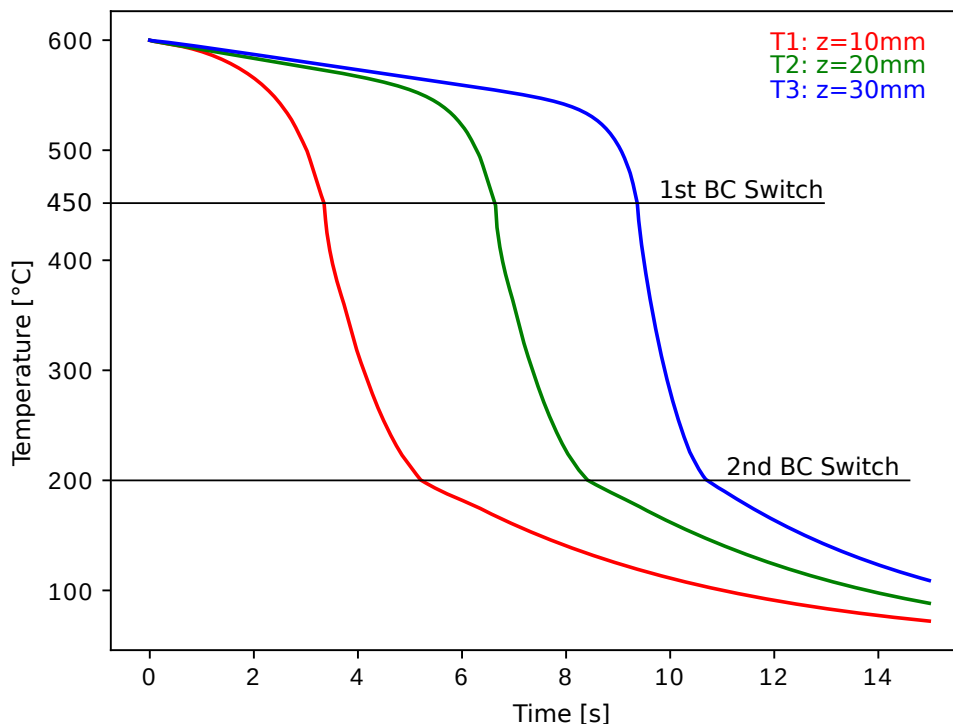
Figure 1.8: Resulting temperature profiles from preliminary calculation

1.5   Basic Heat Transfer Regimes

In general, heat transfer description can be approached in two ways. In the first approach we can examine a given spatial point and at this point, we can describe investigated parameters chronologically. The chronological point of view is actually a resulting process description obtained from experimental setup, where the test section is equipped with thermocouples and chronological data are scanned by data acquisition system. In the second approach we can examine the whole geometry at a given time, i.e. we get a spatial view of the process along the geometry.

We can look at the temperature profile in Figure 1.9 as at a reversed boiling process described in Section 1.3.

In the following description we will start at point G (in Figure 1.9 on page 31) with initial wall temperature T_0. Far enough from advancing quench front, there is completely dry region cooled by heat radiation (if wall temperature is high enough) and by vapor generated at the quench front and escaping at high speed through the flow channel. Precursory cooling region (points F - E) is located in front of the quench front and its range depends on initial wall temperature and actual flow rate because more intense

boiling produces more droplets with higher momentum. Heat is removed by sputtered droplets and vapor in its region. A film boiling region is present closer to quench front (points E - D). The wall temperature is still high enough to maintain continuous vapor layer between the wall and coolant. This region ends with point D, where stable vapor film collapses. The point D corresponds to the Leidenfrost point from boiling curve and at this point, the quench front is located. As the vapor layer collapses, transient boiling takes place between points D and C. Point C represents the critical point, which represents the border between transient and nucleate boiling. Heat transfer coefficient reaches its maximum value at this point and thus the temperature profile first derivative has the maximum negative value here. Beyond the point C, a nucleate boiling regime can be observed on short distance behind the front. Actually, it is very difficult to recognize by eye the difference between transition and nucleate boiling during the reflood process. Once the wall temperature is close to saturation temperature T_{sat}, a single-phase forced convection takes place (beyond the point A). The last point 0 represents the state, where the wall temperature is slightly higher than coolant temperature T_{cool} and removed heat is equal to heat generated within the wall, i.e. steady state is established.

Depending on initial wall temperature and coolant flow rate, these regions and corresponding boiling regimes can be more or less evident.
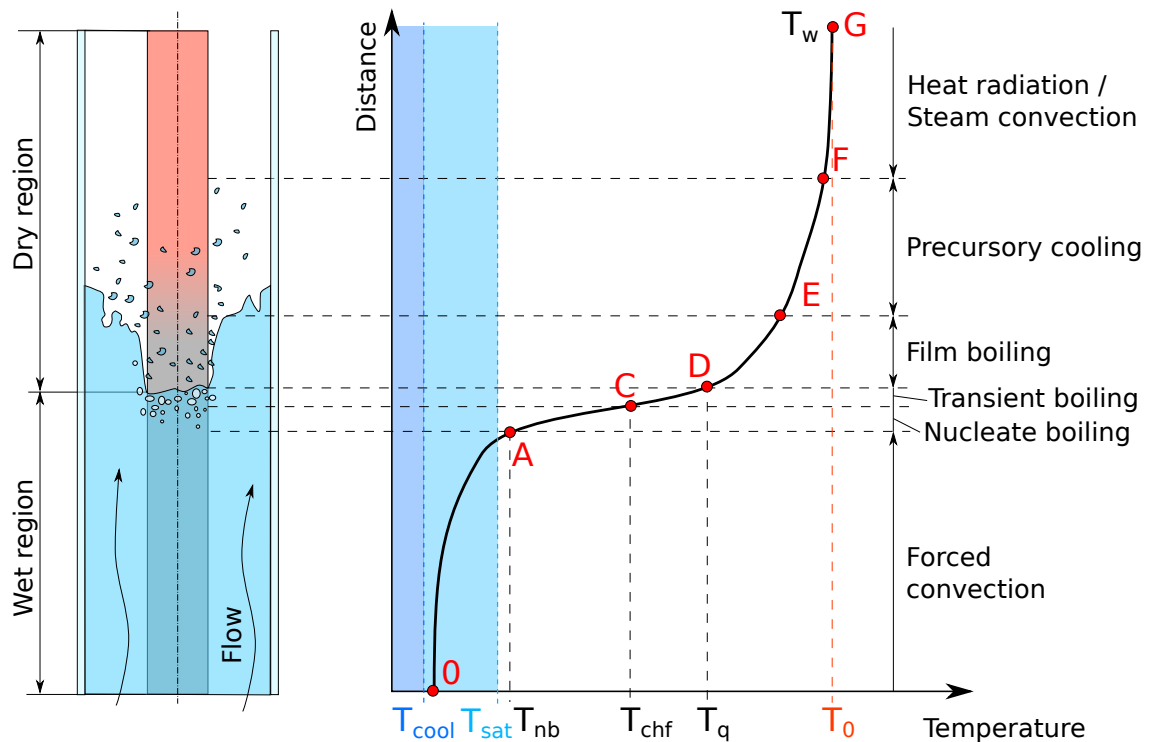
Figure 1.9: Typical temperature profile for bottom flooding at fixed time

Note: Point letters correspond to boiling curve in Figure 1.6 on page 27

1.6   Decay Heat

Heat is generated in a nuclear reactor through fission of heavy nucleus of Uranium 235 or Plutonium 239. Decay heat is generated by unstable fission products. These products decay even when the reactor is shut down and this decay releases additional heat energy. This decay heat is responsible for the post-accidental heating of the reactor core. Because the decay heat is an integral part of the post-operational state of every nuclear reactor, it must be calculated with this effect in post-accidental conditions. Decay heat power as a function of time after reactor shutdown is shown in Figure 1.10.
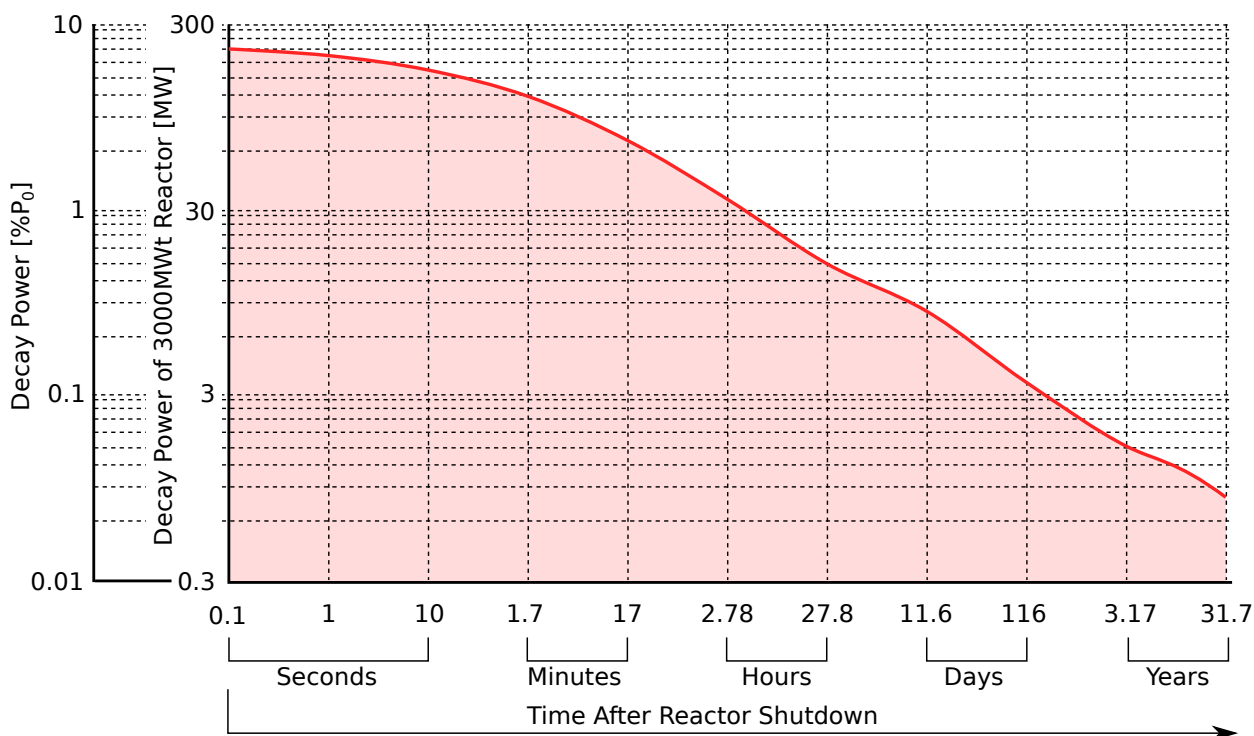
Figure 1.10: Decay Heat power as a function of time after shutdown [5]

From the perspective of bottom reflood process, the decay heat is responsible for high initial cladding temperature and for possible core meltdown subsequently. In the basic model, the decay heat source is assumed as spatially uniform.

There are three possible regimes during the bottom flooding process:

- Heat flux is subcritical and the quench front moves upward. The coolant inlet mass flow rate is high enough to cool down the surface and to advance forward.

- Heat flux is critical and quench front stops. The amount of generated vapor on the surface is equal to inlet mass of coolant and the internal heat source is high enough to keep the quench front static.

- Heat flux is supercritical and quench front moves downward - toward the inlet. In this case, the evaporated amount of coolant is higher than its inlet mass flow rate.

1.7 Precursory Cooling

There is a clear interface between a wet region and a dry region at low quenching velocities. A growing two-phase region in front of the quench front can be observed with rising Peclet number (rising quench front velocity). The two-phase region is generated by unrestrained processes at the interface, where a part of the liquid is thrown forward by boiling liquid and escaping vapor. This mixture of vapor and droplets helps to pre-cool the part of the dry region and it helps the quench front to advance forward. The pre-cooling mechanism is called precursory cooling. If the momentum of these droplets is high enough, the droplet can penetrate the vapor layer and it can rewett the surface at a higher temperature. [4]

The base model is capable to correlate data at medium flow rates, but this effect must be taken into account at high flow rates. The precursory cooling is represented in analytical works by decreasing heat transfer coefficient in front of the quench front, e.g. exponential function as it is shown in Eqn.1.1 [6] (corresponds to Tab.3.2.1).

$$h_2 = \frac{h_1}{N} \cdot e^{-0.05} \tag{1.1}$$

Where h_1 $[W.m^{-2}.K^{-1}]$ is the heat transfer coefficient in the wet region and N $[-]$ is precursory cooling rate. h_2 $[W.m^{-2}.K^{-1}]$ is then the resulting heat transfer coefficient in front of the quench front.

1.8 Conclusion

A brief view on rewetting phenomenon was presented in this chapter. The process is accompanied by many parameters and side effects, which must be taken into account if we want to describe the process of flooding experimentally, such as precursory cooling, dynamics of coolant, initial conditions of the surface, internal heat source, etc. The

process was described side by side with the boiling curve and individual according to points in this curve were connected with the reverse meaning of quenching process. Also a definition of quenching, critical heat flux and nucleate boiling temperature was adopted in this chapter based on previous studies, own experiences and preliminary calculations.

Chapter 2

Loss of Coolant Accident

The rewetting mechanism of highly warmed surfaces is widely applicable in many technical applications. In the field of cryogenic technology, the rewetting phenomenon takes place especially when vessels are filled with liquid gases at the room temperature. From the perspective of nuclear reactor safety, the research of rewetting is crucial in the case of loss of coolant accidents (LOCA). At the same time, LOCA represents the concept of "Maximum Credible Accident", which is caused by sudden and complete separation of the main circulation pipe connected to the reactor vessel.

2.1 Principle of LOCA Accident

A loss of coolant accident is one of the most serious accidents that can affect a nuclear power plant. This accident includes a damage of high-pressure components of the primary cooling circuit especially a loss of integrity of primary piping. This may lead to a leakage and thus to loss of coolant. If the emergency cooling system works properly, the reactor core is reflooded and can be effectively cooled down. Otherwise, the accident leads to unavoidable core meltdown and to the destruction, of the power plant unit.

The LOCA accident can be divided into four successive processes:

1. Decompression and emptying of the primary loop

2. Refill of the bottom part of the reactor vessel

3. Reflood of the core

4. Long-term cooling of the core

2.2 Fenomenology of the LOCA Accident

A coolant presented in the system under high pressure expands into surrounding space and this expansion is accompanied by a pressure drop in the primary loop. When temperature level in the core reaches the saturation temperature for given conditions, a pool boiling takes place at the core outlet (Figure 2.1 a)). This boiling generates an enormous volume of vapor and this situation leads to a lower pressure decrease in the loop. The emptying is driven by critical outflow mechanism in this phase. If the pressure drops further, the pool boiling occurs in the whole primary circuit. The full-scale boiling is responsible for suppression of coolant circulation (Figure 2.1 b)). Depending on the exact point of leakage, the primary circuit is emptied very fast, until a residual volume of the coolant remains in the bottom part of the pressure vessel (Figure 2.1 c)).

The fuel pins forming the core without the presence of coolant are getting overheated. The cladding temperature in the core can reach up to 1204 °C (peak cladding temperature limit)[7]. Significant exceedance of this temperature limit can lead to the autocatalytic reaction of cladding with water/steam, fuel melting and destruction of the core followed by leakage of radioactive materials outside of the first and second barrier. The temperature rising has to be suppressed by the emergency core cooling system (ECCS). This system begins to deliver the coolant into the core as soon as possible through reverse throttle valves. However, in the case of large break LOCA accident, the core is already exposed and its cladding temperature rises. After several tens of seconds, the ECCS can refill the bottom of the reactor vessel. Once the bottom part of the reactor is refilled, the reflood process takes place (Figure 2.1 d)).

The coolant meets the overheated fuel pins during the reflood process and re-establishment of solid-liquid contact is necessary for the safe cooling down these pins in order to prevent the core meltdown. The understanding of the rewetting phenomenon is necessary for this reason.

Once the core is reflooded (Figure 2.1 e)), it is necessary to ensure its long-term cooling.
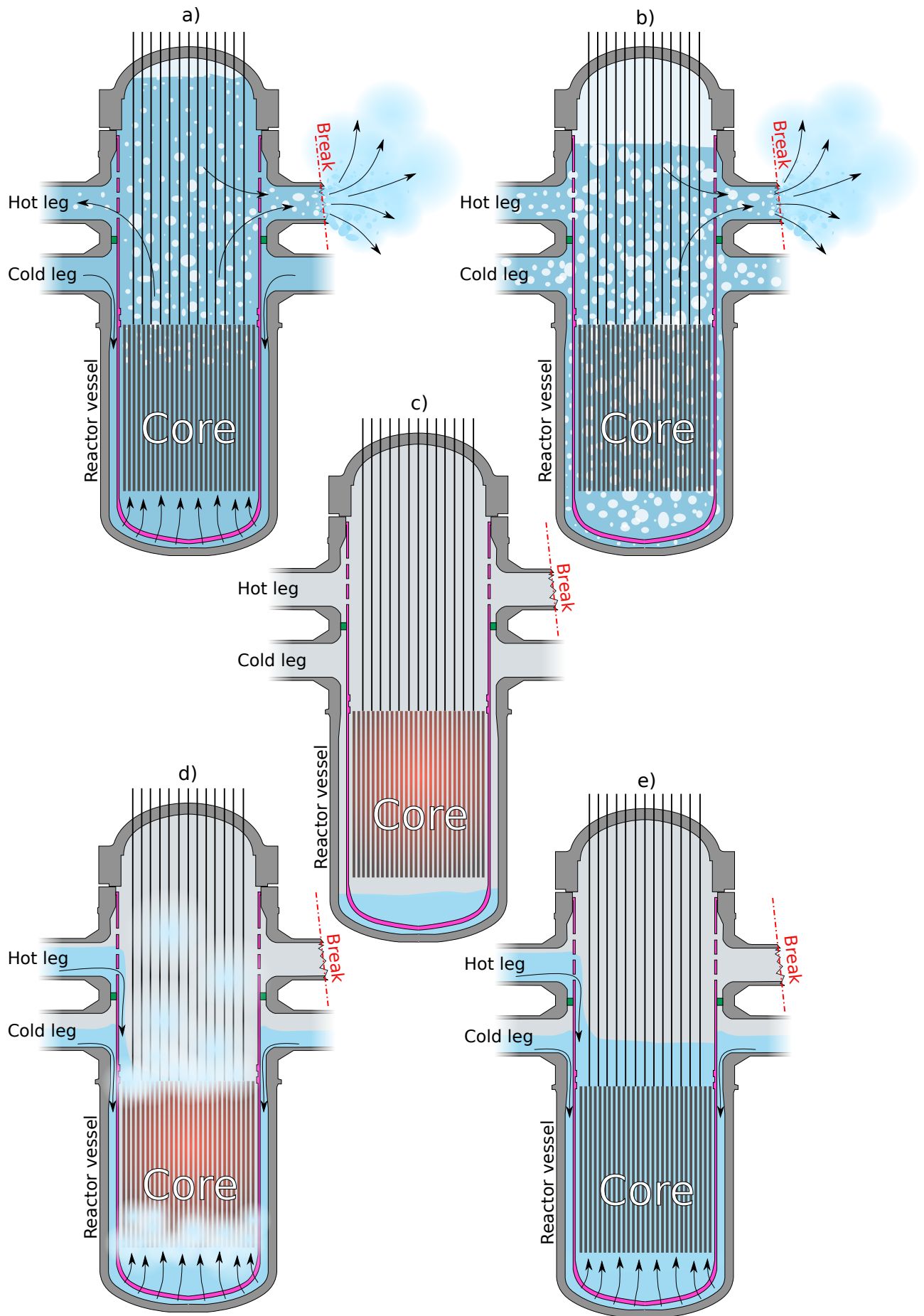
Figure 2.1: Fenomenological process of LB-LOCA accident

Chapter 3

Analytical models

Many mathematical models were created in the last forty years in order to solve rewetting phenomenon for different geometries. These models are either one-dimensional or two-dimensional. Also, several three-dimensional models can be rarely found with advances in computer technology. [A1] A brief overview of analytical studies, their features and philosophy are presented in this chapter.

3.1   Common Simplifications

Over time, many models have been created that contain common simplifications. These widely used assumptions are:

- Homogenous wall of infinite height

- Uniform wall thickness

- Neglect of precursory cooling (adiabatic dry region or its part)

- Constant quench front velocity

- Uniform heat transfer coefficient in the wet region. This assumption is used if the wet region is one-regional. Otherwise, if the wet region is two-regional, the region is split into two sub-regions: boiling and not boiling

- Only single fuel rod is included in the model. influence of surrounding rods is neglected.

- No heat generated within a wall

3.2   Basic Model

The basic rewetting model includes the mentioned simplifications. The most basic model for the analytical solution of the rewetting phenomenon is model which includes only two regions - wet (rewetted) region and dry region. A constant heat transfer rate for the wet region and the adiabatic boundary condition for the dry region are assumed in this approach in many analytical efforts. The model is then solved typically for infinite slab or infinite rod with the quasi-stationary approach. Most of these models were one-dimensional. Sometimes they included constant heat transfer coefficient also for the dry region instead of adiabatic one (see Tab.3.2.1). However, the heat transfer rate in the dry region is much lower than the heat transfer coefficient in the wet region so the heat transfer rate in the dry region can be neglected. This simplification is present in most works.

However, it must be noted, that assuming adiabatic or uniform heat transfer coefficient in the dry region is not correct from the physical point of view and thus resulting data cannot be physically correct. In this case, the heat transfer rate rises along the geometry in front of the quench front. The rising heat transfer rate is caused by rising wall temperature from the quench front. This behavior is unreal.[8] With consideration of multi-regional dry region, we can get more acceptable results. In this case, the farthest dry part of geometry can be considered with adiabatic boundary condition. Such effort was published by Elias and Yadigaroglu (1977)[9].

3.2.1   One-dimensional Models

In one-dimensional models, the radial (transverse) temperature profile is ignored. In this case, only axial conduction is taken into account. One of the first one-dimensional analytical rewetting solutions was proposed by Semeria and Martinet (1965)[10] followed by Yamanouchi (1968)[11]. Yamanouchi considered a constant heat transfer in the wet region and adiabatic boundary condition in the dry region. This solution gives a good agreement with experimental data for low quench front velocities (low Biot and Peclet numbers). His solution for inverse quench front velocity is in Eqn.3.1[11]. One of the most important information from the equation is the inverse dependence of quench front velocity u on initial wall temperature T_0. In short, quench front velocity decreases with rising initial wall temperature.

$$u^{-1} = \nu c_p \frac{\delta}{hk} \frac{T_0 - T_q}{T_q - T_s}; \quad \nu = f(Bi, \Theta_q) \qquad \frac{\sqrt{Bi}}{Pe} = \sqrt{\Theta_q(\Theta_q + 1)} \qquad (3.1)$$
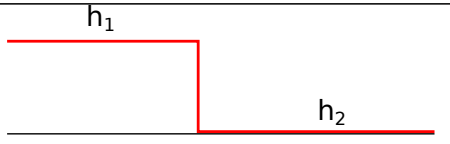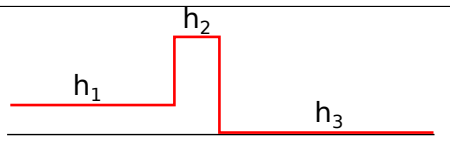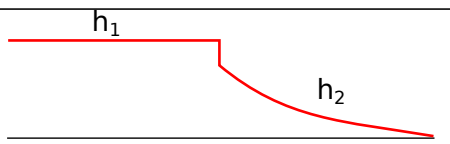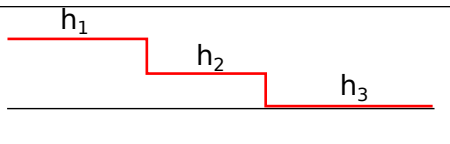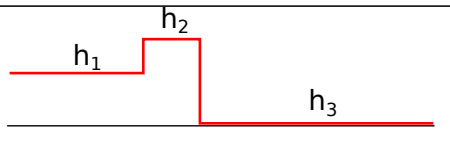
Next published reports by Andréoni (1975)[12] and Yandigaroglu (1977)[9] assumed dry region as uniform or multi-regional. These efforts solved the problem also as one-dimensional. These works are listed in the Table 3.2.1 and they are followed by many consequential efforts.
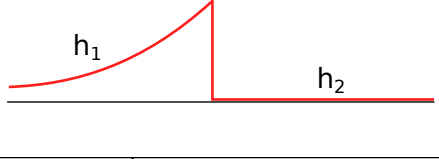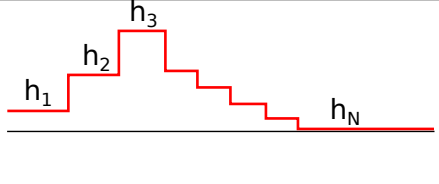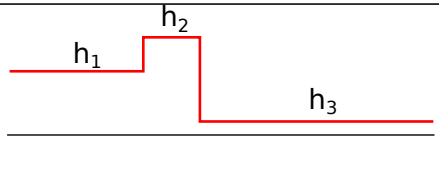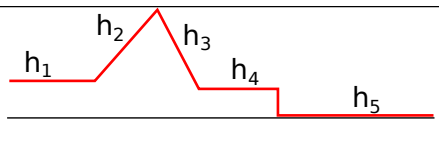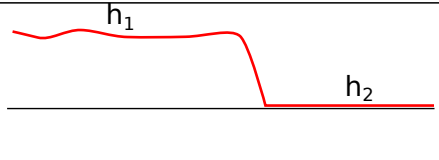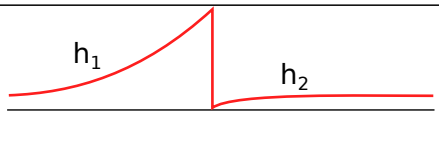
As mentioned, the adiabatic boundary condition is suitable for a thin slab with low rewetting velocity and with low Biot number. Under these conditions, a transverse temperature variation can be neglected. This transverse temperature profile begins to be significant at higher velocities and it can't be neglected. Thus a transition model between one-dimensional and two-dimensional formulation was developed. This model also introduced limitations for usage of the one-dimensional model for high values of Peclet and Biot number. The model was designed by Tien and Yao (1975)[13]. Other models for higher Biot numbers were developed subsequently.[8]

As can be evident from Tab.3.2.1, a lot of the models in the table work with more than two-regional model. The main reason is to reflect highest heat transfer near the quench front, where the heat transfer coefficient reaches its highest value due to transitional and nucleate boiling right behind the front. The first of these models was presented by Sun et al. (1974)[14] based on data by Yamanouchi (1968)[11].

Most of these studies need heat transfer coefficient and initial wall temperature as input parameters. In order to reduce this dependence on two input parameter, some models were developed. Initial wall temperature is the only parameter in these models. Thus heat transfer coefficient is the a part of solution, i.e. heat transfer coefficient is a function of wall temperature. This approach is also partially adopted in this study.

Table 3.1: Selected 1-D Basic models (Models with correlated experimental data)[15]

Author	Experimental data	$h[W.m^{-2}.K^{-1}]$	$T_{rew}[^{\circ}C]$	h regions
Yamanouchi, (1968)[11]	Yamanouchi, (1968)[11]	$h_1 = 2 \cdot 10^5$ $h_2 = 0$	150	h_1, h_2
Sun et al., (1974)[14]	Yamanouchi, (1968)[11]	$h_1 = 570$ $h_2 = 1.7 \cdot 10^4$ $h_3 = 0$	260	h_1, h_2, h_3
Sun et al., (1975)[6]	Yamanouchi, (1968)[11]	$h_1 = 1.7 \cdot 10^4$ $h_2 = \dfrac{h_1}{N} \cdot e^{-0.05}$	260	h_1, h_2
Chun, (1975)[16]	Case et al., (1973)[17]	$h_1 = 2.56 \cdot 10^4$ $h_2 = 170$ $h_3 = 0$	260	h_1, h_2, h_3
Ishii, (1975) [18]	Bennett at al., (1966)[19]	$h_1 = h_{CHF}$ $h_2 = 4 \cdot 10^5$ $h_3 = 0$	$260 \div 390$	h_1, h_2, h_3

Thompson, (1972)[20]	Bennet et al., (1966)[19]	$h_1 = R \cdot \Delta T_s^3$ $h_2 = 0$	$T_s + 100$	h_1 h_2
Elias, (1977)[9]	Duffey, (1972)[21]	$h_1 = 170$ $h_2, h_3, ... h_N$	260	h_3 h_2 h_1 h_N
Andreoni, (1975)[12]	Andreoni, (1975)[12]	$h_1..Jens - Lottes$ $h_2, h_3..experimental$	280	h_2 h_1 h_3
Chambré, (1979)[22]	Duffey, (1973)[23]	Taken from pool boiling	260	h_2 h_1 h_3 h_4 h_5
Piggott, (1973)[24]	Piggott, (1973)[24]	$h_1 = f(T)$ $h_2 = 0$	$T_0 = T_s + 100$	h_1 h_2
Karyampudi, (1976)[2]	Karyampudi, (1976)[2]	$h_1 = R \cdot \Delta T^4$ $h_2..radiation$	$T = T_c$	h_1 h_2

3.2.2 Two-dimensional Models

The main advantage of the two-dimensional model compared to one-dimensional is an ability to solve problems that contain high Biot and Peclet numbers, better said problems with thin walls and high quench front velocities. The first effort to provide a two-dimensional solution was formulated by Semeria and Martinet (1965)[10] besides their one-dimensional solution. However, they suggested model without the exact solution.[25] The first solution for two dimensions was created by Piggott and Porthouse (1973)[24]. They correlated their own data and data from Yamanouchi (1968)[11]. Their model is in Eq.3.2[24, 25]. [8]

$$ u^{-1} = \frac{2}{\pi} \frac{\delta}{k\rho c_p} \frac{\sqrt{T_0 - T_q}\sqrt{T_0 - T_s}}{T_q - T_s} \qquad BiPe = \pi\Theta_q(\Theta_q - \frac{4Bi}{2\pi})\frac{1}{22} \qquad (3.2) $$

Further Salcudean and Bui (1978)[26] came with two-dimensional models followed by efforts by Salcudean and Rahman (1980-1981)[27], Sawan and Temraz (1981)[28], Bonakdar and McAssey (1981)[29] and Hsu et al. (1983)[30]. These efforts were different in assumptions from the perspective of the number of regions and their heat transfer coefficients.

3.3 Analytical Solution of Precursory Cooling

The first model with precursory cooling was proposed by Edwards and Mather (1973)[31]. The model was two-dimensional. This model included exponential heat flux in front of the quench front as well behind it. The solution presented by Dua and Tien (1976)[32] included constant heat transfer coefficient in the wet region. Then analysis of precursory cooling of a tube with finite precursory length for the bottom and top flooding was proposed by Hirano and Asahi (1980)[33]. They solved the problem as one-dimensional with three-regional heat conduction model, where the first region included transition boiling, the second one included film boiling and the last one was characterized by adiabatic boundary condition (heat radiation was neglected). Other models by Olek (1988)[34] and (1990)[35] including precursory cooling were solved by separation of variables method or Wiener-Hopf technique in cartesian or cylindrical coordinate system. The common sign of these rewetting models with precursory cooling is especially dependence on these five parameters: Peclet number, Biot number, the initial temperature of the wall, size of the region influenced by precursory cooling and its rate. [8]

3.4   Decay Heat in Analytical Studies

Several analytical studies, which contained decay heat power, were published from the 1970s. One-dimensional unsteady analytical and numerical study was presented by Chan and Zang (1994)[36]. Their study was focused on grooved and smooth plates. [8] Another study on rewetting with the uniform heat source in infinite slab was presented by Platt (1993)[37]. An effort by Satapathy and Sahoo (2002)[38] was solved for the case of infinite cylindrical geometries using Wiener-Hopf technique. Then Sahu (2008)[39] proposed a solution for this model using the heat balance integral method technique. Other models included multi-regional assumptions of heat transfer coefficient and other variations such as thermal dependence of physical properties of the cooled wall, namely Elias and Yadigaroglu (1977)[9], Sawan (1979)[40] and Bera and Chakrabarti (1996)[41].

3.5   Temperature-dependent Parameters

It can be expected, that temperature-dependent parameter will heavily influence the rewetting process due to rapid cooling of the wall. It is evident, that heat conduction included in Biot number is the most influencing parameter from all temperature-dependence parameters. Some analytical efforts include the temperature dependence into solution. The solution of the problem is then a very non-linear set of equations. Works with incorporated temperature dependencies are for example solutions by Olek and Zvirin (1985)[42] and Sahu (2009)[43].

3.6   Solution Techniques

Most of the models solve rewetting problem using Fourier's heat conduction equation with given set of heat transfer coefficients. The form of the equation for infinite tube takes subsequent shape:

$$\frac{1}{r}\frac{\partial}{\partial r}(r\frac{\partial T}{\partial r}) + \frac{\partial^2 T}{\partial z^2} = \frac{\rho c}{k}\frac{\partial T}{\partial t} \qquad r_1 \ll r \ll r_2 \qquad 0 < z < L \qquad L \to \infty \qquad (3.3)$$

Rewetting velocity is then determined by application of energy conservation law and continuity of temperature profile. The solution includes some analytical and numerical methods. From analytical methods, it can be used for example separation of variables,

Wiener-Hopf technique or heat balance integral method (HBIM). From numerical methods we can name finite difference method, finite volumes method or isothermal migration technique by Durack and Wendroff (1977)[44] and Gurcak et al. (1980)[45].

The solution of the two-dimensional model with two regions (wet and dry) with variable heat transfer coefficient at the quench front for a slab and furthermore for composite slab was introduced by Olek (1988[15] and 1994[46]). In the first work, the dry region was assumed as adiabatic. The composite slab was composed of three slabs, the first one with internal heat generation, the second one was the heat insulator and the third one without the internal heat source. The purpose of these layers was to simulate nuclear fuel and its cladding. The rewetting process for the rod was solved by Evans (1984)[47] and for the tube, it was solved by Chakrabarti (1996)[48]. A physical model of the infinite vertical tube with uniform heat flux was presented by Sapathy and Sahoo (2002)[38]. Their work included dimensionless heat flux and adaptable computational mesh.[8]

3.6.1 Separation of Variables Method

Separation of variables method is relatively simple and straightforward in many cases for rewetting problems. Firstly, the rewetting velocity is chosen and it gives a formal solution of temperature distribution for every subregion. The solution is set of arrays with several constants. These constants are defined assuming continuous temperature profile between each subregion, continuous heat flux and orthogonal properties of its eigenfunctions. The obtained temperature of the quench front is then compared with experimental values. If the assumption of quench front velocity is correct then obtained quenching temperature has to be close to experimental one. If not, then the new value of velocity is taken and the iterating process is repeated. The issue of this method is the definition of a case with discontinuous boundary conditions. These discontinuities cause singularities in solution at interfaces and slow down solution convergence. Moreover, these discontinuities bring inaccuracies into the final solution. These problems can be solved using Wiener-Hopf technique. [15]

3.6.2 Wiener-Hopf Technique

Usage of this technique in rewetting models is less formal than usage method of separation of variables. This method was originally developed for the solution of the system of

integral equations, but it can be used for the solution of differential equations with different boundary conditions containing discontinuities. The typical discontinuity in rewetting is different heat transfer coefficient in the wet and dry region. However, it is very difficult to solve models with many regions using this method. [15]

3.6.3   Heat Balance Integral Method (HBIM)

This approximation method, as well as Wiener-Hopf technique, gives relatively simple expressions for the definition of quenching temperature and rewetting velocity. Moreover, it is capable to solve the multi-regional models. From some efforts, which used this technique, a good agreement with correlated data was obtained. The greatest limitation of this technique is limitation only for one-dimensional problems. Another limitation is lack of uncertainty of solution without the known exact solution. [49]

3.7   Overview of Basic Analytical Rewetting Models

Many efforts on the analytical solution of the rewetting phenomenon based on the basic model have been presented in the last forty years. These works used either of the presented techniques for the solution of the problem. Hand in hand with the evolution of computational power, they used more or less sophisticated approaches and simplifications. Selected analytical two-regional rewetting models are summarized in Table 3.7.

Table 3.2: Basic two-regional rewetting models and their results [8]

Source	Result
Semeria and Martinet, 1-D, (1965)[10]	$\dfrac{\sqrt{Bi}}{Pe} = \Theta_q$
Yamanouchi, 1-D, (1968)[11]	$\dfrac{\sqrt{Bi}}{Pe} = \sqrt{\Theta_q(\Theta_q + 1)}$
Duffey and Porthouse, 2-D slab, (1973)[23]	$\dfrac{Bi}{Pe} = \dfrac{\pi}{2}(\Theta_q + 1)$ $Bi < \dfrac{\pi^2}{4}(\Theta_q + 1)$ for high Pe
Coney, 2-D slab, (1974)[50]	$\dfrac{Bi}{Pe} = 1.6\Theta_q(\Theta_q + 1), \quad \dfrac{Bi}{Pe} < 1$
Andersen and Hensen, 2-D slab, (1974)[51]	for low Bi: $Pe = (Bi^*)^{0.5}$

	$Bi^* = Bi[\Theta_q(\Theta_q + 1)]^{1 - \sqrt{\pi/2}}$ for high Bi: $Pe = 0.7355 \cdot Bi^*$ $Bi^* = Bi[\Theta_q(\Theta_q + 1)]^{-\sqrt{\pi/2}}$
Tien and Yao, 2-D, (1975)[13]	for low Pe: $\dfrac{\sqrt{A}}{Pe} = \sqrt{\Theta_q(\Theta_q + 1)}; \; A = \dfrac{3Bi}{(1 + Bi)}$ for high Pe: $\dfrac{Bi}{Pe} = 1.707\Theta_q + 1.456\Theta_q$
Blair, 2-D cylinder, (1975)[52]	$\dfrac{Bi}{Pe} = \dfrac{\pi}{2}\Theta_q$
Yeh, 2-D cylinder, (1975)[53]	$\dfrac{2Bi}{Pe^2} = \Theta_q(\Theta_q + 1)$
Dua and Tien, (1977)[32]	$Pe = (\overline{Bi^*})^{0.5}$ for $\overline{Bi^*} < 0.3$ $Pe = 0.63\overline{Bi^*}$ for $\overline{Bi^*} > 20$ $Pe = \overline{Bi^*}\sqrt{1 + 0.4\overline{Bi^*}}$ for all $\overline{Bi^*}$ where $\overline{Bi^*} = \dfrac{Bi}{\Theta_q(\Theta_q + 1)}$
Sahu et al., 1-D, 2-D slab and cylinder, (2006)[54]	$\dfrac{\sqrt{M}}{Pe} = \sqrt{\Theta_q(\Theta_q + 1)}$ $M = \dfrac{Bi}{1 + Bi/1722}$

3.8   Dimensionless Numbers

In the table 3.7 we can see, that major basic rewetting models from the last more than forty years are functions of Biot (Eqn.3.4), Peclet (Eqn.3.5) and dimensionless temperature number (Eqn.3.6).

3.8.1   Biot Number

The Biot number is a dimensionless index that connects heat transferred from the body surface and its internal thermal resistance. A view on the time-spatial thermal be-

havior of the body can be provided from its value. From the Eqn.3.4 it can be evident when the Biot number is lower than 1 than the conduction inside the body is capable to distribute heat and balance its temperature profile.

Generally, if the Biot number value is less than 0.1 than the effect of conduction in the body wall can be neglected and thus simpler methods and equations can be used in numerical methods. On the other hand, the Biot values greater than 0.1 indicate the need for a complex solution for conduction inside the wall. The equation for Biot number calculation is in Eqn.3.4.

$$Bi = \frac{hL}{k} \tag{3.4}$$

where h is the heat transfer coefficient $[W.m^{-2}.K^{-1}]$, L is the characteristic length (eg. wall thickness) $[m]$ and k is the heat conduction coefficient of the wall's material $[W.m^{-1}.K^{-1}]$.

3.8.2 Peclet Number

The Peclet number is one of the dimensionless numbers used in heat transfer problems, where heat is transferred by a fluid. It presents a relationship between heat transferred through advection and heat transferred through conduction in the fluid. It can be also written as a product of Reynolds and Schmidt number for the mass transfer and as a product of Reynolds and Prandtl number for heat transfer. The form of Peclet number for heat transfer problems is written in Eq. 3.5.

$$Pe = Re \cdot Pr = \frac{\rho C u L}{k} \tag{3.5}$$

where ρ is a fluid density $[kg.m^3]$, C is a heat capacity of the fluid $[J.kg^{-1}.K^{-1}]$, u is a local fluid velocity $[m.s^{-1}]$, L is a characteristic length $[m]$ and k is a heat conduction coefficient of the fluid $[W.m^{-1}.K^{-1}]$.

In studies on the rewetting phenomenon, the Peclet number is assumed as dimensionless quench front velocity and it is used in a different way and thus the Peclet number loses its original meaning. Properties such as ρ, C, k are taken for wall material, L is replaced by wall thickness and velocity u is the velocity of advancing quench front.

3.8.3 Dimensionless temperature

Dimensionless temperature is a part of almost every analytical and experimental rewetting study. It is a proportion of temperature difference between actual wall temperature and saturation temperature of the fluid and temperature difference between quenching (rewetting) temperature and saturation temperature. The dimensionless formula is in Eq. 3.6.

$$\Theta = \frac{T - T_s}{T_q - T_s} \tag{3.6}$$

where T is a actual wall temperature $[°C]$, T_s represents a saturation temperature of the fluid $[°C]$ and T_q is the quenching temperature of the wall $[°C]$. From its definitions it can be assumed, that temperature at the quench front will lie between values of 1 and 0.

$$\Theta_q = \frac{T_0 - T_q}{T_q - T_s} \tag{3.7}$$

Analogously, the Eq. 3.7 shows modified dimensionless temperature at the quench front. In this equation T_0 is the initial wall temperature $[°C]$.

3.9 Conclusion

An overview of analytical studies on the rewetting phenomenon was summarized in this chapter. It includes important analytical studies in the field together with studies including precursory cooling and internal heat source. The overview shows the common dependence of individual efforts on the set of dimensionless numbers, which are mentioned in the last section. The dependence of quench front velocity on initial wall temperature, saturation temperature, heat conductivity, specific heat and other material and geometrical properties is also a crucial part of the presented study.

Chapter 4

Experimental Studies

Many experimental works have been performed in the last fifty years, especially in the 1970's and 1980's in order to deepen the knowledge of the rewetting phenomenon. These studies have been performed for various geometries such as an annulus, rod bundles, plates, etc. for a wide range of initial wall temperatures (generally $300\,^{\circ}C - 700\,^{\circ}C$) and also under different pressures and for several flow rates. Some works even dealt with the effect of reduced gravity. Subsequently, a lot of analytical efforts has been based upon obtained data as described in the previous chapter. A brief overview is presented in this chapter.

4.1 Overview of Experimental Studies

Shires et al.[55] investigated the experimentally rewetting phenomenon in the year 1964. The resulting finding of the work was, that time needed for surface rewetting is prolonging with rising initial wall temperature. Another consequential result was, that a specific temperature level exists in the rewetting phenomenon and the temperature represents the limit for re-establishing solid-liquid contact.

Bennett (1966)[19] conducted a set of experiments with heated stainless steel tube in the steam environment. He proved the existence of the exact quenching temperature for every pressure level within many pressure level ranges with maximum pressure up to 1000psi (6.9MPa). Yamanouchi (1968)[11] presented quenching experiments and he described a conduction controlled rewetting phenomenon with axial heat conduction toward the quench front. This heat is then removed by fluid in the rewetted region due to high heat transfer coefficient. In this work the wet region heat transfer coefficient was taken as a constant, in the dry region he assumed the heat transfer rate as a function of actual wall temperature and saturated temperature of the coolant in the shape:

50

$$q'' = 1.5(T_w - T_s)^{1.5} \tag{4.1}$$

Later, Tohompson (1972)[20] introduced exponential heat transfer rate in the wet region as a function of the third power of saturation temperature. The dependence is in Tab.3.2.1 on the page 42. An important point of this work is the influence of wall heat capacity on the rewetting velocity. The observed effect of the capacity was that quenching of a zircalloy tube was twice as short than for stainless or Inconel tube. A similar model was introduced for the dry region by Karyampudi and Chon (1976)[2].

Duffey and Porthouse (1973)[23] examined a wide range of materials with initial wall temperatures within the range $300 - 800\,°C$, flow rates $0.1 - 30\,g/s$. The length of the test section was $20\,cm$. The conclusion of their work was, that one-dimensional analytical solution is in good agreement with experimental data for low Pe and Bi numbers for the bottom and top flooding. On the other hand, the process begins to be more unpredictable in case of high velocities, thick walls and varying heat conduction of the wall. Another result was a designation of Leindenfrost temperature within the range of $190 - 250\,°C$.

Experimental studies also showed a uniformity of quench front velocity along the cooled geometry. However, a majority of experimental studies was performed on geometries shorter than $1.5\,m$ whereas nuclear reactor fuel pins are over $3\,m$ high. With increasing distance to be cooled down also increases dry region that is cooled by vapor and droplets (precursory cooling). This means, that more heat will be removed during the process in front of the quench front a thus a lower temperature will be present at the specific point, while quench front reaches this place. Higher precooling of the dry region leads to higher quench front velocity and to unequal front advance. [A3]

One of the latest experimental efforts is work by Saxena et al. (2001)[56]. Their experimental loop consisted a test section $3030\,mm$ high for bottom flooding and $2630\,mm$ high for top flooding. Initial wall temperature range was $200 - 500\,°C$. Two correlations based on obtained data were proposed for both directions of flooding.

- For top flooding:

$$u_T = \frac{5546}{\Theta_q^{0.15}\rho C}\left(\frac{Q}{2\pi r}\right)^{0.8} \tag{4.2}$$

- For bottom flooding:

$$u_B = \frac{7285}{\Theta_q \rho C}\left(\frac{Q}{2\pi r}\right)^{0.84} \tag{4.3}$$

where $Q[l/min]$ is the flow rate, $C[kJ/kg]$ is the the heat capacity of the wall, $\rho[g/cm^3]$ is the wall density, $r[mm]$ is the outer radius of the tube and resulting quench front velocity is $u[mm/s]$. However, this study also does not reflect the varying quench front velocity dependent on actual front position. Incorporation of some kind of position is necessary for the better description of the quench front velocity for high test sections.

Generally, we can conclude according to experimental efforts, that quench front velocity rises with:

- Coolant flow rate

- Coolant sub-cooling

- Thinner wall

- Lower internal heat source power

Selected experimental studies on bottom flooding are summarized in Table 4.1. These experimental studies are also graphically mapped in Figure 4.1. This map clearly shows the lack of bottom rewetting studies with heated length over $1.5\,m$ and simultaneously the lack of experiments covering wide range of initial wall temperatures. The presented study is highlighted in the figure. It is also evident from this map, that lengths over 2 meters are very rare and only length of $3.6\,m$ is covered by experimental studies with rod bundle test section configuration. The reason is, that the length of $3.6\,m$ is the height of typical pressurized water reactor. However, this study focuses on basic research on rewetting behavior and for this purpose a basic geometry such as annulus is much more suitable. Unfortunately we can find only two experimental efforts above length of $1.5\,m$: Saxena (1998)[56] and Cho (2007)[57]. However, these studies do not cover a very wide temperature range. Despite the fact that this map clearly shows the scattering of experimental works, it does not take into account the mass flows and the channel cross-sections. This information is often difficult to obtain and properly compare each other's study.

Table 4.1: Experimental studies on bottom flooding [56]

Author	Geometry	Year	Heated length [m]	Water flow rate [lpm]	Initial wall temperature [°C]	QF velocity (Result) [cm/s]
Duffey, Porthouse [23]	Annular	1973	0.2	0.006 - 1.2	300 - 800	0.1 - 5
Piggot, Duffey [58]	Annular	1975	0.5	0.1 - 0.55	700	0.15 - 0.6
Piggot, Porthouse [59]	Annular	1975	1.2	0.036 - 3.6	400 - 700	0.1 - 3.3
Lee [60]	Tube	1978	4	1.2 - 6.1	450 - 650	2.5 - 17
Chung [61]	Annular	1980	0.6	-	300 - 700	0.25 - 40
Neti, Chen [62]	Tube	1981	1.45	0.045 - 0.94	400 - 600	0.5 - 9.5
Bankoff [63]	Tube	1982	3.5	0.5 - 3.6	550	2.8 - 10
Lee, Shen [64]	Tube	1985	4; 2	-	350 - 550	4 - 22
Boer, Molen [65]	Rod bundle	1985	1.5	$2 - 20 cm/s$	400 - 800	1 - 3
Yonomoto [66]	Rod bundle	1987	1.8	34	630	-
Muto [67]	Rod bundle	1990	3.7	$280 - 1400 kg/m^2/s$	Var. power (350-600)	Correlation

Tuzla [68]	Rod bundle	1991	1.2	0.56 - 2.1	800	0.1 - 0.5
Barnea [69]	Annular	1994	0.8	-	350 - 600	16 - 38
Huang [70]	Tube	1994	0.05	0.12 - 2.4	Stable film boiling temp.	Min. boiling temp. and CHF
Iguchi [71]	Rod bundle	1999	3.66	$20 - 3500 kg/m^2/s$	up to 700	Spacer effect
Saxena et al. [56]	Annular	1998	3.03	1.0 - 7.2	200 - 500	5 - 62.5
Cho [57]	Annular	2007	1.83	-	500 - 700	2 - 5
Cho [72]	Core model	2009	1.95	19.2	300 - 550	-
Stuckert [73]	Rod bundle	2010	1.024	2.46	up to 1776	0.4 (cladding oxidation)
U.S.NRC [74]	Rod bundle	2012	3.66	-	760 - 870	2.54 - 15.24
Lymperea [75]	Annular	2015	1.016	0.5 - 3.0	300 - 550	Correlation
Štěpánek, Bláha [A3]	Annular	2016	1.75	0.55	250 - 800	2.5 - 12.5
Štěpánek, Bláha [A4]	Annular	2017	1.75	0.55, 1.1	250 - 800	2.5 - 14.5
This study	Annular	2018	1.75	0.8, 1.1, 1.9, 2.7	250 - 700	2.5 - 25
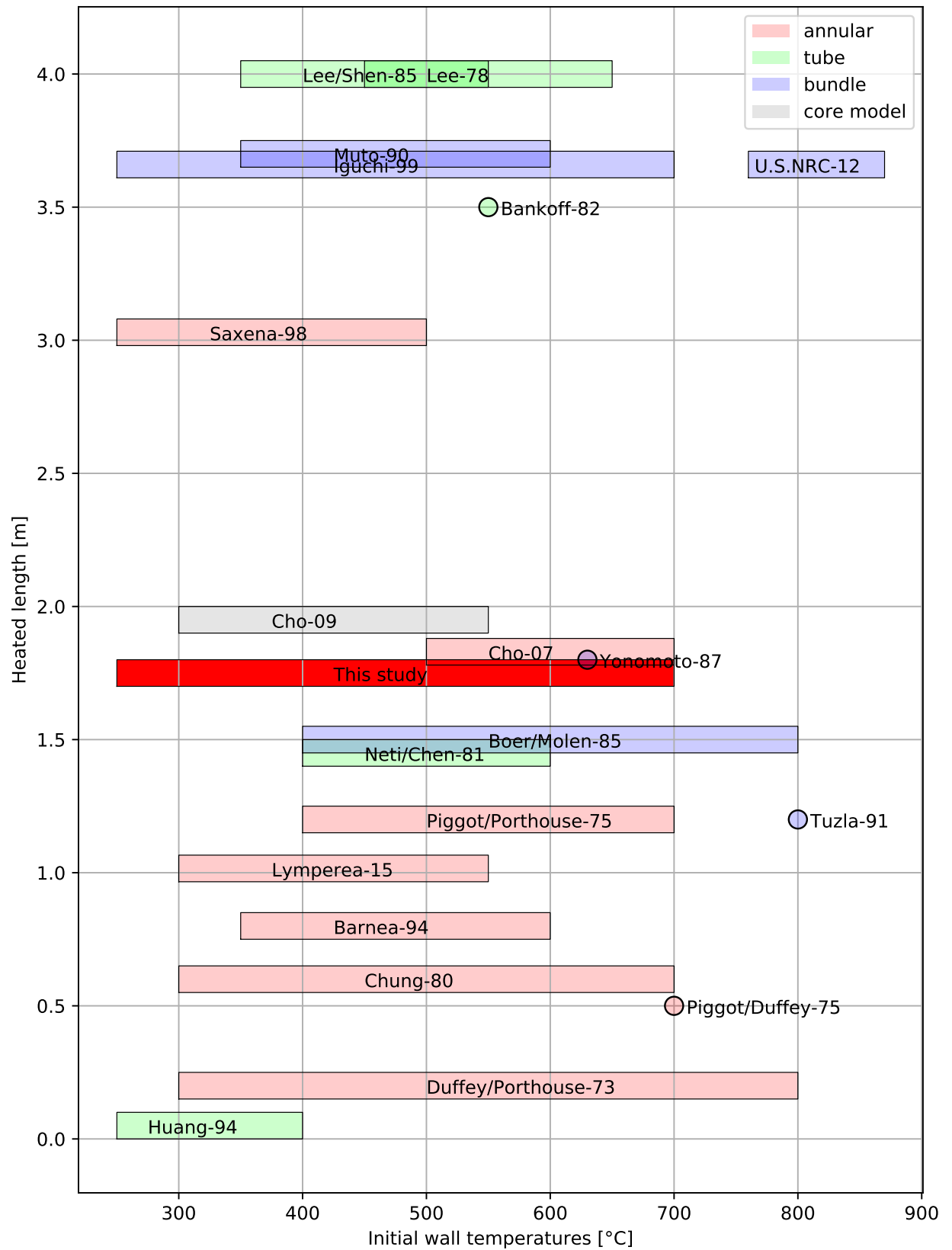
Figure 4.1: Map of experimental studies on bottom flooding from Table 4.1

4.2   Spacer Grid Effect on Reflood Process

There are many works aimed at the quenching temperature and rewetting velocity but few of them were focused on the spacer grid effect on the reflooding phase of LOCA. The main purpose of the grid spacers is to maintain relative rod position in a fuel rod bundle. Another effect is to increase heat transfer rate in the single-phase flow due to turbulization effect. Their effect on the reflood process has been pointed out in several experimental studies. One of the first studies was study by Sigumoto (1984) [76]. An experimental test section was 3.6 m high with 6x6 lattice equipped with six 40 mm high spacers. Initial wall temperature levels were $400\,°C$ and $550\,°C$.
He presented three effects of the spacer on the geometry reflooding:

- The heat transfer above the spacer was $20 - 50\%$ higher than below the grid

- The average droplet diameter was smaller above the spacer due to better heat transfer from vapor to the droplet

- In the slug flow regime, the spacer was rewetted early and water was accumulated near the spacer in the disperse flow regime

Another experimental work on the spacer grid effect was presented by Igushi (1999) [71]. The test section (5x5 lattice, heated length of 3.66 m) was equipped with 9 spacers. Tests were performed under the wide pressure range of $0.2\,MPa$ to $15.5\,MPa$, initial wall temperature was $630 - 730\,°C$. The main conclusions of the work are as follows:

- Spacers affect significantly the quench front propagation under high mass flux

- Quench front is incontinuous at high mass flux

- Spacers shorten quench time by 30% at mass flux of $500\,kg.m^{-2}.s^{-1}$, under $30\,kg.m^{-2}.s^{-1}$ the effect is insignificant

- Spaces have a positive effect on heat transfer coefficient in front of the quench front especially for high mass flux

A study focused on flat spacers and spacers with swirl-vanes was performed by Cho et al. (2007) [57]. The test section (annular channel, $1.83\,m$ of heated length) was equipped with three flat/mixing spacers. Initial wall temperatures were in the range $500 - 700\,°C$. They concluded, that swirl vanes have another positive effect on the quenching

velocity. However, this effect can be caused by the different design of these two spacers and thus different heat transfer area of the grid. Other conclusions are in agreement with Sigumoto and Igushi [76],[71]. Moon (2012) [77] investigated the spacer effect on the heat transfer enhancement in front of the quench front, i.e. in the dry single-phase region. The secondary aim of this study was to describe the spacer grid effect on the breakup of artificially injected droplets into the steam environment of the test section. He concluded, that the breakup ratio increased with rising Weber number (with increasing speed) due to the higher velocity of droplets impacting on the spacer grid face.

4.3   Conclusion

It can be concluded based on reviewed experimental efforts, that a lot of works includes test sections with the length under $1.5\,m$ and higher test sections are performed on complex geometries such as rod bundles. The annular channel is very good channel geometry for phenomenon description and moreover, these data can be also the input for analytical studies. This is very difficult for too complex geometries. Individual experiments can be slip into two groups: the first group takes initial wall temperatures within the range from $300\,^{\circ}C$ to $500\,^{\circ}C$ and the second group from $500\,^{\circ}C$ to $700\,^{\circ}C$. Experimental studies covering a wide range of temperatures are quite rare, especially in terms of basic geometries such as annulus.

Chapter 5

Goals

The main goal of this study is to deepen the knowledge of the quenching phenomenon. This overall goal was split into several individual goals:

- Build an experimental loop for investigation of quenching phenomenon in a flooded annular channel with three changeable tubes for consideration of accumulated heat and more real uneven heat generation

- Collect a large number of new experimental data with all relevant variables influencing the process

- Development of new approaches for experimental data evaluation and self-operational code for batch processing of individual quenching data with a built-in algorithm for correlation development

- Propose correlations for quenching and nucleate boiling temperatures, which are the main breakpoints in the process

- Propose formulas for calculations of heat transfer coefficients during the process

- Development of three-regional quenching model for further analytical studies

- Development of a correlation (or full set of correlations) for prediction of quench front velocity

- To point out the accompanying phenomena such as the influence of spacers and pressure peaks on the bottom flooding process

Chapter 6

Experimental Loop

For the purpose of detailed investigation of rewetting phenomenon an experimental loop has been built. Its component description, construction and parameters are in this chapter.

6.1   Main Parts

The used experimental loop was originally constructed for critical heat flux experiments. After these experiments, the equipment was rebuilt for a purpose of rewetting research. [A1]

Main parts of the experimental loop are as follows:

- Variable hydraulic circuit

- Test section

- Power source

- Data acquisition system (DAS)

The loop scheme is shown in Figure 6.1 and its part-by-part description is followed in next sections.

Figure 6.1: Simplified experimental loop scheme (Full scheme in Appendix 15.2 on page 173)

Table 6.1: Main parameters of the presented study

Mass flux (G)	$80 - 270\,kg.m^{-2}.s^{-1}$
Coolant	Water
Coolant temperature (T_{cool})	$\sim 20\,^{\circ}C$
Initial wall temperature (T_0)	$250 - 700\,^{\circ}C$
Pressure	Atmospheric
Internal heat source given by steady state at initial wall temperature	

6.2   Variable Hydraulic Circuit

The hydraulic circuit is the biggest part of the equipment. It is constructed with respect to all possible experiments such as critical heat flux experiments, bottom flooding and top flooding configuration. Also, a pre-heater for different coolant sub-cooling is an integral part of the circuit. The base construction material of the circuit is 25×3.5 PPR (polypropylene) pipes due to the absence of corrosion, good flexibility, easy installation and good temperature stability for given temperature range of coolant. All parts are chosen as stainless. The main reason is to avoid corrosion because of a possible impact of impurities on the investigated process and ensuring a clear view of the inner heated tube in the test section. The circulation of water is ensured by the pump with stainless (brass) body and plastic impeller for the same reason.

6.2.1   Circulation Pump

Wilo Star-Z 25/2 has been chosen for the circulation pump. It is a standard circulation pump for drinking water or heating systems. Its only specialty is the brass body and plastic impeller due to non-corrosion benefits as it was mentioned above. All relevant technical data are summarized in Table 6.2.1.

Table 6.2: Circulation pump main technical data (Source: www.wilo.com)

Type	Wilo Star-Z 25/2 EM
Temperature range	$-10... + 110\,°C$
Maximum operating pressure	$1\,MPa$
Revolutions	$2700\,RPM$
Input	$46\,W$
Housing	Red brass (CC499K)
Impeller	Plastic (PPO)
Shaft	Alumina (Al2O3)
Pump head	$0.5/3/10\,m$

6.2.2 Flow Meter

A turbine flow meter Vision 2008 (see Figure 6.2) was chosen for flow rate measuring. The main reason for this choice is the easy installation, no maintenance, small size and good precision. The actual flow through easily readable frequency output can be measured. High numbers of pulses also offer a good resolution of the output. [A1] There is no need of installation of straight pipe in front of the meter. Due to simple mechanical construction, a long lifespan is guaranteed without loss of accuracy. Moreover, pressure pulses do not affect the measuring.

Measuring principle is based on the axially mounted turbine and a hall generator. Rotations of turbine caused by flowing water are transferred to frequency for digital or

analog signal processing. Generated pulses are represented by a magnitude called K-factor. Units of K-factor are pulses per liter (PPL). The flow meter is capable to measure low viscous and non-aggressive liquids such as water, oils, fuels, etc.

Main technical data for the chosen type of Vision turbine flow meter are in Table 6.3.

Figure 6.2: Vision turbine flow meter

Table 6.3: Vision turbine flow meter technical data (Source: www.badgermeter.com)

Type	Vision 2008 4F44
Measuring rate	$1 - 15\,lpm$
Frequency	$36.7 - 550\,Hz$
K-factor	$2200\,PPL$
Material	Polyamid 12 / Trogamid
Viscosity range	$0.8 - 16\,mm^2.s^{-1}$
Repeatability	$< 0.5\,\%$
Accuracy	$\pm 3\%$ of value
Temperature range	$-20... + 100\,°C$
Power supply	5 - 24 VDC
Output signal	Pulses by open collector (NPN sinking)
Pull-down resistor	$1 - 22\,k\Omega$

6.2.2.1 Flow Meter Calibration

The flow meter was calibrated using the standing start-and-stop method. It is the simplest method available. The calibration curve is shown in Figure 6.3. The measured data were linearly regressed using least squares fit and resulting parameters are in Table 6.4.

Table 6.4: Calibration data correlation results

Slope	0.0242
Y-intercept	0.21069
Correlation coefficient R^2	0.996
Standard deviation of the slope	0.000398
Standard deviation of the y-intercept	0.0211
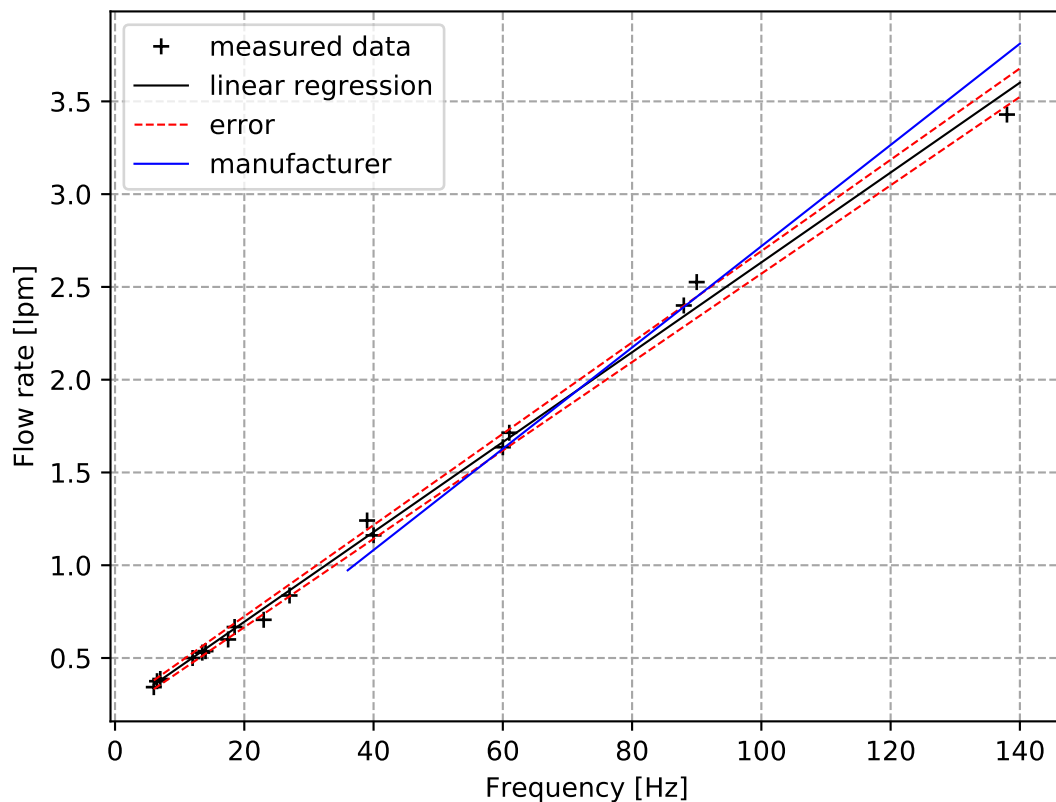
Figure 6.3: Calibration line of turbine flow meter

From linear regression of measured data a flow rate value in liters per second can be calculated. The linear function is in Eqn. 6.1 bellow:

$$\dot{Q} = 0.0242 \cdot f + 0.21069 \tag{6.1}$$

where $f\,[Hz]$ is the scanned frequency of the turbine flow meter and $\dot{Q}\,[lpm]$ is the resulting actual flow rate. Standard error of the flow rate value is than calculated using rounded standard deviations of the slope and the y-intercept of the least squares fit:

$$\dot{Q}_{err} = \pm 4 \cdot 10^{-4} \cdot f + 0.022 \tag{6.2}$$

From the standard deviation and flow rate value a relative error in % can be calculated as:

$$\delta_{fr} = \pm 0.13 \cdot \dot{f}^{-0.37} \tag{6.3}$$

6.3   Test Section

The test section is the main part of the whole experimental equipment. It consists mainly of an annular channel and two nodes (chambers): upper and lower one. The flow channel is constructed from two parts. The first one is a transparent outer barrier made of silica glass and the second part is an inner electrically heated stainless steel tube equipped with the set of thermocouples.

The flow channel geometry differs in experimental studies as it was mentioned in Chapter 4 on page 50. In this study, annulus was chosen for several reasons. The first reason was technical restrictions such as maximum input power and dimensions of outer barrier. The second pragmatic and the more important reason is, that obtained experimental can be used for further analytical studies. Complex geometry such as rod bundle with complicated spacers are very good for disposable description of the phenomenon, but for analytical processing of data, a "simpler" approach is required. The main reason is, that mathematical solution techniques containing complex boundary conditions and its discontinuities are almost unable to solve the problem for very complicated geometries due to resulting singularities in solution. Moreover, an annulus is clear, simple and uniform flow area and thus attention can be focused at just one advancing quench front and its behavior. The annulus is also a very good basis for further works in the field.
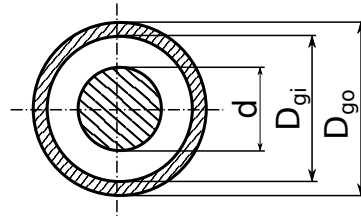
Figure 6.4: Test section annulus diameters

Table 6.5: Geometry of the test section

Total height (annular channel)	2 m
Steel tube total length	1.775 m
Heated length	1.725 m (318 D_h)
Cold inlet length	0.21 m (38 D_h)
Silica glass tube outer diameter (D_{go})	18 mm
Silica glass tube inner diameter (D_{gi})	14.5 mm
Heated tube outer diameter (d)	9 mm
Flow area	101.5 mm^2
Hydraulic diameter (D_h)	5.5 mm

Dimensions of annular channel are in Table 6.5 and its cross-section is in Figure 6.4. Total resulting flow area of the channel is given by Equation 6.4:

$$A_f = \frac{\pi(D_{gi}^2 - d^2)}{4} = \frac{\pi(14.5^2 - 9^2)}{4} = 101.5 \, mm^2 \tag{6.4}$$

Hydraulic diameter is calculated as:

$$D_h = \frac{4.A_f}{O_w} = \frac{4.(\frac{\pi.(D_{gi}^2 - d^2)}{4})}{\pi.(D_{gi} + d)} = \frac{(D_{gi}^2 - d^2)}{D_{gi} + d} = D_{gi} - d = 14.5 - 9 = 5.5 \, mm \tag{6.5}$$

Mass flow rate is scanned from turbine flow meter as frequency $[Hz]$ and then it is converted into mass flux $G\,[kg.m^{-2}.s^{-1}]$, assuming water density as $\rho = 998\,kg.m^{-3}$:

$$G = \frac{\dot{Q} \cdot \rho}{A_f \cdot 60 \cdot 1000} = \frac{(0.0242 \cdot f + 0.21069) \cdot 998}{101.5 \cdot 10^{-6} \cdot 60 \cdot 1000} = 3.966 \cdot f + 34.53 \qquad (6.6)$$

and its standard error $G_{err}\,[kg.m^{-2}.s^{-1}]$ is given analogously using Eqn. 6.2:

$$G_{err} = \pm \frac{\dot{Q_{err}} \cdot \rho}{A_f \cdot 60 \cdot 1000} = \frac{(0.0004 \cdot f + 0.022) \cdot 998}{101.5 \cdot 10^{-6} \cdot 60 \cdot 1000} = \pm 0.066 \cdot f + 3.61 \qquad (6.7)$$

6.3.1   Heated Tubes - Models

The inner tube in the test section is changeable. There were used three different tubes - models during experiments. These models have different wall thickness for heat capacity and profiled heat flux effect investigation. All models have the same outer diameter of $9\,mm$ and the wall thickness differs.

The tested models are (δ is the wall thickness):

- Model A: $\delta = 0.5\,mm$, steel $MONEL^{\circledR}$ K500 (UNS N05500)

- Model B: $\delta = 1.0\,mm$, steel X6CrNiTi18 - ČSN 17 248 / AISI-321

- Model C: $\delta = f(z)$, steel $MONEL^{\circledR}$ K500 (UNS N05500)

The last tube has variable wall thickness for simulation of the variable heat source within the geometry. The models are heated by direct current. The thinner wall means smaller cross-sectional area and this leads to lower current density i.e. lower generated heat at given position. The profile of the thickness function corresponds to the cosine function. The dependency of wall thickness on model position is in Figure 6.5.
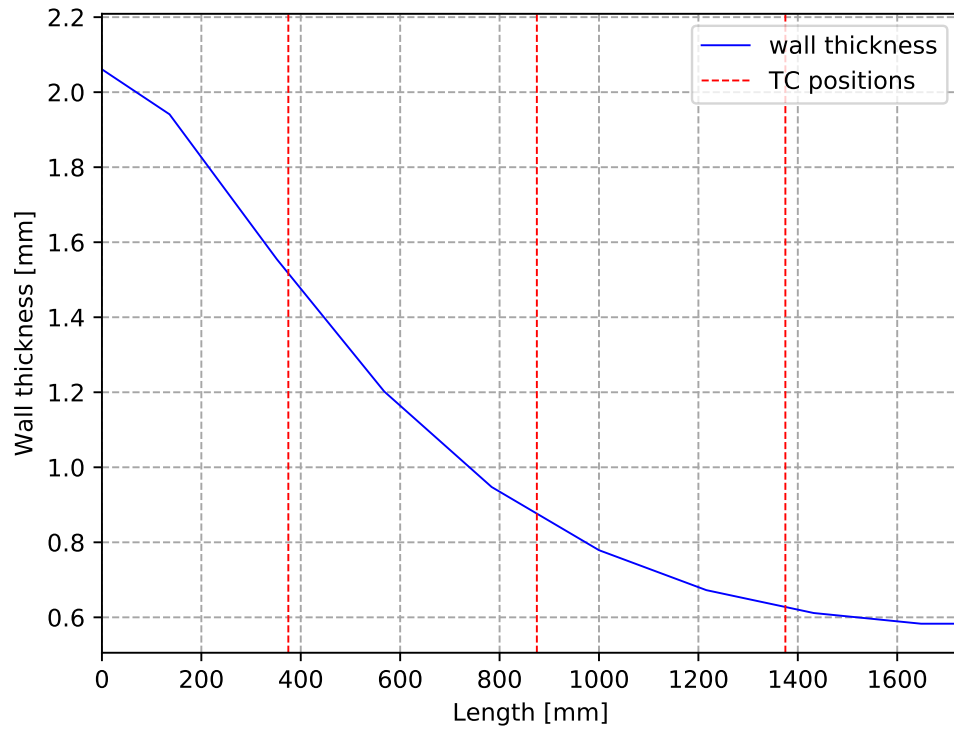
Figure 6.5: Wall thickness of the model C

6.3.1.1 Thermal Properties of the Heated Models

Thermal properties of used materials have to be incorporated into the numerical processing of measured data because of the wide range of initial wall temperatures in this work. Thermal property such as electric resistance varies significantly during cooling and thus resulting internal power is strongly dependent on the correct value of the resistance. These properties are thermal conductivity $k\,[W.m^{-1}.K^{-1}]$, specific heat $C\,[J.kg^{-1}.K^{-1}]$, electric resistance $r\,[\Omega.mm^2.m^{-1}]$ and density $\rho\,[kg.m^3]$. These dependencies of properties were obtained from material data sheets [78], [79]. Thermal properties were approximated and resulting equations are listed below. The equations are functions of temperature $T\,[^{\circ}C]$.

- **Thermal conductivity** $[W.m^{-1}.K^{-1}]$

  Monel K-500

$$k_M = 0.02952 \cdot T + 16.538 \tag{6.8}$$

  AISI-321

$$k_A = 0.0151 \cdot T + 14.184 \tag{6.9}$$

- **Specific heat** $[J.kg^{-1}.K^{-1}]$

  Monel K-500

$$C_M = 1.05276\text{e}{-}6 \cdot T^3 - 0.001096 \cdot T^2 + 0.5159 \cdot T + 407.02 \tag{6.10}$$

  AISI-321

$$C_A = -8.3187\text{e}{-}5 \cdot T^2 + 0.272 \cdot T + 462.92 \tag{6.11}$$

- **Electric resistance** $[\Omega.mm^2.m^{-1}]$

  Monel K-500

$$r_M = 7.8779\text{e}{-}5 \cdot T + 0.6131 \tag{6.12}$$

  AISI-321

$$r_A = -2.8298\text{e}{-}7 \cdot T^2 + 7.69\text{e}{-}4 \cdot T + 0.73187 \tag{6.13}$$

- **Density** $[kg.m^3]$ (calculated through thermal expansion coefficient)

  Monel K-500

$$\rho_M = 8440 \cdot (1 - 3 \cdot 15.6\text{e}{-}6 \cdot (T - 20)) \tag{6.14}$$

  AISI-321

$$\rho_A = 7900 \cdot (1 - 3 \cdot 19.3\text{e}{-}6 \cdot (T - 20)) \tag{6.15}$$

6.3.2 Thermocouples

The crucial part of the study is the most accurate temperature measurement especially in the sense of measurement response. The measurement response is most important during data processing because derivatives of the measured temperature profiles are used for heat flux calculation and calculation of heat transfer coefficient. Isolated $0.5\,mm$ K-thermocouples were chosen not only for their small dimension but also for their short response time. This applies to the three thermocouples positioned along the heated tube.

The fourth thermocouple is fixed on the outer surface of silica glass tube. Its main purpose is to indicate steady state through the glass barrier for flood initialization.

The last thermocouple is located inside the lower chamber. The thermocouple measures inlet temperature of water.

Another question is the construction of the experimental model and thermocouple installation. Basically, there are three possible options:

- **Installation from outside** - This installation method is quite simple and can be done either by fixing the thermocouple with staple (Figure 6.6 a)) or by soldering (Figure 6.6 b)). Moreover, the thermocouple can be positioned right on the wall or in a groove. This method is suitable for applications involving coolant flow inside the tube or applications with large flow area. In this study, the annular channel is too narrow for this method. On top of that presence of thermocouple within the flow cross-sectional area may strongly influence the flow, especially it can create another quench fronts near the thermocouple due to its low heat capacity and heat exchange surface. This method was used for installation of the thermocouple for measuring the silica glass tube surface temperature.

- **Installation from inside** - Thermocouples are conducted inside the heated tube and they are leaned against the wall (Figure 6.6 c)). On the one hand this method is also relatively simple but on the other hand, it gives information primarily about internal surface temperature and temperature derivative can be influenced for thicker walls due to heat conduction and heat capacity of the wall. Probably the greatest disadvantage of this method is no control over the real situation between the measuring junction of the thermocouple and inner wall surface. There is also no information about the actual position of the thermocouple.

- **Installation into the wall** - This method proved to be the most reliable. Thermocouples are conducted inside the tube and soldered with silver directly to the hole inside the wall (Figure 6.6 d)). The thermocouple junction is aligned with the outside tube surface. This design gives better information about surface temperature and it also gives a good response to temperature changes. This method was used in the current study.
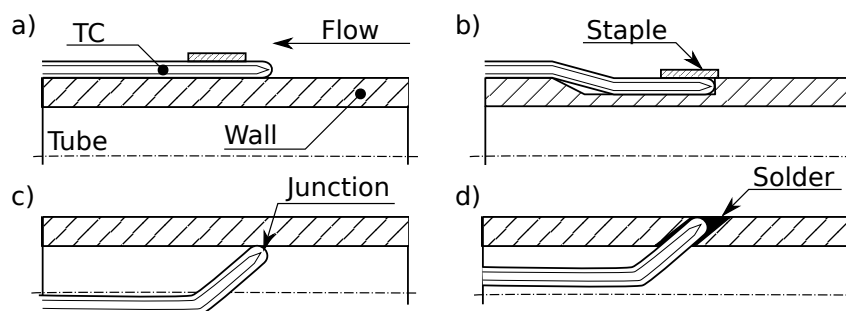
Figure 6.6: Thermocouple installation methods

There are three thermocouples soldered inside the tube wall. Their pitch is $0.5\,m$ and their individual positions are in Table 6.6.

Table 6.6: Positions of thermocouples

	Positions relative to:		
TC	Pressure sensor	Channel inlet	Heated length
Water	$0\,mm$	$-35\,mm$	$-245\,mm$
1	$580\,mm$	$545\,mm$	$335\,mm$
2	$1080\,mm$	$1045\,mm$	$835\,mm$
3	$1580\,mm$	$1545\,mm$	$1335\,mm$
GL	$1080\,mm$	$1045\,mm$	$835\,mm$

6.3.2.1 Thermocouples Calibration

The thermocouples installed in the heated tube are uncalibrated and due to their fixation, they cannot be calibrated. The accuracy of uncalibrated K-thermocouple is $\pm2.5\,°$ (ČSN EN 60584-2).

The thermocouple positioned inside the lower node for measuring of water temperature was calibrated. Its temperature shift was determined by immersion in water-ice mixture at $0\,°$. The shift for the thermocouple is $+1.1\,°$. Using this shift value of measured water temperature was corrected.

6.3.2.2 Maximum Temperature Limitation

The thermocouples are soldered into tube wall by silver solder. The melting point of silver solder is $710\,C°$ and thus the maximum initial temperature for experiments is limited by this temperature. Otherwise, the thermocouple can be melted out and the model is destroyed.

6.3.3 Spacers

The heated tube is equipped with four spacer grid elements. The spacers have two functions. The first and most important purpose is to help us to investigate their effect

on reflood process because spacer grids are the part of every pressurized and boiling water reactor and thus their presence must be taken in mind for every operational and accidental condition including LOCA accident. The second role of these spacers is to maintain annular cross-sectional flow area along the test section.

Two spacers are positioned near the inlet and outlet area and two remaining are right between thermocouple positions. The pitch of spacers is the same as for thermocouples, i.e. $0.5\,m$. The spacer element is $10\,mm$ high and it is made of stainless steel tube of thickness $0.2\,mm$. Spacers were created in-site using simple manufacturing process which is shown in Figure 6.7.
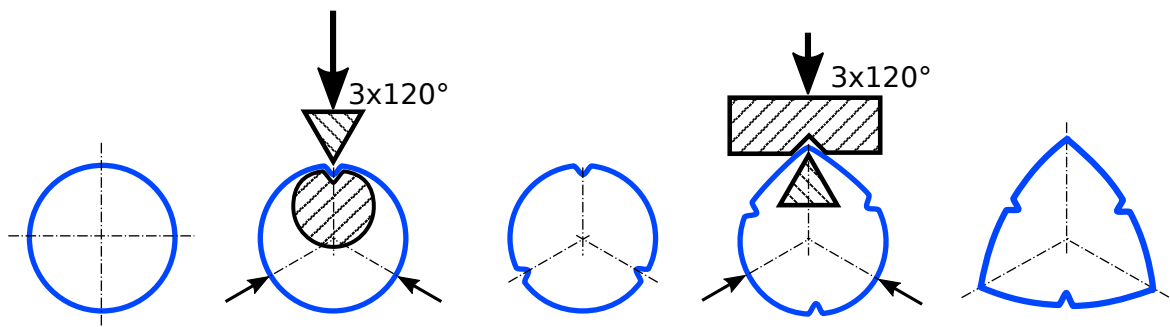
Figure 6.7: Spacer element manufacturing process

The final shape of the element positioned on the heated tube inside the test section is shown in Figure 6.8. The spacer keeps its position due to the elastic force of the spacer itself.
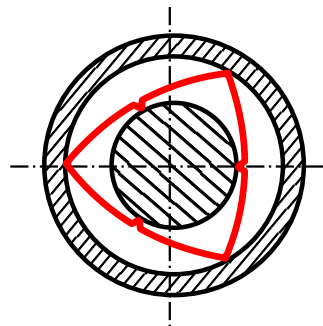
Figure 6.8: Spacer inside the annular flow area

Positions of all spacers within the test section are in Table 6.7. (Spacers are centered at their position)

Table 6.7: Positions of spacers

	Position relative to:		
Spacer no.	Pressure sensor	Annulus inlet	Heated length
1	$330\,mm$	$295\,mm$	$85\,mm$
2	$830\,mm$	$795\,mm$	$585\,mm$
3	$1330\,mm$	$1295\,mm$	$1085\,mm$
4	$1830\,mm$	$1795\,mm$	$1585\,mm$

6.3.4 Pressure Sensor

Relative pressure under the test section in the lower node is measured by the relative pressure sensor. Originally, the relative pressure was measured in both chambers - lower and upper. However, preliminary experiments showed, that upper pressure is not influenced by the flooding of the test section. The upper relative pressure was expelled from data acquisition system for this reason. Lower chamber sensor then represents the actual sum of hydrostatic pressure and pressure drop of the test section.

The relative pressure sensor Cressto TM G537 A3G with the ceramic membrane was used in the device. Parameters of the sensor are in Table 6.8 and its connection scheme is in Figure 6.9.

Table 6.8: Relative pressure sensor parameters

Type	Cressto TM G537 A3G
Pressure	$0 - 250\,kPa$
Input (Design)	$12 - 36\,V$
Input (Used)	$24\,V$
Output	$0 - 20\,mA$
Resistor (R_{press})	$499.0\,\Omega$
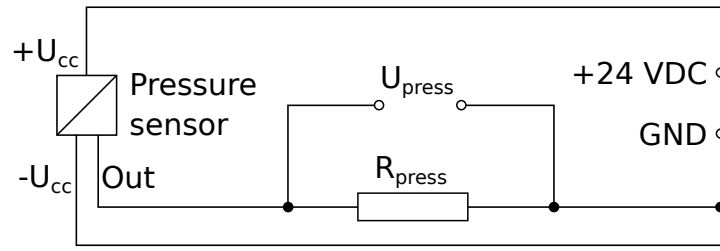
Figure 6.9: Pressure sensor connection scheme

The measured value is the voltage U_{press} (see Figure 6.9). The voltage is transferred to pressure using Equation 6.16 and 6.17:

$$p_{relM} = \frac{U_{press} \cdot p_{max}}{R_{press} \cdot I_{max}} = \frac{U_{press} \cdot 250\mathrm{e}3}{499 \cdot 20\mathrm{e}{-3}} \quad [Pa] \tag{6.16}$$

or

$$p_{relM} = K_{press} \cdot U_{press} \quad [Pa] \quad where \quad K_{press} = 25050\,Pa.V^{-1} \tag{6.17}$$

where $U_{press}\,[V]$ is the measured voltage and $p_{relM}\,[Pa]$ is the resulting measured relative pressure.

6.3.4.1 Pressure Sensor Calibration

The pressure sensor was calibrated by measuring hydrostatic pressure of water column with known height. For this purpose, the cold test section was used. The water column height was red from the mm scale attached to the glass tube. There was chosen several water column levels at which pressure was scanned (eight times each).

The reference correct value was calculated as hydrostatic pressure:

$$p_h = \rho \cdot g \cdot H \quad [Pa] \tag{6.18}$$

where $\rho = 999\,[kg.m^{-3}]$ is the density of water at actual temperature ($16\,°C$), $g\,[m.s^{-2}]$ is gravitational acceleration (Prague, Czech Republic $g = 9.81373\,m.s^{-2}$) and $H\,[m]$ is height of the water column. Absolute error was subsequently calculated as a difference between reference value and actual measured pressure value. These results are plotted in Figure 6.10.
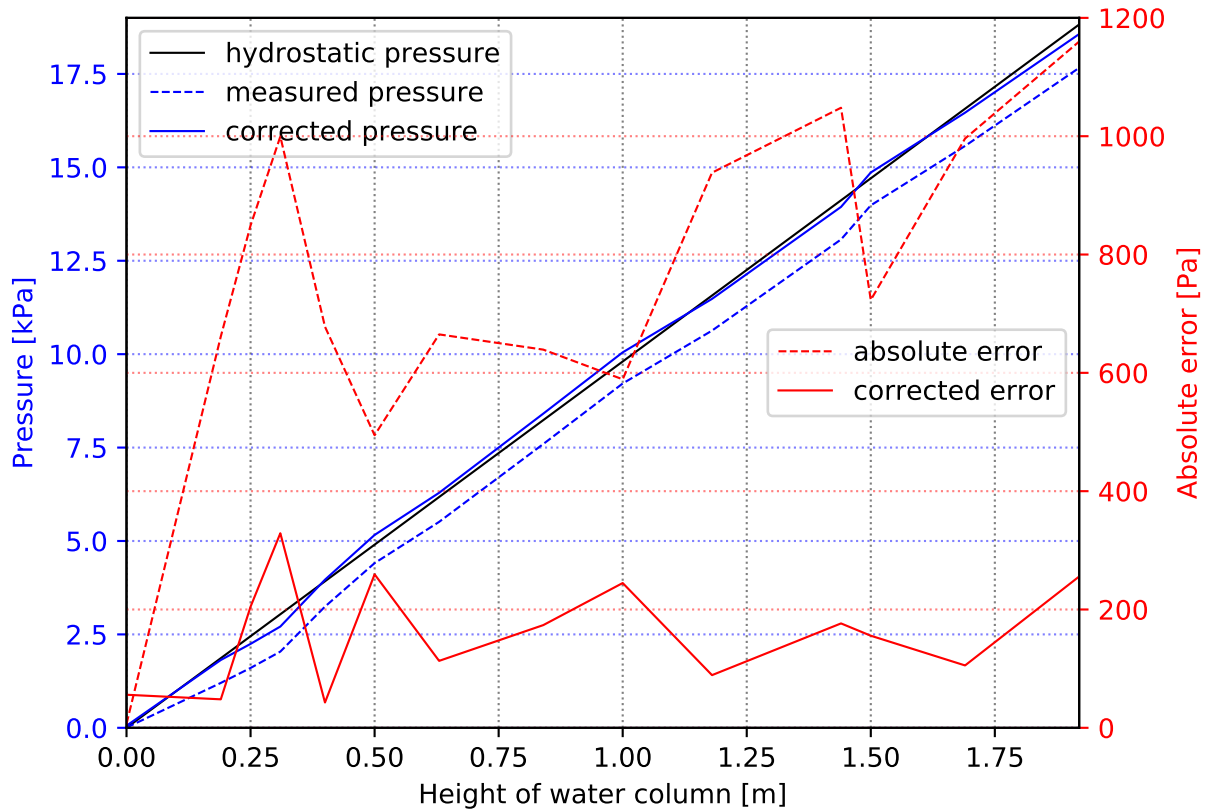
Figure 6.10: Pressure sensor calibration

The resulting absolute error was approximated with logarithmic function, due to its profile, and from this approximation, a correction equation for pressure was created. The correction function is in Equation 6.19. The corrected pressure profile and its absolute error are in Figure 6.10. The MAE (Mean Absolute Error) value for corrected pressure values is $\pm 160\,Pa$.

$$p_{corr} = 108.2535 \cdot ln(p_{relM}) - 154.4 \quad [Pa] \tag{6.19}$$

$$p_{rel} = p_{relM} + p_{corr} \quad [Pa] \tag{6.20}$$

or directly from measured voltage U_{press} (see Equation 6.17):

$$p_{rel} = K_{press} \cdot U_{press} + 127.755 \cdot ln(U_{press}) + 1017 \quad [Pa] \tag{6.21}$$

where $U_{press}\,[V]$ is the measured voltage, $K_{press}\,[-]$ is pressure sensor constant (see Equation 6.17) and $p_{rel}\,[Pa]$ is corrected measured pressure.

6.4   Power Source

DC current supply into the test section was ensured by welder ČKD KS250. It is a thyristor welding rectifier from 70's and it was made in formal Czechoslovakia. It is an easily accessible heavy-duty source of DC power. Preliminary tests showed, that KS250 is suitable and reliable power source solution. The welder is connected to copper electrodes of the heated tube through the manually operated contactor. Maximum provided direct current of the welder is, as can be evident from its name, $250\,A$.

6.4.1   Input Power Measurement

The value of actual input power of the test section was calculated from the voltage at welder output contacts and shunt resistor voltage drop. The shunt resistor parameters are in Table 6.9. The electrical scheme is in Figure 6.11.
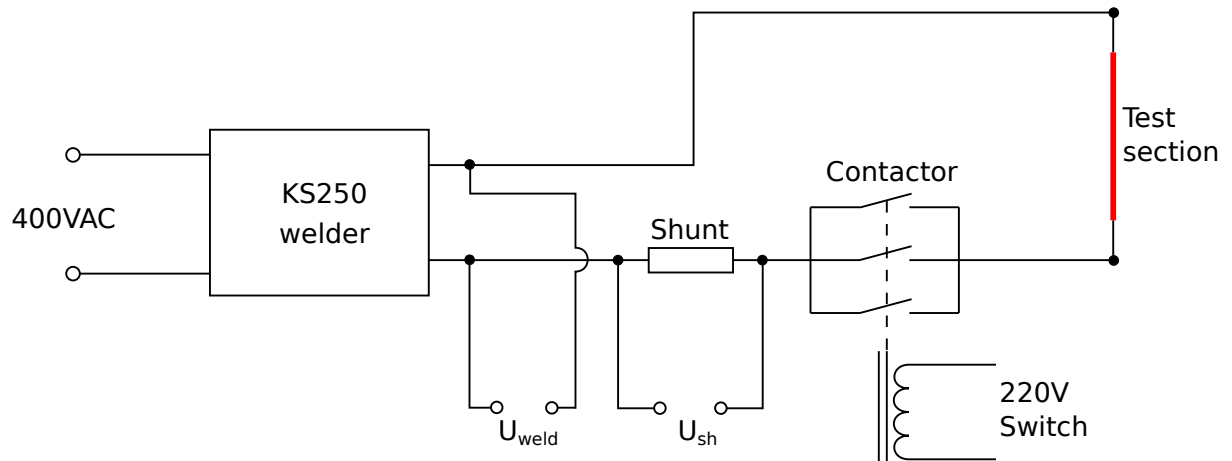
Figure 6.11: DC current input scheme

Table 6.9: Shunt resistor parameters

Current (I_{sh})	$0 - 250\,A$
Voltage drop (U_{sh})	$0 - 50\,mV$

Scanned voltages were converted to input power $P_{in}\,[W]$ using Equation 6.22.

$$P_{in} = U_{weld} \cdot I_{weld} = U_{weld} \cdot \frac{U_{sh}}{U_{shmax}} \cdot I_{shmax} = U_{weld} \cdot \frac{U_{sh}}{0.05} \cdot 250 = 5000 \cdot U_{weld} \cdot U_{sh} \quad (6.22)$$

where $U_{weld}\,[V]$ is the welder output voltage and $U_{sh}\,[V]$ is the shunt resistor voltage drop.

6.5 Data Logger

For real-time experimental data logging Agilent (Keysight) 34972A unit connected to the laptop was used. The data logger is equipped with a multiplexer 34901A with 20+2 channels. The 20-channel general multiplexer main features are 60ch/s scanning, two-wire and four-wire scanning and built-in thermocouple reference junction [80]. The basic DCV accuracy of the logger is 0.004%. However, it is included in each equipment calibration as described in previous sections.

Figure 6.12: Agilent/Keysight 34972A data logger [80]

6.6 Conclusion

All parts of the experimental loop and the loop itself were described in this chapter. The loop is equipped with temperature, flow rate, pressure and power measurement with respect to investigated process and its parameters.

Chapter 7

Experiment Setup and Methodology

Experimental methodology is described in this chapter. The measuring process can be summed up in the following three steps:

- Flow rate setup

- Test section heating

- Flooding

Each experimental point, i.e. given initial wall temperature and flow rate, was measured at least three times ideally five times. The number of minimum three repetitions was chosen due to degradation of silver solder at high temperatures. This precaution ensured the correct surface temperature measurement.

7.1   Flow Rate Setup

The desired investigated initial flow rate was chosen at four levels: 80, 110, 190 and 270 $kg.m^{-2}.s^{-1}$. These values were chosen with taking into account easy readability of the value in frequency on data logger display during experiment run. The corresponding frequency values are 11, 20, 40 and 60 Hz for the turbine flow meter.

The given flow rate was adjusted by throttle valve behind the circulation pump in "Short Loop" configuration of the test loop (see Figure 6.1 on page 60). The flow rate between "Short Loop" and "Open Loop" configuration slightly differs due to different hydraulic conditions, but the flow rate level can be set in this way. During the reflooding of the test section, the flow rate decreases approximately by 20 % because of rising hydrostatic pressure and pressure drop caused by dynamic processes within the annular

channel. The set flow rate in "Short Loop" corresponds to flow rate at the half height of the test section.

7.2   Heating of the Model

The tube - model inside the annular channel was heated by direct electrical heating. The heating process was initiated by switching on the contactor in the electrical circuit of the welder (see Figure 6.11 on page 76). The surface temperature of the tube was continuously scanned at three points via thermocouples TC1, TC2, and TC3. The annular channel remains completely dry during the heating process. When thermocouples reached the desired initial wall temperature, the electric current was stabilized at corresponding value.

The investigated temperature levels are within the range from $250\,^\circ C$ to $700\,^\circ C$ with the temperature step of $50\,^\circ C$.

The initial wall temperature for the tube with variable wall thickness (Model C) was driven by the warmest thermocouple, i.e. the third thermocouple (TC3) with the thinnest wall. In the case of models A and B, the initial surface temperature scattering for all thermocouples was under $\pm 5\,^\circ C$.

The heating was maintained at given temperature level until the thermocouple positioned on the outside surface of the silica glass tube reached steady state. The heat generated by the electric current within the steel tube is equal to escaping heat through the outer barrier at this moment. The configuration of the hydraulic circuit was then changed by valves from "Short Loop" to "Open Loop" configuration and flooding process begun.

7.3   Flooding

The flooding process does not require the intervention of the experimenter until the flooding process is finished, i.e. the test section is full of water.

When done, the test loop configuration was switched back to "Short Loop" and DC current source was disconnected. Then water inside the test section was drained and new water was added into the hydraulic circuit to cover the loss of water during the experiment run.

7.4   Initial Conditions - Summary

All initial wall temperature level are in Table 7.1 and initial flow rates in Table 7.2. These conditions were set for each model in the same way. This gives 140 experiments per model. In total, 420 experiments were performed and evaluated consequently.

Table 7.1: Initial wall temperatures

Initial wall temperature levels T_0 $[°C]$									
250	300	350	400	450	500	550	600	650	700

Table 7.2: Initial mass flow rates

Initial mass flow rates G $[kg.m^{-2}.s^{-1}]$ (reps.)			
80 (3)	110 (5)	190 (3)	270 (3)

Chapter 8

Supplementary Study on Spacer Grid Effect

The previous study by Štěpánek and Bláha (2015)[A2] describing the spacer effect is summarized in this chapter. These results were based on experimental data by Bláha (1983) (never published).

8.1 Parameters of the Experiment

The experimental work initial parameters were follows:

- Bottom flooding regime

- Inlet water temperature of $50\,°C$

- Initial wall temperature of $580\,°C$

- Coolant mass flux of $150\,kg.m^{-2}.s^{-1}$

- Wall heat flux (computed from voltage and current in the electrical circuit) $22\,kW.m^{-2}$

- Atmospheric pressure

8.2 Construction of the Probe

The main target of the effort was to measure the temperature field around the spacer. Obtained data were used for the description of the quench front propagation. For this purpose, a set of thermocouples near the spacer is needed. These thermocouples are soldered to the wall from the inside. This construction gives a good information on the wall temperature. The thermocouple's positions are follows (see Figure 8.1):
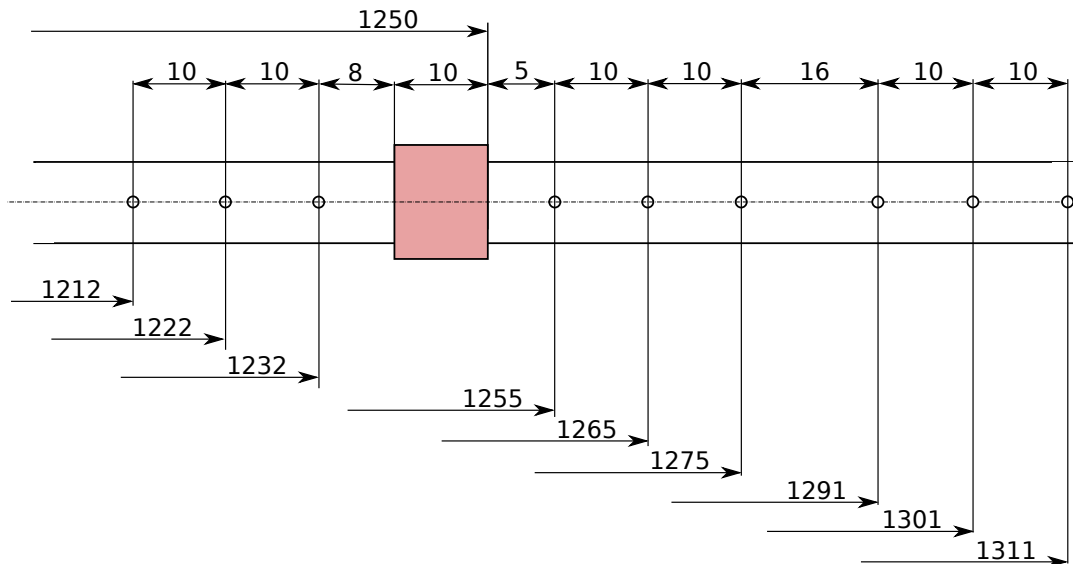
Figure 8.1: Positions of thermocouples near the spacer

Bellow the bottom edge of the spacer

1. 28 mm, 2. 18 mm, 3. 8 mm

Above the top edge of the spacer

4. 5 mm, 5. 15 mm, 6. 25 mm

The spacer was placed 1250 mm behind the inlet.

8.2.1 Visually Observable Behavior Near the Spacer

At first sight, two quench fronts near the spacer can be observed. The first - primary quench front moving relatively fast along the tube and secondary quench front in front of the spacer. Behind the primary quench front, there are no dry regions. The secondary quench front begins to be observable while the primary quench front is close enough to the spacer (10 cm or less). As the secondary quench front moves away from the spacer there is a column of water created. This column is about 1-3 cm high. The secondary quench front velocity (U_1 in Figure 8.2) is very low and no significant bubbly boiling occurs in its area.

As primary quench front, with the velocity of U in Figure 8.2, reaches the spacer, the secondary quench front becomes the primary one. This transformation of the quench fronts may be understood as a prompt jump of the primary front.

Moreover, while the secondary front is present above the spacer, a thin tertiary quench front moving downwards may cool down the surface of the tube under the spacer. Its

velocity (U_2 in Figure 8.2) is very low compared to the velocity of the primary quench front.
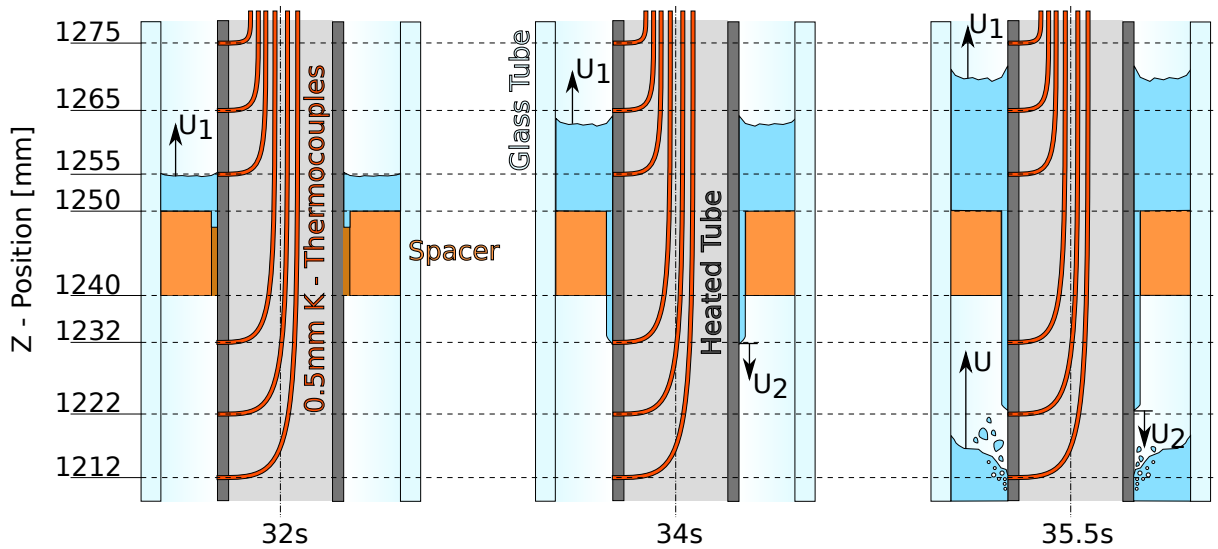
Figure 8.2: Primary, secondary and tertiary quench front near the spacer

(Coloured lines correspond to individual thermocouples)

The conclusion of this work was, that quenching of fuel rods equipped with spacers will be not a coherent process with just one advancing quench front, but several quench fronts will occur near the spacers. These quench fronts have different directions and velocities. This means, that many local centers along the cooled geometry will generate its own quench fronts with influence on the rewetting process. Because of this quenching behavior, we can't determine the exact location, which will be rewetted as the last one.

Chapter 9

Individual Data Processing

Before the full-scale data evaluation, each data set passed through individual evaluation. This step contains a calculation of average quench front velocities, surface heat fluxes, evaluation of temperature profiles and its derivatives, identification of quenching and rewetting temperatures, calculation of heat transfer coefficients, pressure drops and etc. The data processing scripts are written in the Python v.3.6.4 programming language supplemented by numerical python libraries (NumPy v.1.14) and scientific python (SciPy v.1.0). Water and steam properties are calculated through python implementation of standards from the International Association for the Properties of Water and Steam (iapws v.1.2). The process is described in detail in this chapter. Figure 9.1 represents simplified scheme of the data processing script and all its important parts are described in following sections.
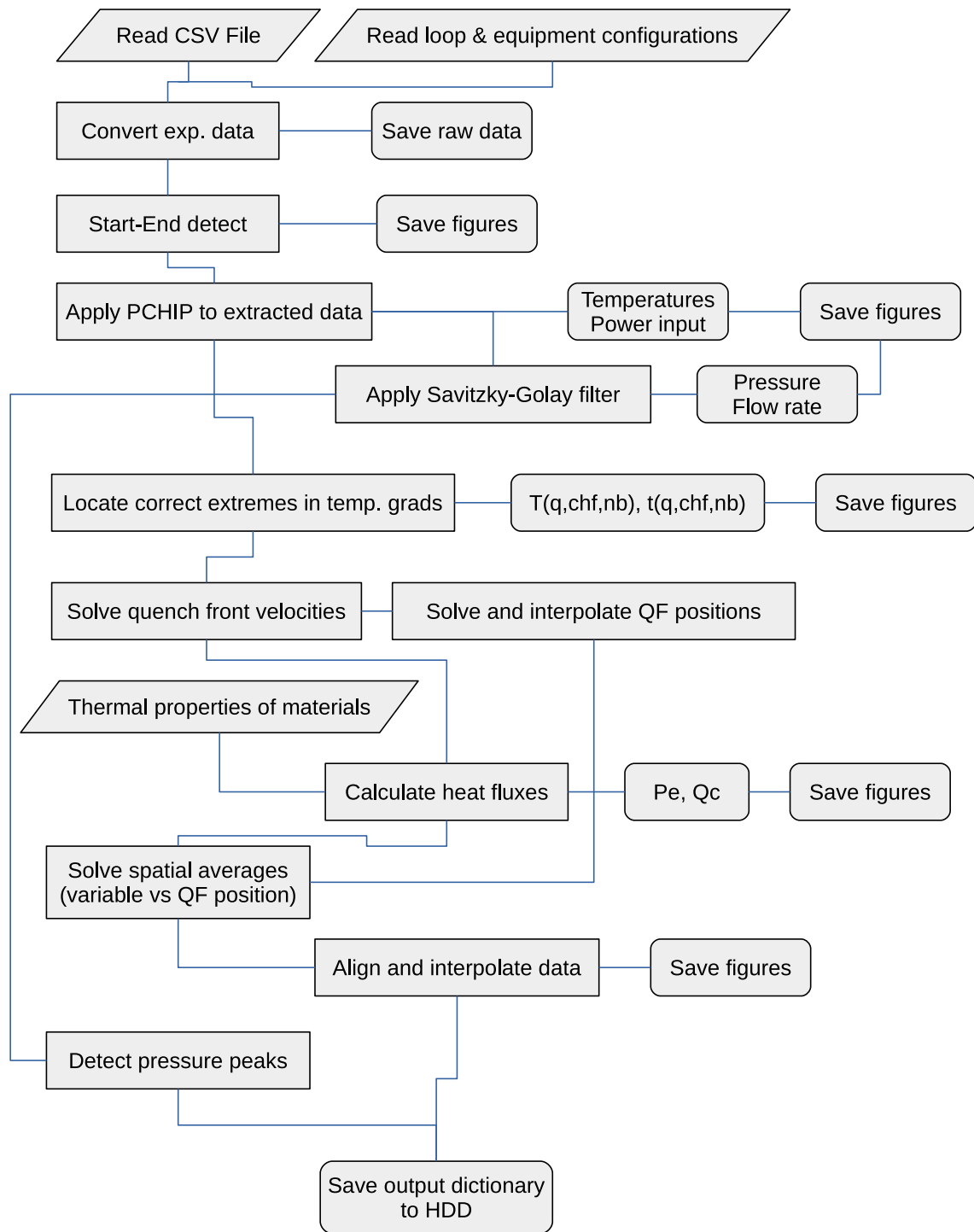
Figure 9.1: Individual data processing script - simplified scheme

9.1   Start-End Detection

Full datasets of each experiment are converted and stored on a hard drive with corresponding full-scale plots for further possible analyses. Subsequently, the flooding phase of the experiment is extracted from these sets. The extraction process is done automatically by the specialized script. The beginning of the flooding phase is detected through the

first order derivative of the pressure. The rapid pressure increase occurs while the coolant enters annular flow channel. This rapid change can be easily found in the pressure array though set pressure gradient threshold. If pressure gradient is higher than this threshold, the script searches for its local minimum backward in time. This process is shown in Figure 9.2.
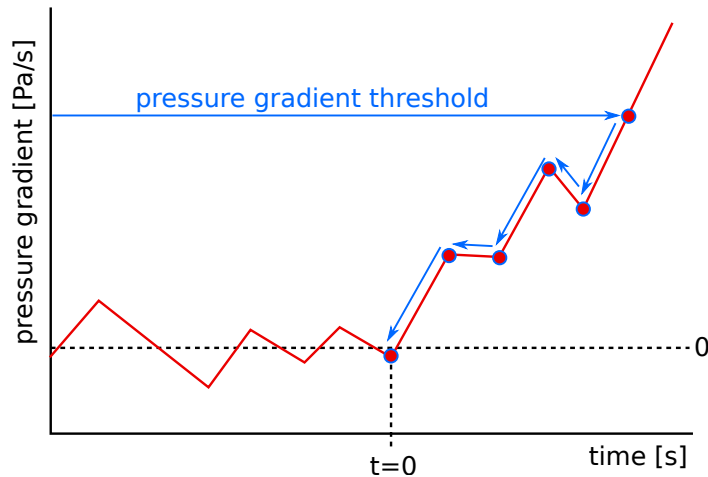
Figure 9.2: Detection of beginning of flooding in measured pressure data

The end is detected in several ways. The end of the experiment can be done in the laboratory by input power disconnection, coolant flow closure or by scanning process interruption. These interruptions are found in the dataset by searching for electric current zero values or for no frequency input from turbine flow meter. Otherwise the last measured point is the endpoint. The reason for flooding interruption by experimenter is fully flooded test section.

9.2 Experimental Data Interpolation

First of all, data scanned by data logger need to be interpolated eventually filtered for further evaluation because obtained experimental data represent discrete values of physical quantities. If we want to perform various calculations, these points have to be interpolated by the continuous function with continuous first order derivative.

Measured and scanned variables are:

- Time

- Coolant flow rate

- Coolant inlet temperature

- Heated tube surface temperatures by thermocouples TC1, TC2, and TC3

- Silica glass surface temperature

- Lower chamber relative pressure

- Welder and shunt resistor voltage drops, i.e. input power

Preliminary calculations were evaluated using cubic spline interpolation method. This method proved to be unsuitable for obtained experimental data near the rapid temperature decrease near the quench front. On the one hand, the resulting curve is very smooth and continuous. But due to its smooth character, it overestimates temperatures near the upper and lower edge of the temperature profile. On top of that, the region with the minimum value of first-order derivative (i.e. region of critical heat flux) is also affected by the smooth interpolation.

Figure 9.3: PCHIP vs Spline experimental data interpolation

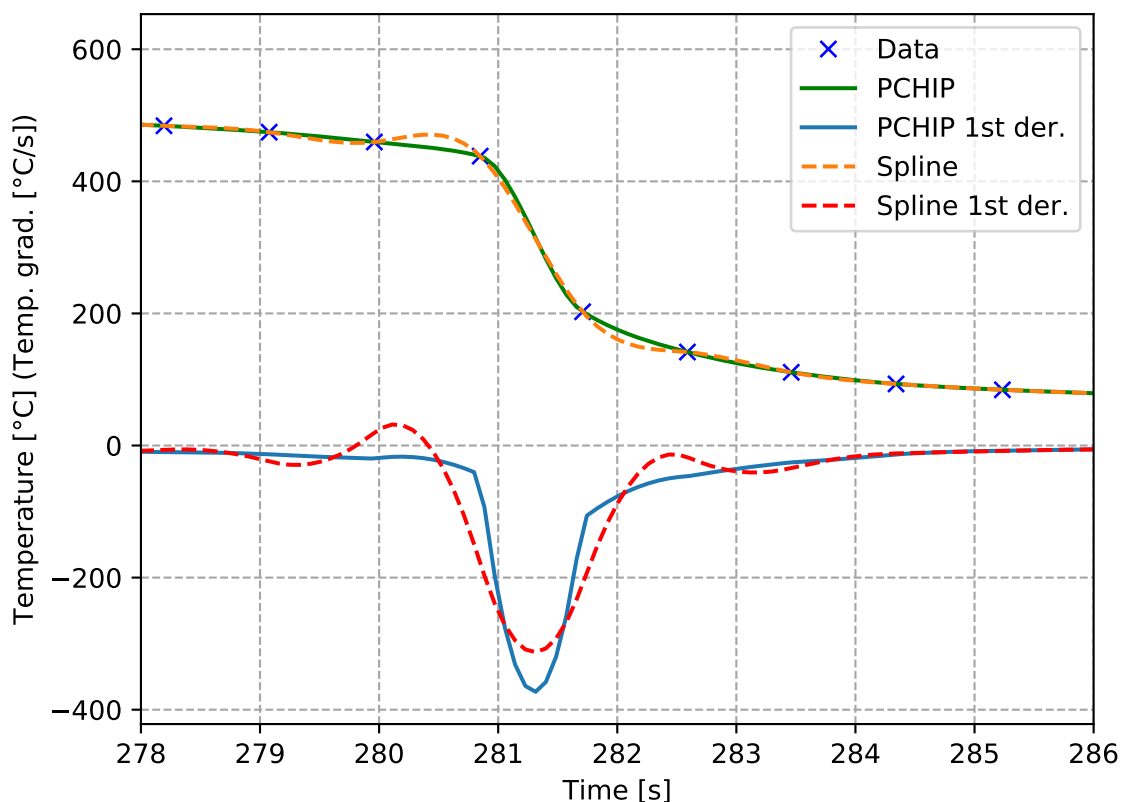Several other methods for data interpolation were probed subsequently. The best-proved interpolation method for given data was a Piecewise Cubic Hermite Interpolation Polynomial (PCHIP). The main difference between the spline and PCHIP curve is that PCHIP

does not overestimate temperatures near the edges in temperature profile and the curve looks more natural and credible. [A3] As it turned out, spline and PCHIP can be used for identification of the position of critical heat flux and second derivative extremes. But the main lack of spline and similar functions is an underestimation of the maximum first-order derivative value, which is used for heat flux and heat transfer coefficient calculation. The difference between the spline and PCHIP interpolation is shown in Figure 9.3. As it can be evident, the maximum absolute value of the first order derivative is for spline lower approximately by 20 %.

The number of interpolated points between the experimental ones is a function of flow rate. The data logger collects a specific number of pulses to evaluate the frequency, thus a scanning frequency is dependent on the given flow rate. A variable called fin was defined in numerical interpolation script and it represents a number of interpolated points. From results a floor of thirteenth fraction of initial mass flux $G_i[kg.m^{-2}.s^{-1}]$ was used.

$$fin = \left\lfloor \frac{G_i}{13} \right\rfloor \tag{9.1}$$

9.3 Experimental Data Filtration

Some experimental data needs to be filtered in order to get more consistent and clear flow of the specific variable. The filtered data in the presented experiment were variables, which show very frequent small chaotic changes around mean value. The filtered variable was pressure, flow rate, and electric current. For this purpose, a Savitzky-Golay filter was used. Savitzky-Golay filtering can be thought of as a generalized moving average. You derive the filter coefficients by performing an unweighted linear least-squares fit using a polynomial of a given degree. For this reason, a Savitzky-Golay filter is also called a digital smoothing polynomial filter or a least-squares smoothing filter. Note that a higher degree polynomial makes it possible to achieve a high level of smoothing without attenuation of data features. [81]

Usage of Savitzky-Golay filter requires two parameters: window length and degree. Window length represents a number of coefficients and degree is the order of the polynomial used to fit the samples. The formula for window length calculation is in Equation 9.2. The formula is based on later experience in data processing. It must be a positive odd integer.

$$W_l = \left\lceil N_s \cdot 0.33 \right\rceil \cdot 2 + 1 \qquad (9.2)$$

where $N_s[-]$ is number of nodes in the filtered data sample. The degree of the filter was taken as a floor half of the window length:

$$D_f = \left\lfloor \frac{W_l}{2} \right\rfloor \qquad (9.3)$$

A filtered relative pressure data sample is shown in Figure 9.4 bellow.
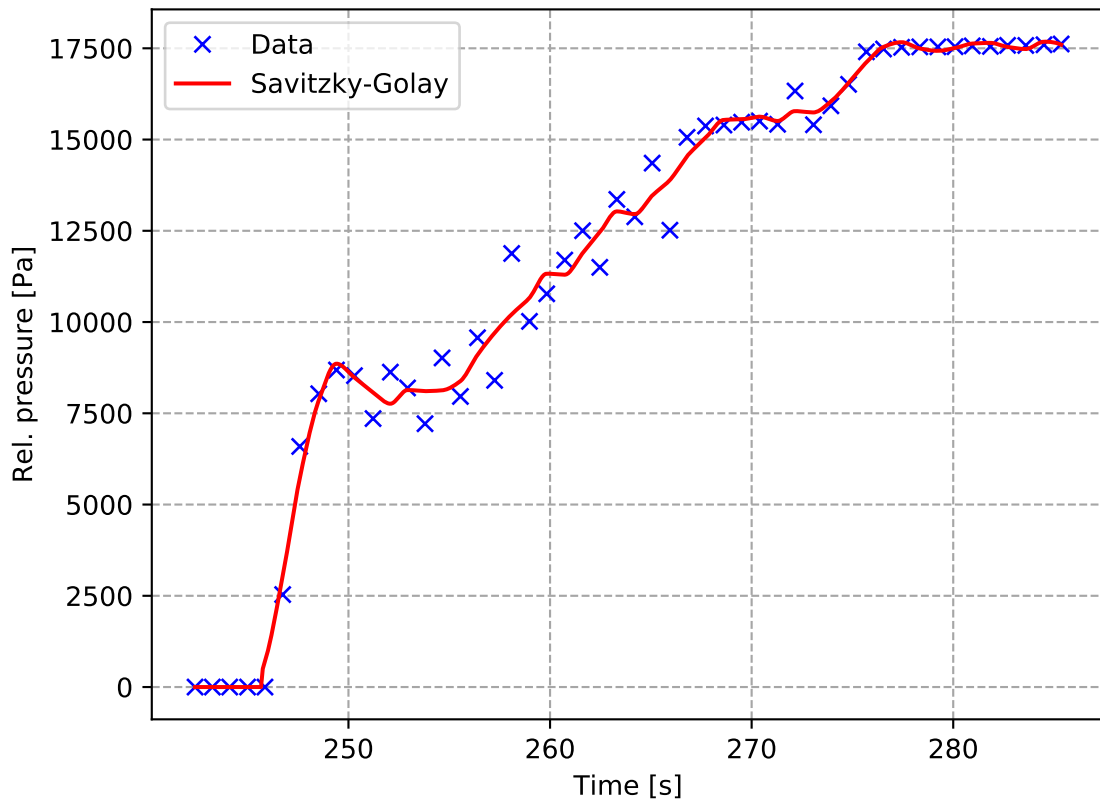
Figure 9.4: Savitzky-Golay filter applied to relative pressure data

9.4   Quenching and CHF Temperature Detection

As it was mentioned in Section 1.4 on page 27, the quenching temperature is defined at the position in temperature profile with the minimum second order derivative of temperature. While the scanned points are equidistant in time, Equations 9.4 and 9.5 can

be used for the first order and second order temperature derivation respectively. These equations are applied on interpolated temperature arrays.

$$T'_t = \frac{T_{t+\Delta t} - T_{t-\Delta t}}{2\Delta t} \qquad [K.s^{-1}] \qquad (9.4)$$

$$T''_t = \frac{T_{t+\Delta t} - 2T_t + T_{t-\Delta t}}{\Delta t^2} \qquad [K.s^{-2}] \qquad (9.5)$$

where $t\,[s]$ is given time moment (and corresponding array index), $T\,[°C]$ is the temperature and $\Delta t\,[s]$ is size of the time step defined as (i is for array index):

$$\Delta t = t_{i+1} - t_i \qquad [s] \qquad (9.6)$$

Using these derivatives, positions of individual important temperatures were found:

- Quenching temperature T_q - position of the minimum second order derivative

- Critical heat flux temperature T_{chf} - position of the minimum first order derivative

- (Nucleate boiling temperature T_{nb} - position of the maximum second order derivative)
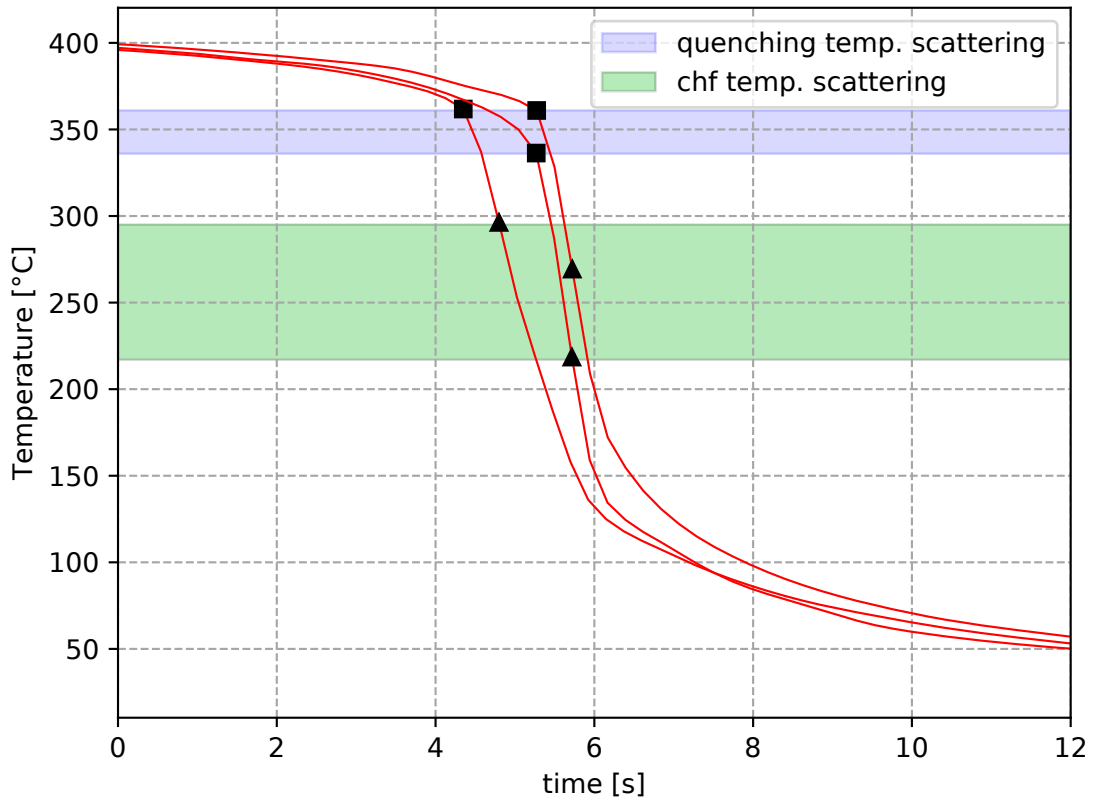
Figure 9.5: Quenching and CHF temperatures on temperature profiles

Figure 9.5 shows detected quenching and CHF temperatures for selected temperature profile. As can be seen, quenching temperatures show less scattering than CHF temperature. However, CHF temperatures are less scattered in time for most cases because the first order derivative can be found in data with greater certainty, despite the actual different moments of reading the temperature values. CHF temperatures were chosen for calculation of mean quench front velocity for this reason.

9.5 Quench Front Velocity

Quench front velocity is defined as a known distance overcome in a measured time interval. The known distance is, in this case, the pitch of two thermocouples. The chosen easily recognizable moment is the position of the minimum first order derivative of temperature profile as declared in the previous section. Each temperature has assigned a time point, for example T_{1chf} is located at t_{1chf}. The average quench front velocity between thermocouples TC1 and TC2 is then calculated as:

$$u_{12} = \frac{L_{h2} - L_{h1}}{\Delta t_{12}} = \frac{0.5}{t_{2chf} - t_{1chf}} \qquad [m.s^{-1}] \qquad (9.7)$$

the quench front velocity between thermocouples TC2 and TC3 is calculated analogously:

$$u_{23} = \frac{L_{h3} - L_{h2}}{\Delta t_{23}} = \frac{0.5}{t_{3chf} - t_{2chf}} \qquad [m.s^{-1}] \qquad (9.8)$$

and finally, the average quench front velocity between thermocouples TC1 and TC3:

$$u_{13} = \frac{L_{h3} - L_{h1}}{\Delta t_{13}} = \frac{1.0}{t_{3chf} - t_{1chf}} \qquad [m.s^{-1}] \qquad (9.9)$$

Moreover an average quench front velocity between bottom edge of the heated tube and the first thermocouple can be calculated. The unheated part of the test section is $0.21\,m$ long. From known inlet coolant mass flux and the length of the unheated annulus the zero time (originally detected from pressure derivative) is shifted by Δt_{in}:

$$\Delta t_{in} = \frac{L_{nh}}{c_{in}} = \frac{0.21 \cdot \rho_{in}}{G_{in}} \qquad [s] \qquad (9.10)$$

while the measured time is shifted backwards, the resulting quench front velocity between bottom edge of the heated tube and the first thermocouple can be expressed as:

$$u_{01} = \frac{L_{h1}}{t_{1chf}} = \frac{0.335}{t_{1chf}} \qquad [m.s^{-1}] \qquad (9.11)$$

Figure 9.6 shows temperature profiles of TC1, TC2 and TC3 thermocouples with marked CHF temperatures. The time interval between zero time and quench time of the first thermocouple is at first glance shorter. It is caused not only by the shorter distance between bottom heated edge and thermocouple position but also by the inertia of the coolant moving at high speed through the unheated annulus. When the water meets the overheated surface a significant pressure peak can be observed and the water speed rapidly decreases. However, the resulting average velocity is higher in this first region. This quench front velocity is not used for final quench front velocity correlations (due to its evident relative inaccuracy) but only for rough estimation of the quench front position in this region.
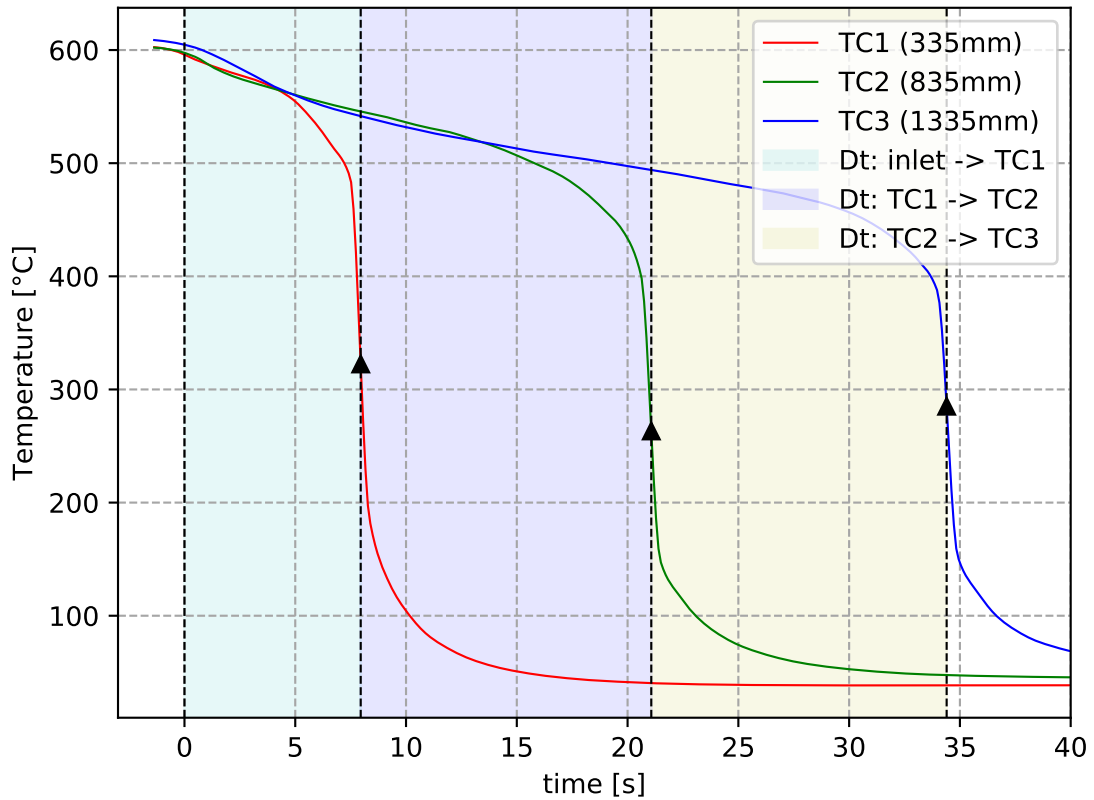
Figure 9.6: Quenching intervals for quench front velocity calculations

9.6 Quench Front Position

For further calculations and data evaluations, a simple quench front position script was created. The purpose of the script is to convert time axis into spatial coordinates. Spatially dependent variables can be aligned and they can be compared to each other. This conversion aligns all measured and calculated parameters with respect to known time and spatial points. These points are in Table 9.1. These sets of points are sent in the PCHIP interpolator and a smooth set of spatial points is obtained as a solution.

Table 9.1: Known time and spatial points for quench front prediction polynominal

Position	$-L_{nh}$	0.0	L_{aux}	L_{h1}	L_{h2}	L_{h3}	L_{ht}
Time	$-\Delta t_{in}$	0.0	Δt_{aux}	t_{1chf}	t_{2chf}	t_{3chf}	t_{end}

In the Table 9.1 L_{hi} stands for position of thermocouples TC1, TC2 and TC3 according to bottom edge of heated tube, L_{ht} is the total heated length (see Table 6.6 on page 71)

and L_{nh} is length of unheated part of the annular channel. L_{aux} is an auxiliary point for credible smooth velocity profile right after coolant inlet into the heated annulus. The position of this point is related to actual inlet velocity and average quench front velocity in the first region in front of the TC1. The resulting spatial shift is given by average velocity of the inlet velocity and velocity in the first region and chosen time interval of Δt_{aux}. The interval was chosen based on good experience with quench front prediction capability of the code with these values for all experiments. The auxiliary point calculation is showed in Equation 9.12.

$$L_{aux} = \frac{c_{in} + u_{01}}{2} \cdot \Delta t_{aux}$$
$$where$$
$$\Delta t_{aux} = 1.0, 0.6, 0.4, 0.2\, s \quad for \quad G = 80, 110, 190, 270\, kg.m^{-2}.s^{-1}$$
(9.12)

The last point at position of L_{ht} can be obtained by extrapolating the average velocities between each thermocouples. Let's assume a simplification, that average quench front velocities u_{12} and u_{23} are present in the middle of the each section then velocity at the end of the heated tube will be:

$$u_e = (u_{23} - u_{12})\frac{L_{hp} + L_e}{2L_{hp}} + u_{23} \qquad where \qquad L_{hp} = \frac{L_{h3} - L_{h2}}{2}; \quad L_e = L_{ht} - L_{h3} \quad (9.13)$$

L_{hp} is "half pitch" length and L_e is the length of the last heated section behind the last thermocouple. For final calculation of time t_{end} we need average velocity in the last region u_{3e}:

$$u_{3e} = \frac{u_3 + u_e}{2}$$
(9.14)

where

$$u_3 = \frac{3 \cdot u_{23} - u_{12}}{2}$$
(9.15)

and finally

$$t_{end} = t_{3chf} + \frac{L_e}{u_{3e}}$$
(9.16)

Using these complete arrays of positions and according time points the PCHIP interpolator can be applied on the fine time array. The resulting array includes an approximate view on the quench front advance and the first time derivation represents quench front velocity along the test section. Example of the time dependence of quench front position is shown in Figure 9.7.
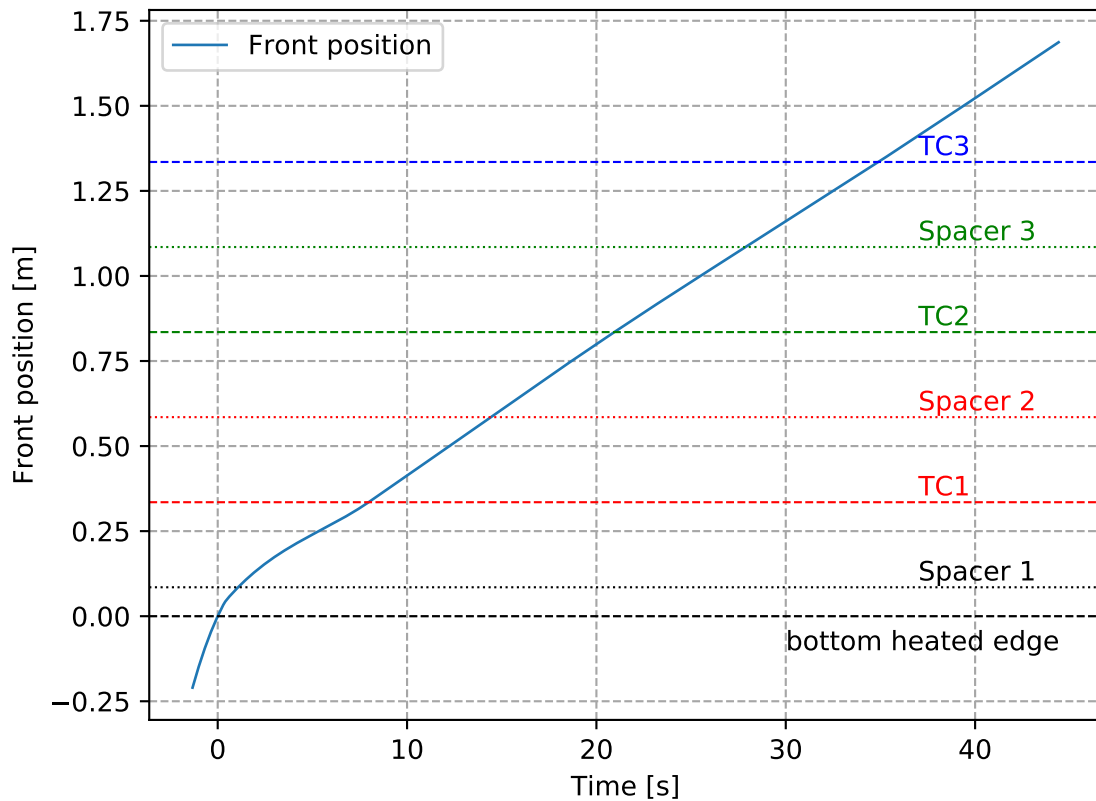
Figure 9.7: Calculated quench front position vs time

Based on Figure 9.7 it can be concluded, that after initial slow down in the bottom part of the test section (up to TC1), the quench front velocity is almost constant. While the water column rises during the flooding and this generates higher pressure drop, the dry region is more and more precooled and this helps the quench front to advance. These two effects go against each other and it keeps velocity nearly constant. This behavior is also observable visually.

9.7 Heat Fluxes

Heat fluxes within the channel must be solved in order to solve heat transfer coefficients. The source of these fluxes is electrically generated heat within the steel wall, which is a function of electrical current and resistance of the wall. The generated heat

is removed by a combination of heat radiation, conduction, and convection through the gap of the annulus. It can be assumed, that radiation escapes directly from the wall through the gap and the silica glass barrier due to its high translucency. Rest of the heat is conducted through the silica glass barrier by conduction and then it escapes to the surroundings. The generated heat is accumulated within the wall up to the initial wall temperature which corresponds to the steady state where heat flux from the wall is equal to the heat loss escaping to the surroundings. In front of the quench front and at the front, saturation temperature is assumed as coolant temperature. Beyond the quench point, the coolant temperature has to be calculated from the water inlet temperature and its enthalpy increase. Mentioned situation and its temperature profile are shown in Figure 9.8. In this figure, P_e is the electrical heat source, Q_c is the heat removed by coolant and Q_g is the escaping heat.
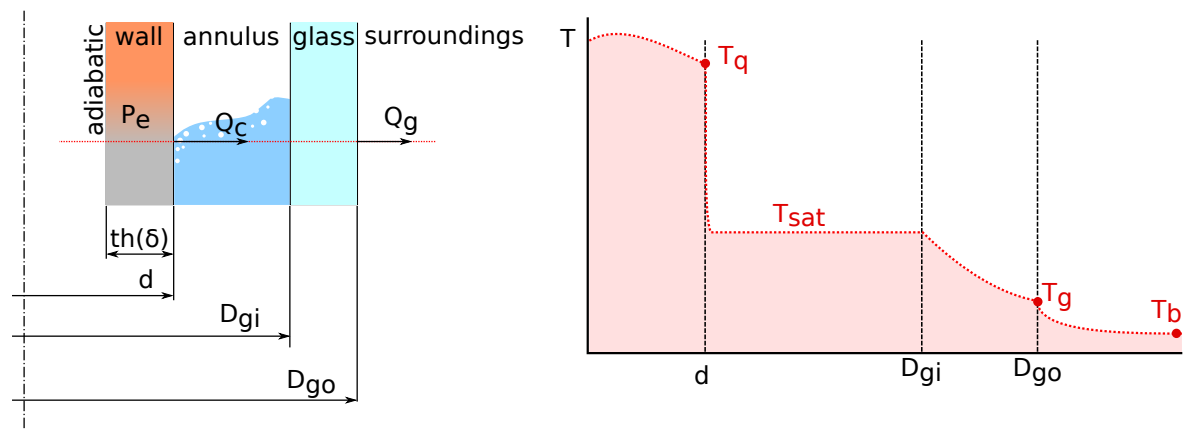
Figure 9.8: Heat fluxes within the channel and its temperature profile at quench time

Note: The temperature profile in Figure 9.8 is only illustrative.

9.7.1 Coolant Heat Flux

The heat within the heated tube's wall is generated by the direct electric current. The current value is measured at shunt resistor behind the welder as described in Section 6.4 on page 76. The generated heat is dependent on wall thickness i.e. cross-sectional area and electric resistance of the tube at individual thermocouple's position and corresponding temperature at given time point.

9.7.1.1 Tube Nodalization

The heat balance was calculated in nodalized geometry at three thermocouples. Evaluation of the heat fluxes was performed for all time points within the interpolated arrays of temperatures and velocities. The essential assumption here is, that time-temperature profile is the same for two spatial nodes at a very short distance. The finite distance named $\Delta z\,[m]$ is calculated from actual quench front velocity and the time step of interpolated time array (see Equation 9.17). This obtaining of node height respects rapid changes of temperatures when the quench front passes the thermocouple. The nodalization is shown in Figure 9.9. The total sum of all heat fluxes (axial-top, axial-bottom, Joule's heat, heat removed by coolant and accumulated heat change) must be equal to zero. The internal tube surface is assumed as adiabatic.

$$\Delta z = u_{[t]} \cdot \Delta t \tag{9.17}$$
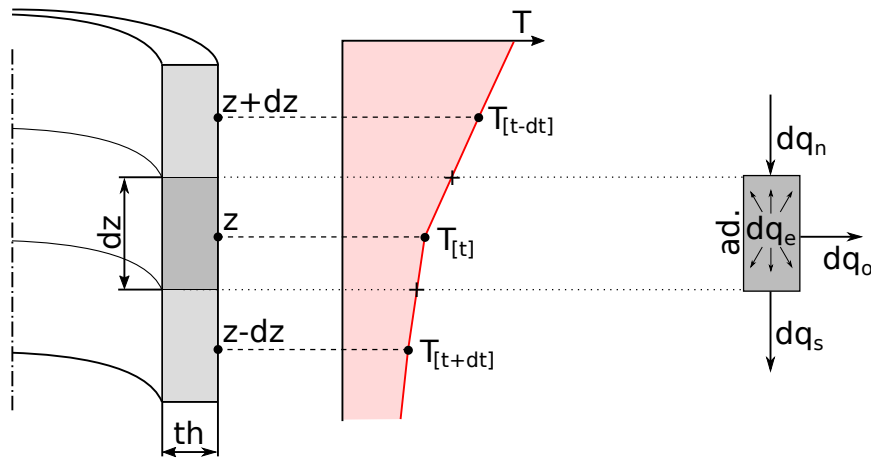
Figure 9.9: Axial nodalization and heat fluxes

9.7.1.2 Heat Flux Balance

The heat balance was calculated including axial heat conduction. The conducted heat is calculated by Fourier's equation in presented spatial nodes as:

$$q_n = k_n \frac{\Delta T_n}{\Delta z} A_z \qquad and \qquad q_s = k_s \frac{\Delta T_s}{\Delta z} A_z \qquad [W] \tag{9.18}$$

where A_z is axial cross-sectional area of the heated tube (the area is assumed to be constant at short distance of Δz):

$$A_z = \frac{\pi}{4}[d^2 - (d - 2 \cdot th_i)^2] \qquad [m^2] \tag{9.19}$$

$th_i\,[m]$ is wall thickness at individual thermocouple axial position. k_n and $k_s\,[W.m^{-1}.K^{-1}]$ are heat conduction coefficients between nodes defined as:

$$k_n = \frac{k(T_{t-\Delta t}) + k(T_t)}{2} \qquad and \qquad k_s = \frac{k(T_{t+\Delta t}) + k(T_t)}{2} \qquad [W.m^{-1}.K^{-1}] \tag{9.20}$$

heat conduction coefficients such as $k(T_{t-\Delta t})$ are functions of temperature and they are evaluated using Equations 6.8 and 6.9 (see page 68) depending on tube's material.

Temperature differences between nodes are defined with respect to heat flow direction as:

$$\Delta T_n = T_{t-\Delta t} - T_t \qquad and \qquad \Delta T_s = T_{t+\Delta t} - T_t \qquad [^\circ C] \tag{9.21}$$

If heat is conducted into the node, then it has a positive sign and negative otherwise. Heat generated within the node by electric current is:

$$q_e = \frac{r(T_t)}{A_z}I^2\Delta z \qquad [W] \tag{9.22}$$

where specific electric resistance $r\,[\Omega.mm^2.m^{-1}]$ is calculated for node temperature using Equation 6.13 eventually 6.12 (page 69) according to tube material.

Finally all heat fluxes in node can be balanced as:

$$\frac{\Delta T_t}{\Delta t}c(T_t)\rho(T_t)A_z\Delta z = q_n + q_s + q_e + q_c \tag{9.23}$$

specific heat c and density ρ are temperature dependent parameters calculated using Equations 6.11,6.10 and 6.15, 6.14 (page 69). Last heat flux of q_c is heat transferred to

coolant and the heat flux is the unknown in this equation.

Moving q_c to the left side of the equation we get:

$$q_c = \frac{\Delta T_t}{\Delta t} c(T_t) \rho(T_t) A_z \Delta z - q_n - q_s - q_e \qquad [W] \qquad (9.24)$$

in full form:

$$q_c = \frac{\Delta T_t}{\Delta t} c(T_t) \rho(T_t) A_z \Delta z - k_n \frac{\Delta T_n}{\Delta z} A_z - k_s \frac{\Delta T_s}{\Delta z} A_z - \frac{r(T_t)}{A_z} I^2 \Delta z \qquad [W] \qquad (9.25)$$

The time derivation of temperature is obtained from original temperature interpolating polynomial. Example of all plotted heats within a single node is in Figure 9.10.
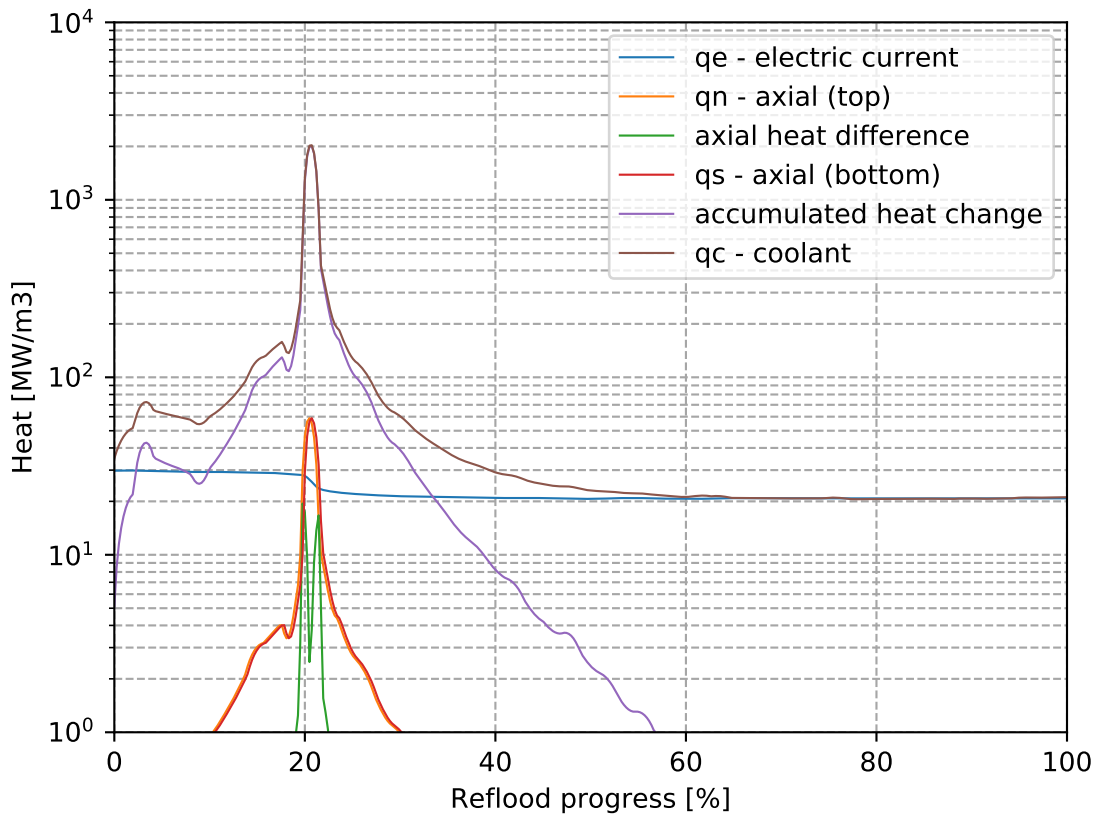
Figure 9.10: Absolute node heats at TC1 ($T_0 = 600\,°C$, Model B, $I = 131\,A$)

From these values it can be concluded, that axial conduction can be neglected in most parts of the process. But near the quenching point and nucleate boiling point are evident peaks of axial heat flux difference. The axial heat flux at the quench point is approximately $15\,\%$ of the total heat flux at this point. This observation supports the

conduction controlled rewetting theory. While precursory cooling pre-cools the geometry, the axial conduction has the last decisive influence on the process.

While the electric power plays its small role, the most prevailing heat to be removed by the coolant is the accumulated heat. Another finding evident from this figure is that in the rear part of the flooding phase, the generated heat is equal to removed heat.

Areal heat flux removed by coolant flows through outer peripheral surface:

$$A_o = \pi d \Delta z \qquad [m^2] \tag{9.26}$$

$$Q_c = \frac{q_c}{A_o} \qquad [W.m^{-2}] \tag{9.27}$$

And this is also an important step towards heat transfer coefficient calculation. Another comparable variable is the volume electrical heat power input i.e. internal heat source term:

$$P_e = \frac{q_e}{V_n} = \frac{q_e}{A_z \Delta z} \qquad [W.m^{-3}] \tag{9.28}$$

In Figure 9.11 bellow, there is plotted an example case of heat fluxes into the coolant. These data are aligned using predicted quench front position function. The three peaks correspond to thermocouple positions along the test section. Labeled lines represent individual repeated measuring.
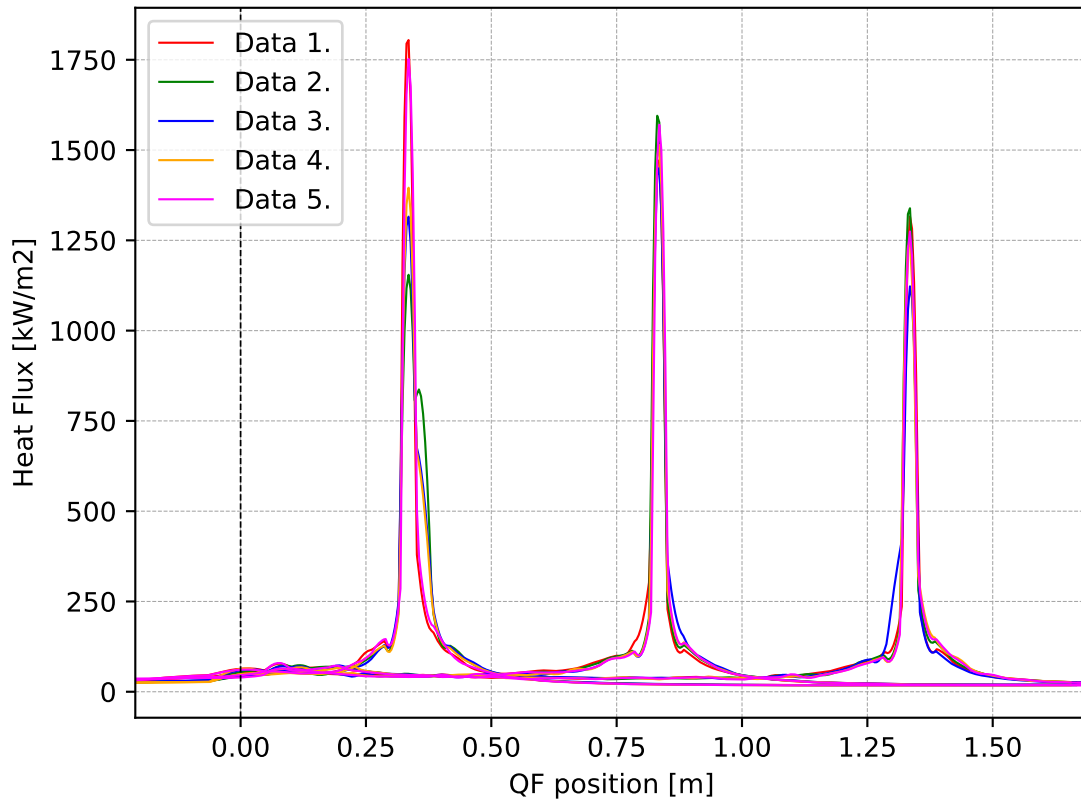
Figure 9.11: Absolute coolant heat fluxes vs QF position ($T_0 = 600\,^\circ C$, Model B)

9.7.2 Silica Glass Tube Heat Flux

A simplified heat flux calculation was applied on the silica glass outer barrier. The barrier is equipped with the thermocouple at the same position as the second thermocouple in the heated wall ($835\,mm$). The main difference between glass and heated tube approach is, that silica glass has no internal heat source and also axial conduction was neglected in this case. Another simplification is the use of constant silica glass physical properties:

Table 9.2: Physical properties of silica glass

$$c_g = 1051.7\,[J.kg^{-1}.K^{-1}]$$

$$\rho_g = 2203\,[kg.m^{-3}]$$

Geometrical parameters of the tube are listed in Table 6.5 on page 66. The areal heat flux can be then expressed as:

$$Q_g = \frac{\frac{dT_g}{dt}c_g\rho_g A_{zg}(1)}{A_{og}(1)} = \frac{\frac{dT_g}{dt}c_g\rho_g \frac{\pi(D_{go}^2 - D_{gi}^2)}{4}}{\pi D_{go}} = \frac{\frac{dT_g}{dt}c_g\rho_g \frac{\pi(18^2 - 14.5^2)}{4 \cdot 10^6}}{\pi 18 \cdot 10^{-3}} \quad [W.m^{-2}]$$

$$(9.29)$$

Assuming constant properties it can be expressed in simplified form involving "glass barrier constant" C_g:

$$Q_g = \frac{dT_g}{dt}C_g \quad [W.m^{-2}] \qquad where \qquad C_g = 3660\,[-] \tag{9.30}$$
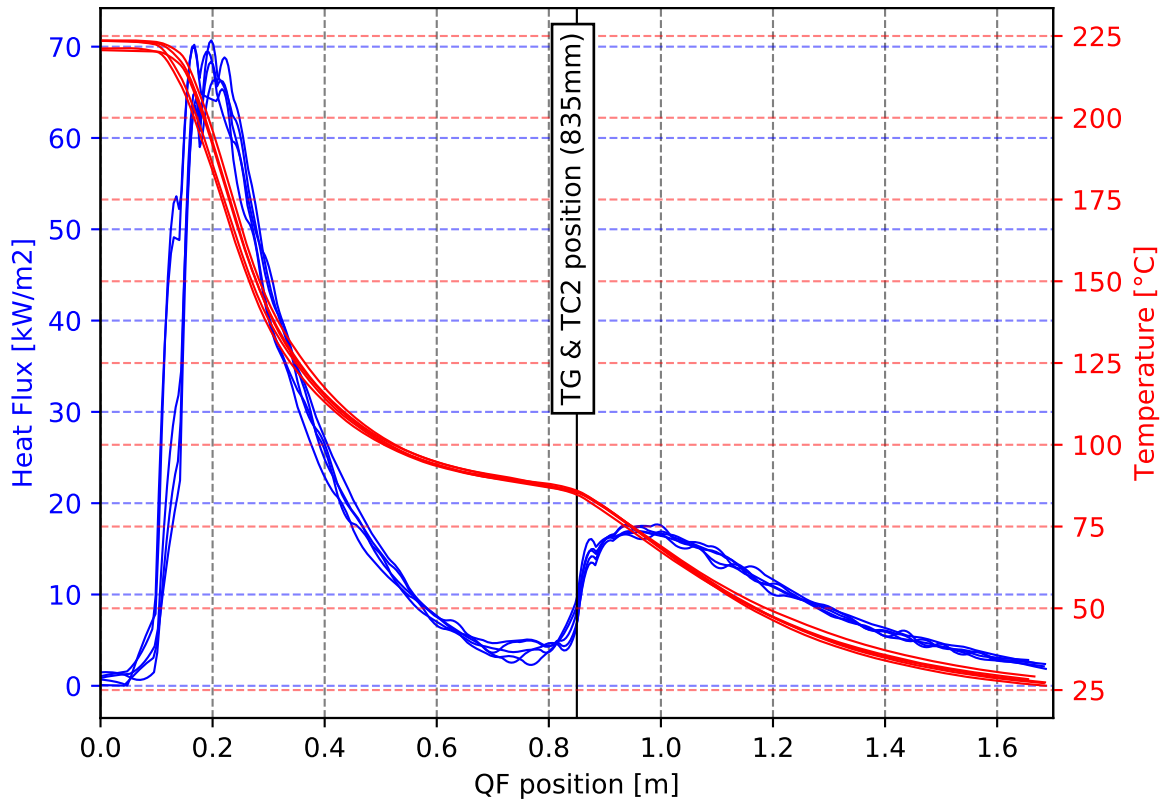
Figure 9.12: Heat flux and temperature of the silica glass tube ($T_0 = 600\,°C$)

The resulting heat flux for given initial wall temperature condition can be seen in Figure 9.12. It is a typical heat flux profile. A high heat flux peak, right behind the flooding start, is obvious at first glance. The peak is more visible at higher temperatures of the test section and it is caused by intensive steam generation when water meets the hot surface. After this initial steam shock, the quench front velocity is stabilized at a

lower value and the steam generation ceases. The temperature of the glass surface is almost constant when quench front reaches the position of the second thermocouple and position of the glass surface measuring one. The value is approximately $85\,^{\circ}C$ on the outer surface. On the inner surface there is a saturated two-phase mixture, so the temperature difference through the glass barrier is approximately $15\,^{\circ}C$. However, the heat flux at this point is very small compared to the heat flux of the heated tube for the same conditions in Figure 9.11.

9.7.3   Internal Heat Source

Internal heat source $P_e\,[MW.m^{-3}]$ is generated by electric current flowing through the heated wall. At the beginning of the experiment at each initial wall temperature level, the generated heat is equal to heat losses. This means that initial heat source value is a function of initial wall temperature.

The solution for the dependence of internal heat source on initial wall temperature is in Equation 9.31 below. The equation essentially includes heat losses to the environment (free convection and radiation), the temperature dependence of electric resistance, etc. For this reason, the dependence was created as an exponential function of the internal heat source (which is measured) and initial wall temperature.

$$P_{e0AB} = (25.25\mathrm{e}{-}5) \cdot T_0^2 - 0.14 \cdot T_0 + 27 \qquad [MW.m^{-3}] \tag{9.31}$$

Figure 9.13 show the dependence for model A and model B. The difference between these two models is insignificant and sensitivity of Equation 10.1 on power source is relatively low, so these two models share the same equation for internal heat source which is the product of these two plots.
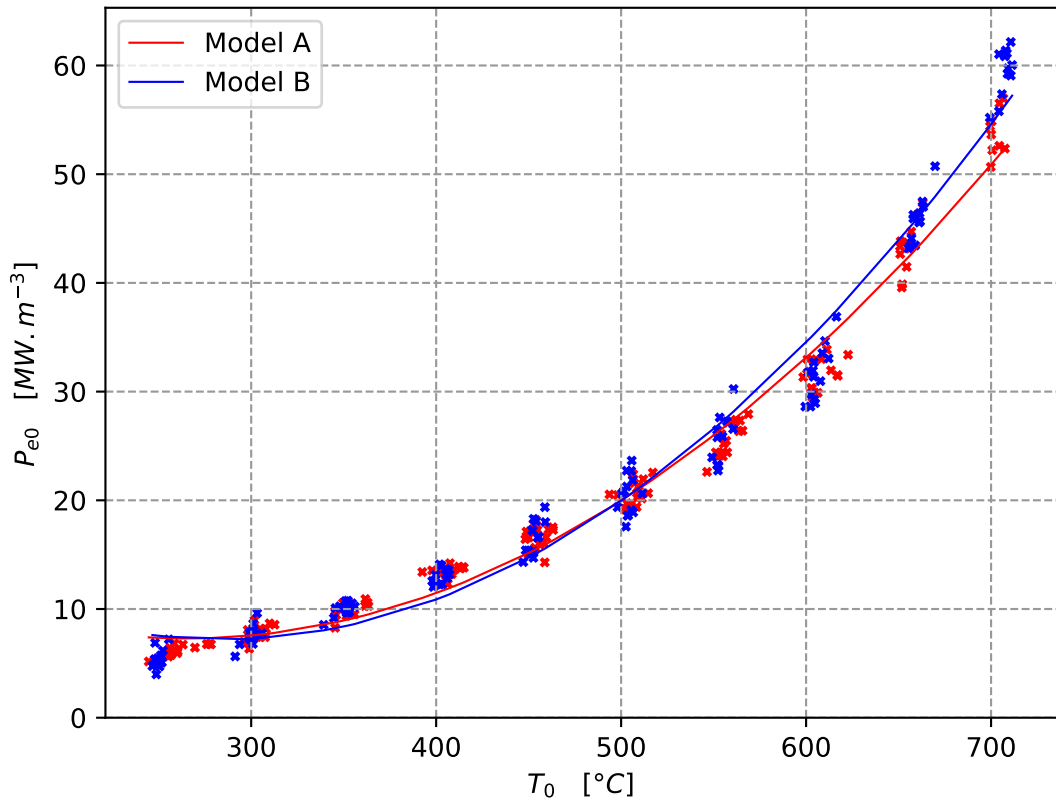
Figure 9.13: Generated heat on initial wall temperature for models A and B

The situation is totally different from models with constant wall thickness, where the initial wall temperature and thus internal heat source remains constant along the heated length. In the case of model C, a dependence on axial position must be incorporated into the solution because initial wall temperature was set for the third thermocouple TC3. The solution for model C was found as a product of initial wall temperature and axial position in the form:

$$P_{e0C} = (6.1\mathrm{e}{-}11)A^2 + (4.6\mathrm{e}{-}5)A + 2.55 \quad [MW.m^{-3}]; \qquad A = T_{0TC3}^{2.07} z^{0.43} \qquad (9.32)$$

where $z\,[m]$ is the axial position and $T_{0TC3}\,[°C]$ is the initial wall temperature of the TC3. Figure 9.15 shows the correlated data for model C.

Figure 9.14: Generated heat on initial wall temperature for model C
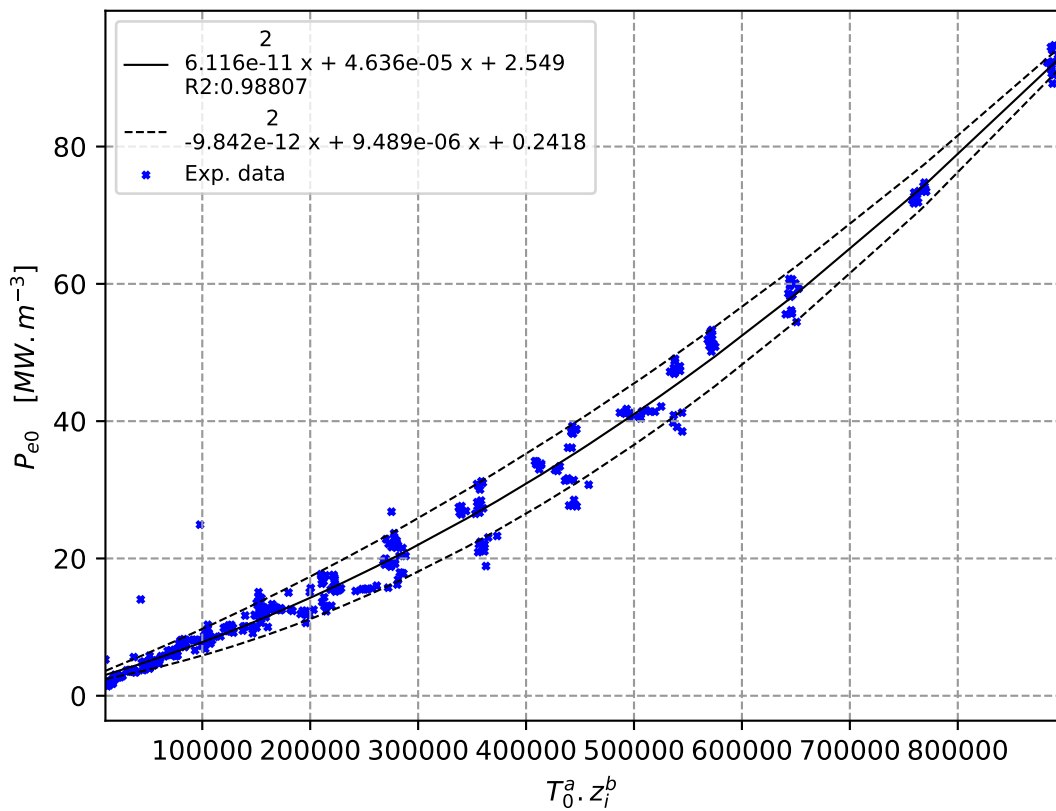
Figure 9.15: Correlated heat source data for model C

9.7.4 Initial Wall Temperatures of Model C

Hand in hand with different internal heat source power along model C goes different initial wall temperature for each thermocouple. As Equation 10.1 needs as i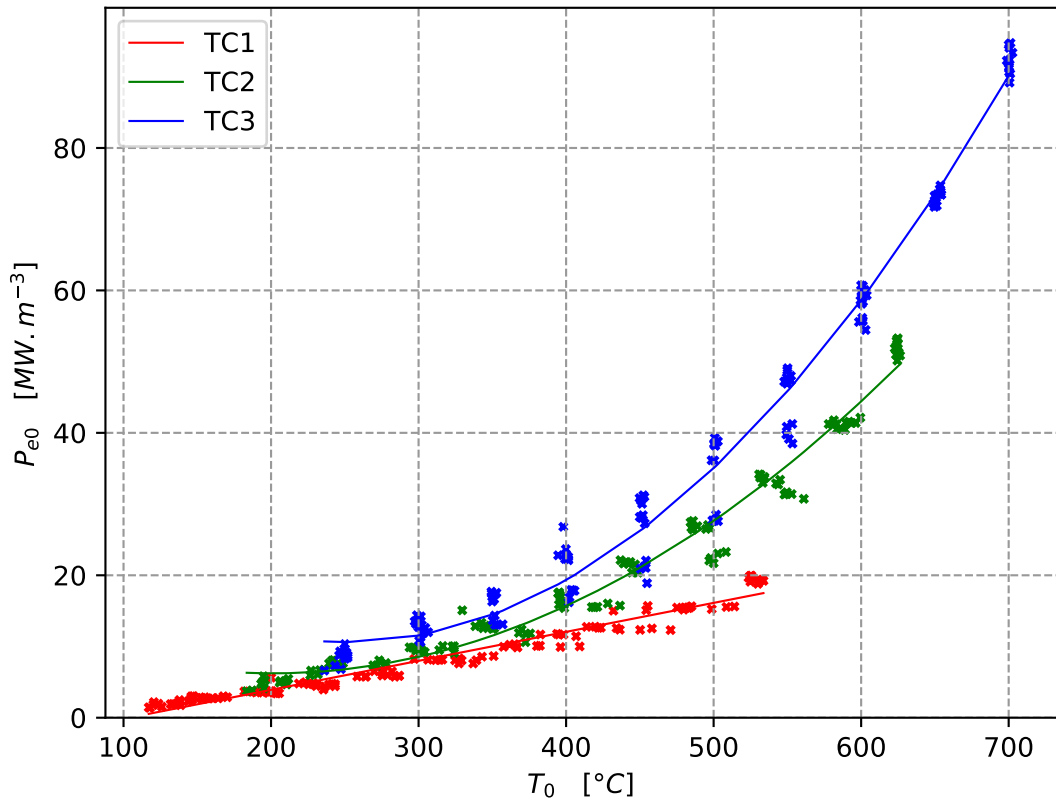nput initial wall temperature and consequently Equation 10.13 requires averaged quenching temperature, knowledge of initial wall temperature for TC1 and TC2 for model C is necessary. The initial wall temperature is set for TC3 for this model. Thus other two temperatures must be taken from experimental data directly or it can be calculated through functions of initial wall temperature of TC3. The dependence of the first two thermocouples on the last one in initial wall temperature is shown in Figure 9.16.

Figure 9.16: TC1 and TC2 initial temperatures on TC3 initial temperature

$$T_{0TC1} = (9.24e-4) \cdot T_{0TC3}^2 + 0.042 \cdot T_{0TC3} + 55 \qquad [^\circ C] \qquad (9.33)$$

$$T_{0TC2} = 0.974 \cdot T_{0TC3} - 50 \qquad [^\circ C] \qquad (9.34)$$

Equations 9.33 and 9.34 correspond to Figure 9.16 and its purpose is to evaluate initial wall temperature along model C in further calculations without need of unnecessary

experimental data inputs.

9.8   Heat Transfer Coefficients

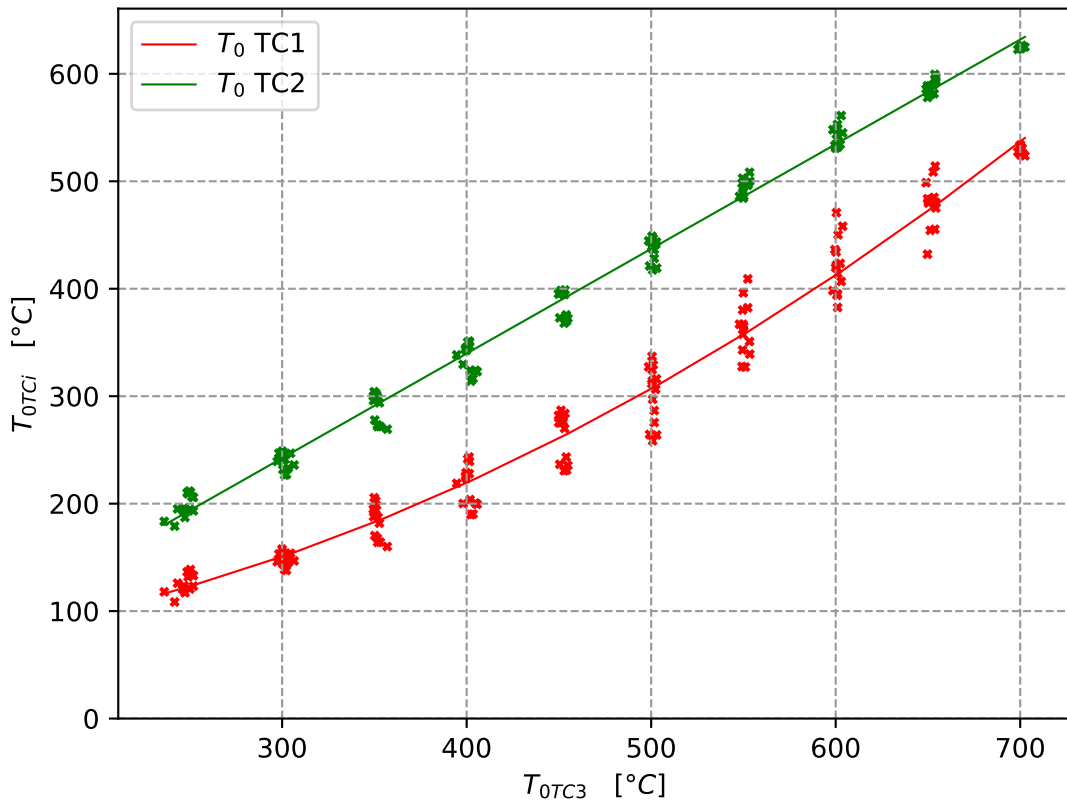Calculation of heat transfer coefficient is one of the most tricky part of quenching data evaluation and thus it is very rare in experimental works in the field. When we have calculated areal heat flux into coolant the only thing it needs to be calculated is the coolant temperature. Any direct measuring of temperature in the flow is impossible due to the small area for thermocouple installation and due to the undesirable influence of the thermocouple on the quenching process. The thermocouple within the coolant flow will be cooled down significantly earlier and it generates secondary quench fronts spreading further along the geometry.

9.8.1   Downstream Heat Transfer Coefficient

Common approach, that can be found in several studies [82], is assumption of saturated steam downstream the quench front i.e. $T_{cool} = 100\,°C$. At high initial wall temperatures, this assumption will be less accurate. In this case, overheated steam will be present in the channel. However the overheating can be assumed to be relatively small and thus negligible. The saturated steam approach is adopted in this section for the dry region. The main reason is a too difficult prediction of the steam velocity in the channel due to the unknown exact evaporated mass of water. Based on the heat transfer version of Newton's law of cooling, the heat transfer coefficient can be obtained as:

$$h_{sat} = \frac{Q_c}{\Delta T_{sat}} = \frac{Q_c}{T_w - T_{sat}} \qquad [W.m^{-2}.K^{-1}] \qquad (9.35)$$

where $Q_c\,[W.m^{-2}]$ is heat removed by water (Equation 9.27, p. 100), $T_w\,[°C]$ is wall temperature and $T_{sat}\,[°C]$ is saturation temperature of water at atmospheric pressure ($T_{sat} = 100\,[°C]$). This equation was involved in this study up to nucleate boiling point declared in Section 9.4 on page 89. Behind this point a complex prediction of coolant temperature was developed.

9.8.2 Upstream Coolant Temperature

The only way how to obtain coolant temperature behind the quench front is to calculate enthalpy increase caused by known areal heat flux behind the front in combination with measured inlet coolant temperature. Because the heat flux behind the front is relatively low, the temperature increase of water is also insignificant except the region right behind the front.

The coolant temperature calculation is based on the idea, that heat flux from the surface to water is very similar along the geometry, or it morphs linearly in the case of varying wall thickness. In other words, moving along heat flux profile forward in time means to go backward in space, because the investigated point is deeper and deeper below the advancing front. In the case of areas without thermocouples, the linear morphing of heat flux profiles is applied. The concept of moving and morphing heat flux profile is shown in Figure 9.17. The effect of spacers is neglected in this approach. It can be expected, that preheated water accumulated around a spacer may increase the actual water temperature compared to calculated one because it is probably not too deep under the saturation temperature. Nevertheless, it can be supposed, when the quench front reaches next thermocouple the preheated portion of water will be already evaporated and fresh water will be fed to the front.
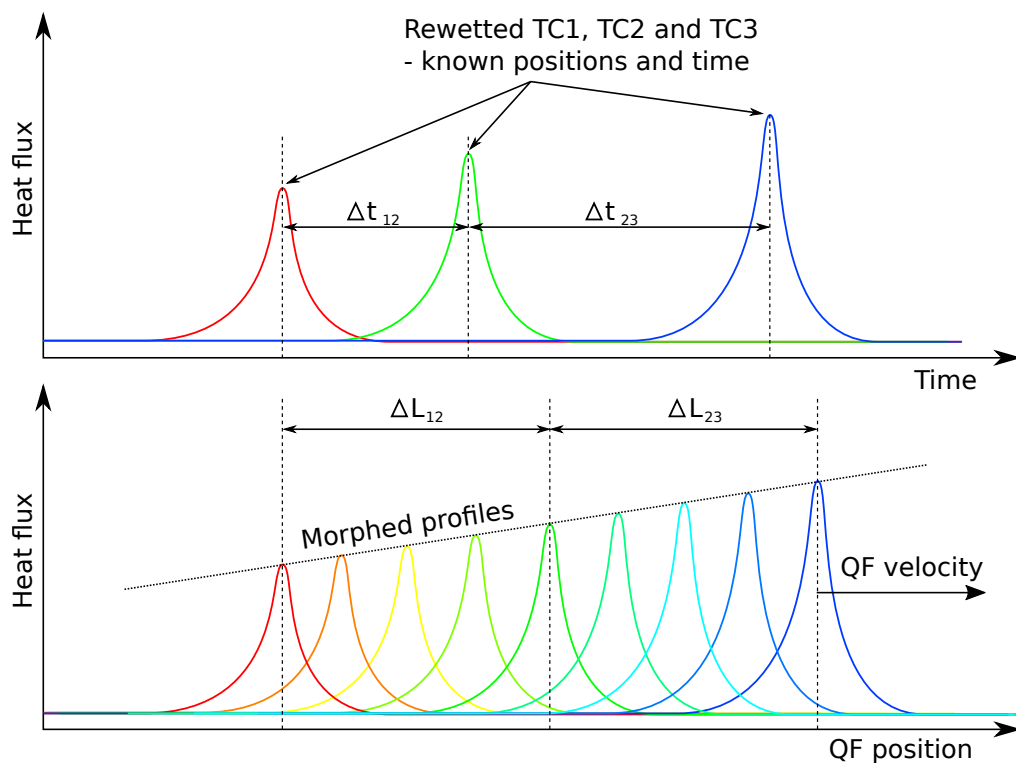
Figure 9.17: Heat fluxes along the geometry of model C

The water velocity at the inlet is the same along the channel (in the rewetted region) at given time. A time interval needed to overcome the distance between thermocouples can be calculated from the known velocity of the water at a given time for given thermocouple. The heat flux profiles at this thermocouple and the previous one give us information about how many heat the coolant had to remove from the tube during its path. We can go further back in time/space on heat flux curves if another thermocouple is below these two. In this case, the process is repeated between second and third thermocouple behind the investigated one starting at end time from the previous step and so on. For better accuracy, the water velocity and inlet enthalpy should be taken at corresponding times during the calculation. The solution process is described below.

Figure 9.18: Cascade concept of coolant temperature calculation

The following description of "cascade" calculation process is for the last thermocouple. Remaining thermocouples are calculated in the same way just with the reduced number of cascade steps. A graphical representation is shown in Figure 9.18 and it is followed by process description.

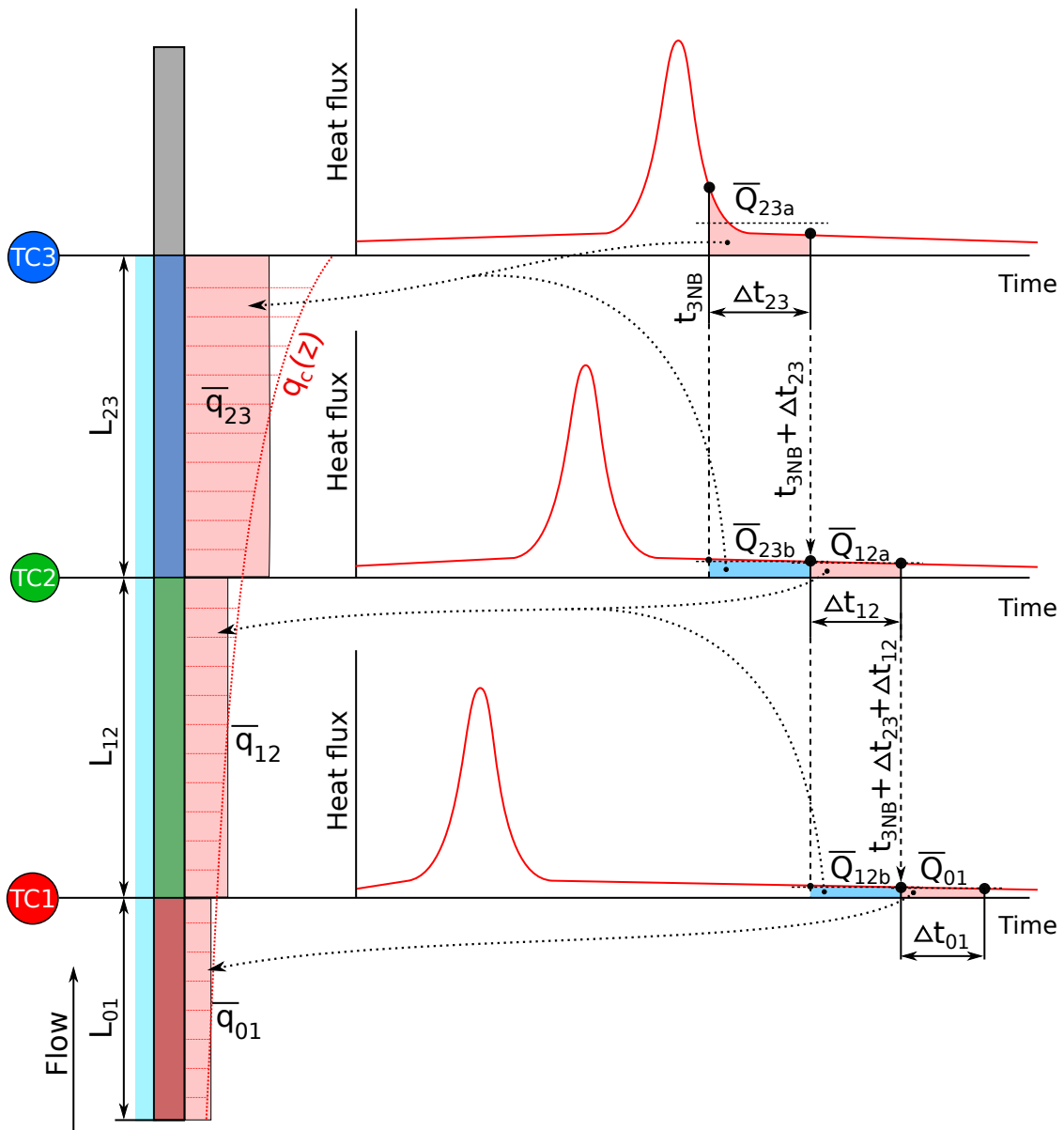- Enthaply increase between thermocouple TC2 and TC3:

  - Interval needed for water to overcome the distance between thermocouples is determined by the pitch ($L_{23} = 0.5\,m$) and inlet velocity at time point of nucleate boiling temperature of the third thermocouple (t_{3NB}):

$$\Delta t_{23} = \frac{L_{23}}{c_{t_{3NB}}} = \frac{0.5 \cdot \rho_{t_{3NB}}}{G_{t_{3NB}}} \qquad [s] \qquad (9.36)$$

  - Time when the investigated water portion passed the second thermocouple then was:

$$t_2 = t_{3NB} - \Delta t_{23} \qquad [s] \qquad (9.37)$$

  - Mean heat power between thermocouples TC2 and TC3 was then calculated as integral part of heat flux curve in resulting time interval Δt_{23} (Heat flux $Q_i(t)\,[W.m^{-2}]$ was calculated using Equation 9.27, p.100):

$$\overline{q_{23}} = \frac{\overline{q_{23a}} + \overline{q_{23b}}}{2} = \frac{\int_{t_{3NB}}^{t_2} Q_3(t)dt + \int_{t_{3NB}}^{t_2} Q_2(t)dt}{2\Delta t_{23}}\pi dL_{23} \qquad [W] \qquad (9.38)$$

  - Enthalpy increase is then:

$$\Delta H_{23} = \frac{\overline{q_{23}}}{\overline{G_{23}}A_f} \qquad [J.kg^{-1}] \qquad (9.39)$$

  where $\overline{G_{23}}$ is averaged mass flux within given time interval.

$$\overline{G_{23}} = \frac{\int_{t_{3NB}}^{t_2} G(t)dt}{\Delta t_{23}} \qquad [kg.m^{-2}.s^{-1}] \qquad (9.40)$$

- Enthalpy increase between thermocouple TC1 and TC2:

  The calculation process is analogical to the interval between TC2 and TC3

  - Time interval:

$$\Delta t_{12} = \frac{L_{12}}{c_{t_2}} = \frac{0.5 \cdot \rho_{t_2}}{G_{t_2}} \qquad [s] \qquad (9.41)$$

  - Time of passing the first thermocouple:

$$t_1 = t_{3NB} - \Delta t_{23} - \Delta t_{12} = t_2 - \Delta t_{12} \qquad [s] \qquad (9.42)$$

– Mean according power within the region:

$$\overline{q_{12}} = \frac{\overline{q_{12a}} + \overline{q_{12b}}}{2} = \frac{\int_{t_2}^{t_1} Q_2(t)dt + \int_{t_2}^{t_1} Q_1(t)dt}{2\Delta t_{12}} \pi d L_{12} \qquad [W] \tag{9.43}$$

– Enthalpy increase:

$$\Delta H_{12} = \frac{\overline{q_{12}}}{\overline{G_{12}} A_f} \qquad [J.kg^{-1}] \tag{9.44}$$

where $\overline{G_{12}}$ is averaged mass flux within the time interval 1-2.

$$\overline{G_{12}} = \frac{\int_{t_2}^{t_1} G(t)dt}{\Delta t_{12}} \qquad [kg.m^{-2}.s^{-1}] \tag{9.45}$$

• Enthalpy increase between bottom edge of the heated tube and the first thermocouple.

In this case the mean power along the region can not be weighted between two known fluxes, so the power results only from data of TC1. Neverthless, heat flux is very low, and practically constant in time.

– Time interval

$$\Delta t_{01} = \frac{L_{01}}{c_{t_1}} = \frac{0.335 \cdot \rho_{t_1}}{G_{t_2}} \qquad [s] \tag{9.46}$$

– Time of passing the heated edge ($z = 0$):

$$t_0 = t_{3NB} - \Delta t_{23} - \Delta t_{12} - \Delta t_{01} = t_1 - \Delta t_{01} \qquad [s] \tag{9.47}$$

– Mean power within the region:

$$\overline{q_{01}} = \frac{\int_{t_2}^{t_1} Q_1(t)dt}{\Delta t_{01}} \pi d L_{01} \qquad [W] \tag{9.48}$$

– Enthalpy increase:

$$\Delta H_{01} = \frac{\overline{q_{01}}}{\overline{G_{01}} A_f} \qquad [J.kg^{-1}] \tag{9.49}$$

where $\overline{G_{01}}$ is averaged mass flux within the time interval 0-1.

$$\overline{G_{01}} = \frac{\int_{t_2}^{t_1} G(t)dt}{\Delta t_{01}} \qquad [kg.m^{-2}.s^{-1}] \tag{9.50}$$

• Resulting enthalpy of water at given time and thermocouple (in this case TC3):

$$H3 = H_{in_{t0}} + \Delta H_{01} + \Delta H_{12} + \Delta H_{23} \qquad [J.kg^{-1}] \tag{9.51}$$

Temperature of water was subsequently calculated using iapws steam tables:

$$T_{cool_3} = f(H3, p = 0.1MPa) \qquad [^\circ C] \tag{9.52}$$

This process was iterated for all time points in interpolated data arrays (beyond the nucleate boiling point) and for every thermocouple. The result is three sets of coolant temperatures giving a coolant temperature for each thermocouple during the reflood phase of the experiment. Temperature profiles of wall temperatures and coolant temperatures are shown in Figure 9.19. Using these temperature profiles and law of cooling (Equation 9.53), a map of heat transfer coefficients was created.

$$h = \frac{Q_{ci}}{\Delta T_{cooli}} = \frac{Q_{ci}}{T_{wi} - T_{cooli}} \qquad [W.m^{-2}.K^{-1}] \tag{9.53}$$
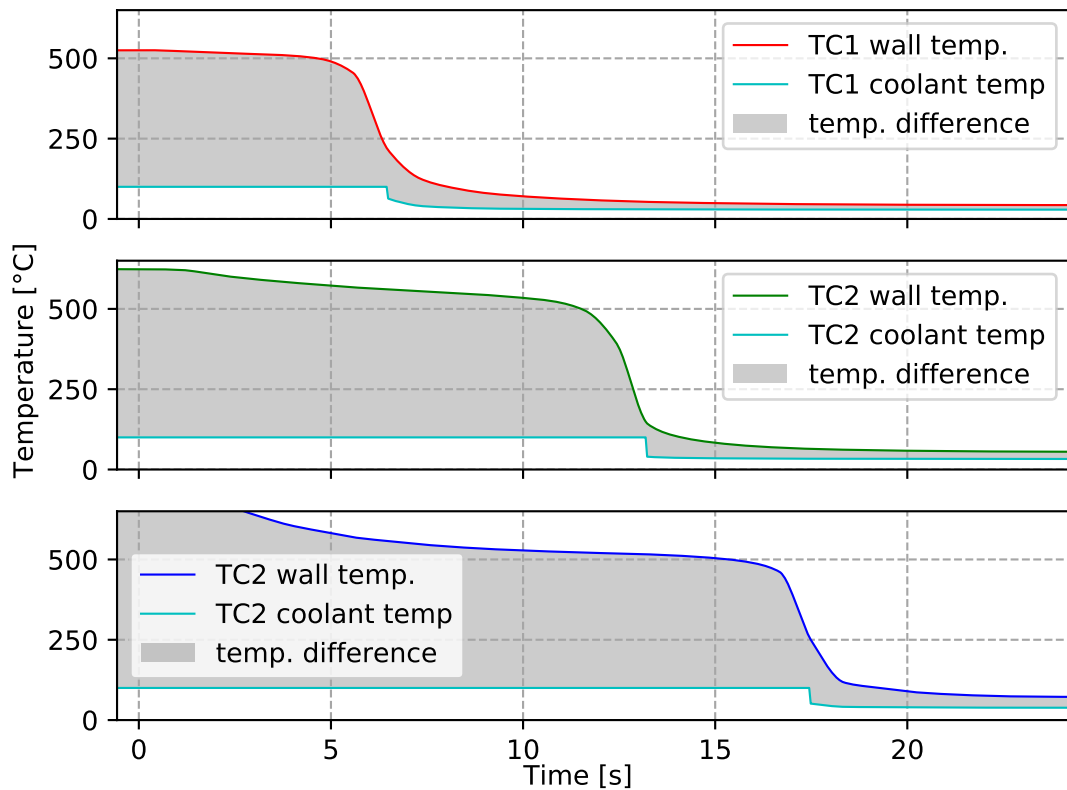
Figure 9.19: Result of coolant temperatures ($T_0 = 600\,°C$, Model B)
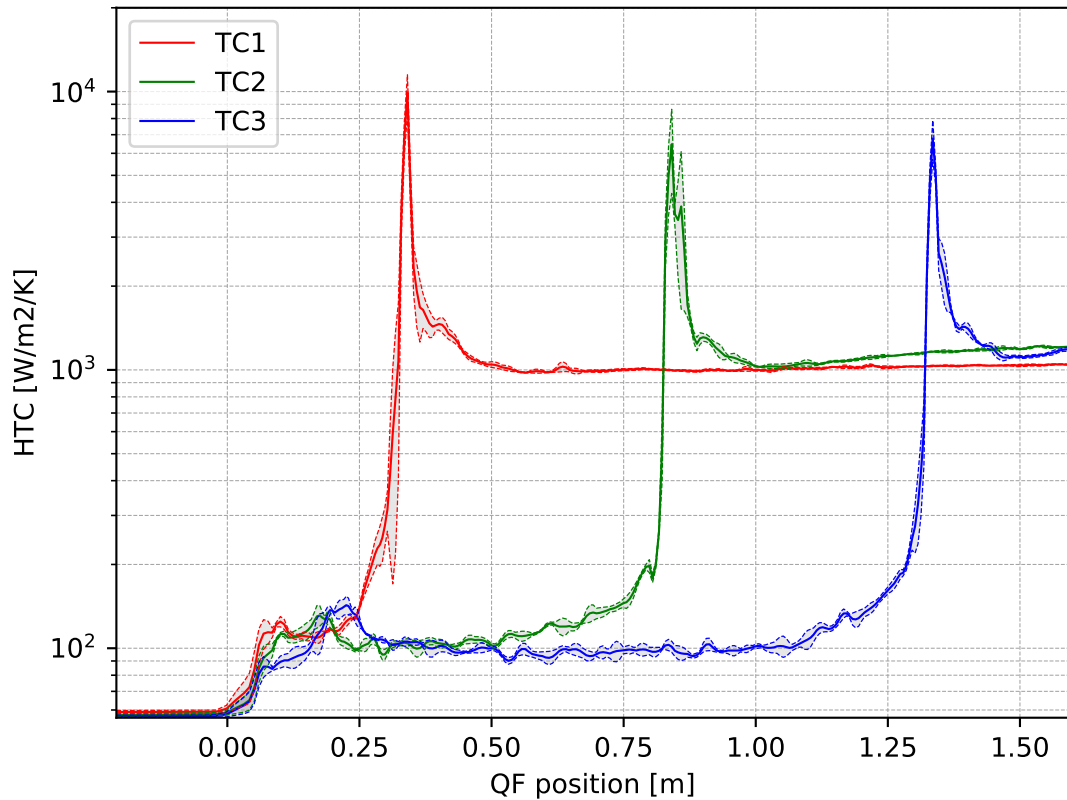
Figure 9.20: Map of HTC vs front position ($T_0 = 600\,^\circ C$, Model B)

9.9 Conclusion

Main parts of individual data processing procedure were described in this chapter. This process begins with experimental data extraction, their interpolation and eventually filtration. Prepared data serve as an input for other steps, such as important temperature points detection, calculation of heat transfer coefficients, etc. The heat transfer coefficient is the most tricky part of the process. The heat transfer coefficients in the dry and two-phase region are assumed as regions cooled by steam or water-steam mixture at saturation temperature, heat transfer coefficients behind the quench front are calculated through coolant temperature obtained via cascade algorithm. Generally, the individual data processing part of the study is crucial and the most complex part. Its purpose is to obtain all relevant information from experimental data and prepare them for further evaluation.

Chapter 10

Results

This chapter consists of all relevant results from individual data processing coupled in global view on the process for given experimental equipment. These results include a view of important temperatures such as quenching temperature, critical heat flux temperature and nucleate boiling temperature. These temperatures are used in other results as input variables and they are also used as limits for the developed three-regional model of rewetting. Hand in hand with the defined important wall temperatures go relevant heat transfer coefficients (HTC) in local form or in mean for between mentioned temperature limits for usage on the three-regional model. The most important result presented in this chapter is a solution for mean quenching velocity. The understanding of the complexity of the process and its influence on quenching velocity is crucial for a deeper understanding of the process and for more effective handling of situations where quenching takes place. On top of that, there are presented results of pressure behavior during quenching and its influence on the process.

10.1 Pressures

Relative pressure was measured by pressure sensor described in section 6.3.4 on page 73. Relative pressures of the cold section for selected flow rate levels were also measured. The pressure was measured as a supplementary parameter with focus on pressure peaks at the beginning of the reflood process.

10.1.1 Pressure Peaks

The reflood process goes with significant pressure peaks while the coolant meets the hot surface. This sudden contact generates an enormous amount of vapor due to the momentum of the coolant. The effect is clearly detectable at initial wall temperature levels above $400\,^{\circ}C$. This effect was already published and described by Stepanek (2016) [A3] for model A. In this study, the pressure peak rate is described also for models B and C.

The pressure peaks significantly influence pressure drop at the beginning of the reflood process and its value can easily exceed total pressure drop of fully reflooded test section as shows Figure 10.1. This can be a challenge for parallel channels, e.g. nuclear reactor core. The unevenness can lead to cooling water flowing around the central area of the core, where the surface temperature is lower, and the central area of the core can be cooled down distinctly later.

Figure 10.1 shows measured pressures for model B and for all four flow rate levels. The pressure peak is clearly visible from these plots. Its value is dependent on flow rate as well as on initial wall temperature. The flow rate is responsible for higher momentum and initial wall temperature represents more accumulated heat. In combination, these two parameters can raise considerable pressure drop as it is shown in Figure 10.1 d).
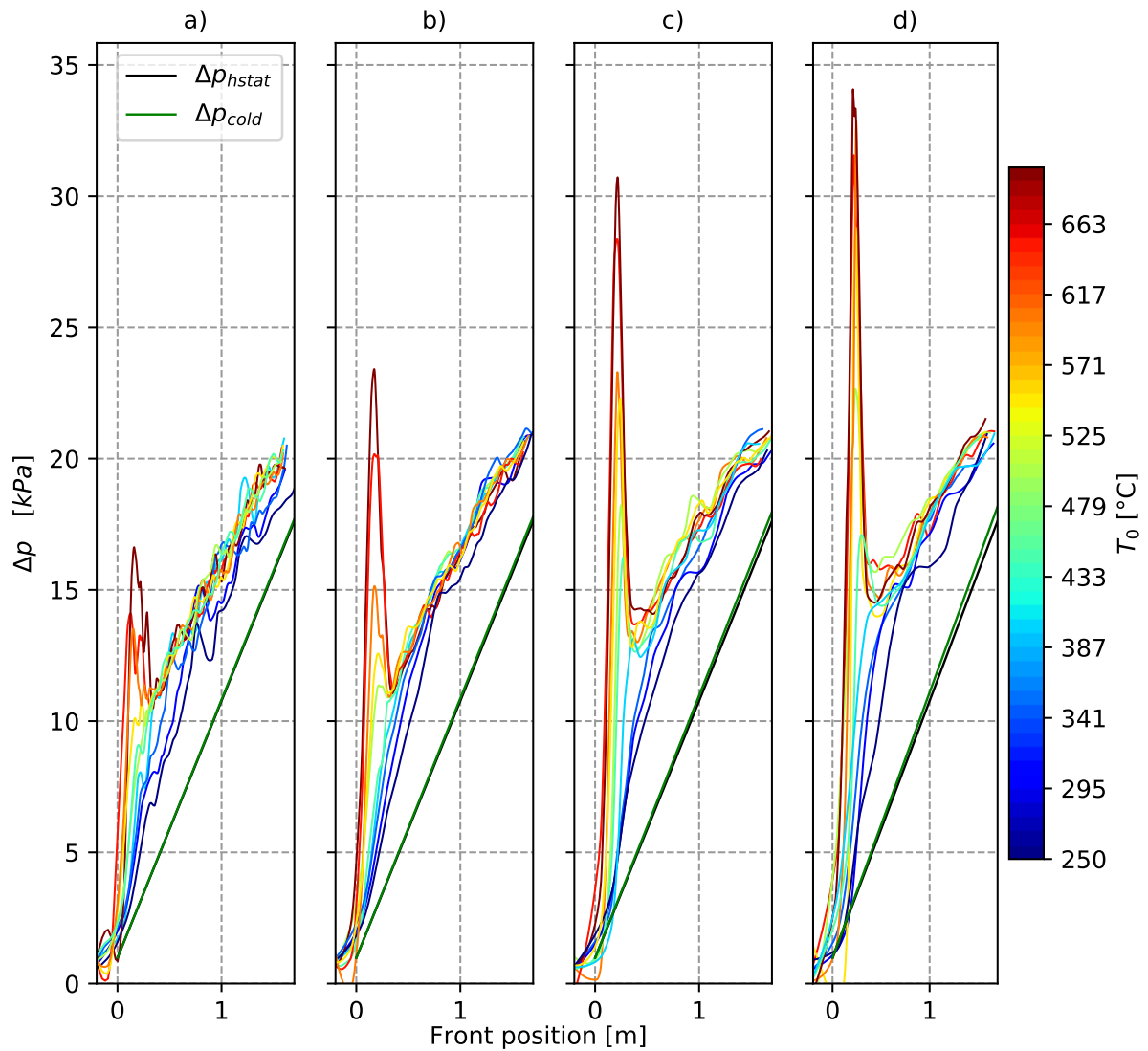
Figure 10.1: Relative pressures of model B

a) $G = 80\,kg.m^{-2}.s^{-1}$, b) $G = 110\,kg.m^{-2}.s^{-1}$, c) $G = 190\,kg.m^{-2}.s^{-1}$, d) $G = 270\,kg.m^{-2}.s^{-1}$

Figure 10.1 also contains hydrostatic pressure and pressure drop of the cold test section. The difference between cold section pressure drop and hydrostatic pressure is hardly noticeable compared to dynamic pressure drop during the reflood process. Based on the figure it can be deducted, that addition to pressure drop by dynamic behavior within the channel is approximately $5\,kPa$ to $7\,kPa$.

Figure 10.3: Pressure peaks of model A
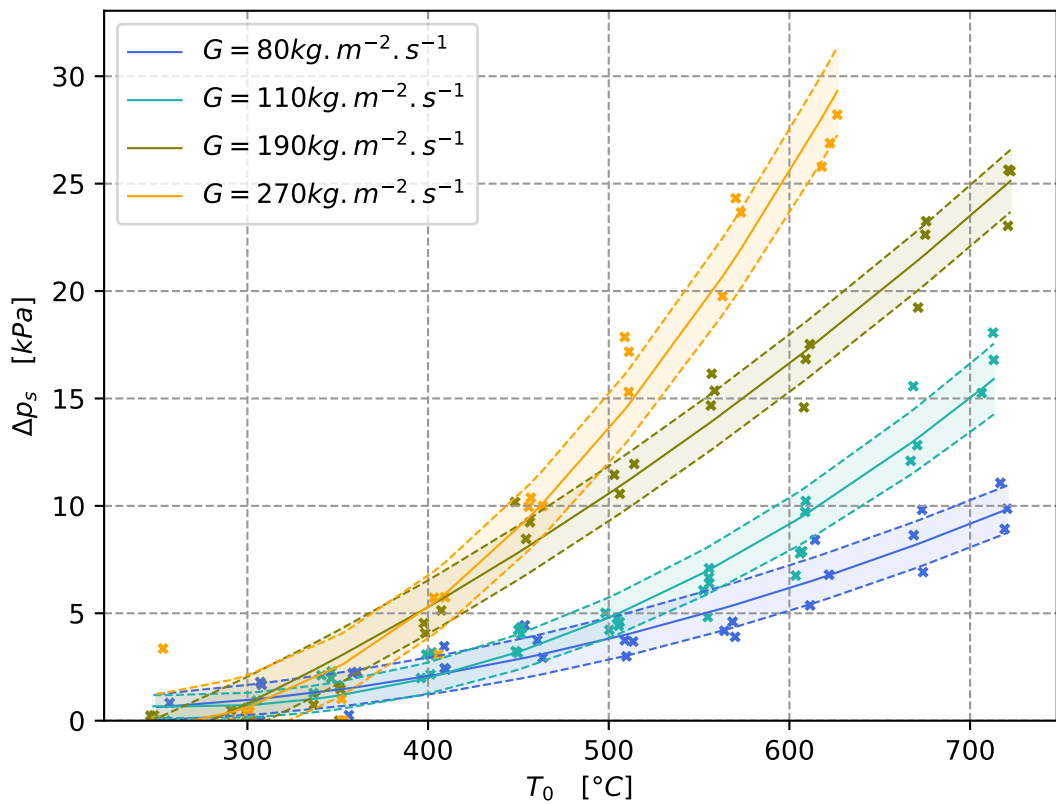
Figure 10.4: Pressure peaks of model B
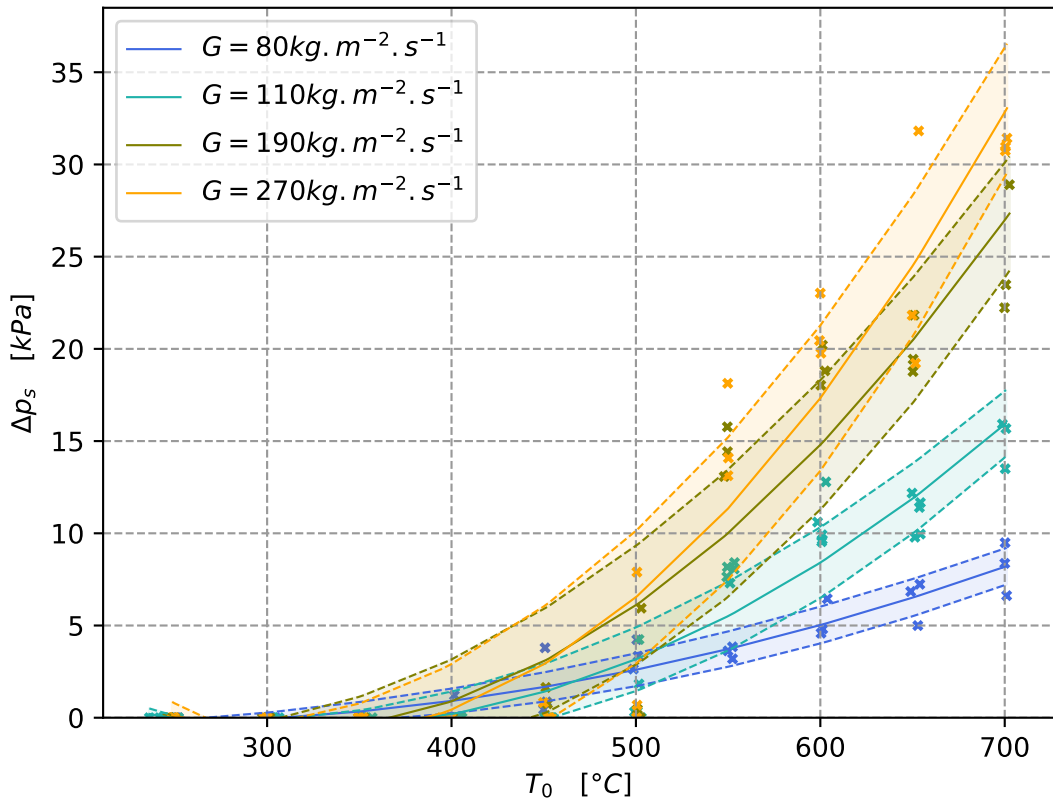
Figure 10.5: Pressure peaks of model C

The pressure peaks were detected in measured pressures as maximum pressure before rewetting of TC1 minus according to the pressure drop of the cold section (approximately $7\,kPa$). Figures 10.3, 10.4 and 10.5 show values of pressure peaks on initial wall temperature and for different flow rates. Detection of actual pressu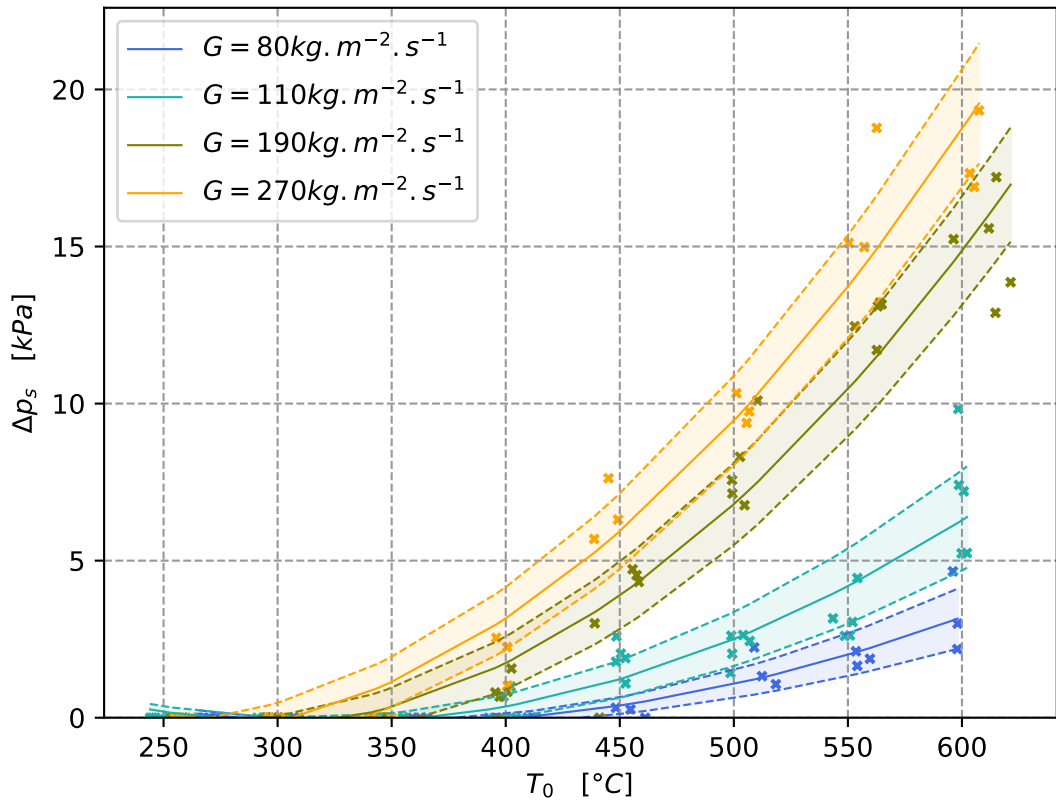re peak at high flow rates proved to be difficult because the actual peak can be uncaught by data acquisition system due to a short time interval of its occurrence. For this reason, some data were excluded in following figures.

- In the case of model A, pressure peaks begin to be significant at the initial wall temperature of $400\,°C+$ and they rise exponentially with the wall temperature.

- Model B shows similar initial wall temperature for the beginning of pressure peaks, but compared to model A the value of pressure peak is almost twice. This is caused by more accumulated heat within the wall, which generates more vapor and pressure peak consequently.

- Initial wall temperature for model C is shifted to higher temperatures, approximately $450\,°C+$ (initial temperature of TC3). This shift is caused by relatively cold

bottom part of test section due to profiled heat generation. The values are also more scattered for the same reason.

These pressure transient processes strongly influence the pre-cooling of the geometry and the quenching temperature consequently. This effect was mentioned in section 10.2.1.1 (page 120) and it is already included in Equation 10.1. As it can be seen, the pressure characteristics of the flooding are complex problem closely connected with flooding geometry and channel design.

10.2   Temperatures

Surface temperatures are the most important measured parameters. A lot of assumption can be made on the basis of their time courses. There are several important points on these profiles, namely: quenching temperature, critical heat flux temperature and temperature of the nucleate boiling point. These points separate important areas with different flow and heat transfer regimes. For the presented study the quenching temperature showed to be sufficient for description of the investigated process.

10.2.1   Quenching Temperature

Quenching temperatures have been found via second order derivatives on the time-dependent temperature data. The quenching temperature represents a state at which re-establishment of solid-liquid contact is possible. After this point a high heat transfer rate takes place and thus the quenching temperature determination is the crucial part of the study. From this point of view, a higher quenching temperature (relative to initial one) means, that less accumulated heat needs to be removed in front of the quench front and thus the front can move faster along the surface.
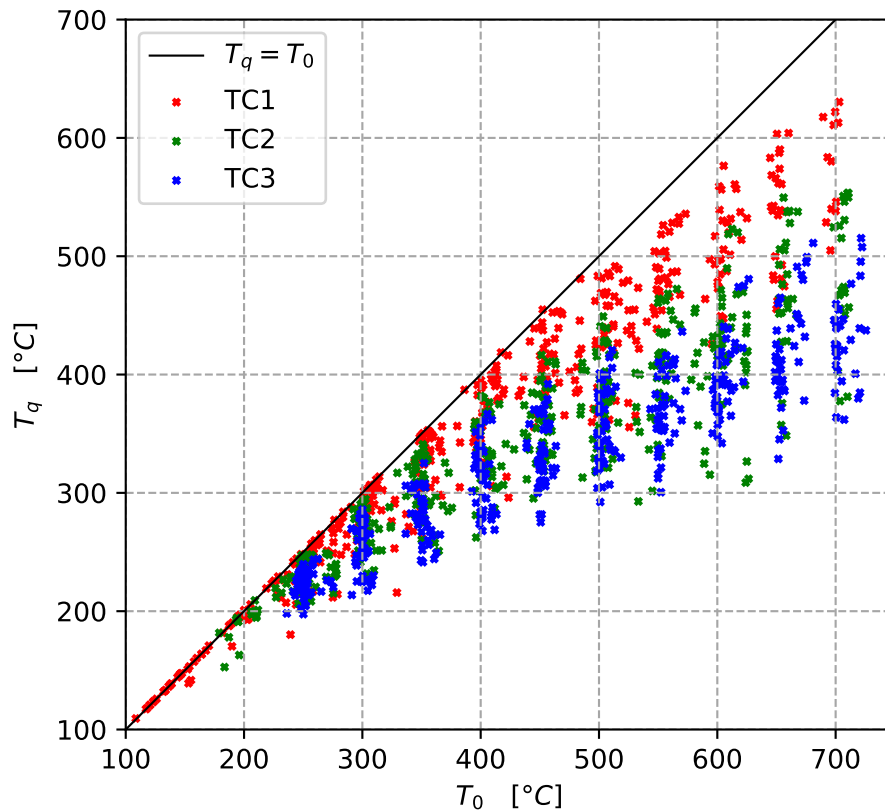
Figure 10.6: Quenching temperatures for all models and flow rates

All quenching temperature points are shown in Figure 10.6. Based just on this scatter plot, it can be concluded (regardless of flow rate), that with rising initial wall temperature the quenching temperatures are more deflected from the line, which represents the state where quenching temperature equals the initial wall temperature. Another insight is, that the deflection rate is also dependent on thermocouple's position which is obvious at first glance. It can be caused by more pre-cooling time further from the inlet. Points bellow temperature of $T_0 = 200\,°C$ represent states for the model C, where no boiling at the advancing water surface was visible. In this case, the surface was rewetted instantly.

This is another lack of approach, which determines quenching temperature via the first-order derivative. The temperature of the maximum first order derivative will be never equal to the initial temperature, even in the case of very low initial parameters. In this case, the temperature will be located somewhere on the most inclined part of the temperature profile, regardless of whether the surface is already rewetted.

10.2.1.1 Precooling Effect on Quenching Temperature

The difference in geometry precooling is clearly visible on models with different wall thickness and high initial wall temperatures. There are plotted two temperature profiles

in Figure 10.7 for models A ($\delta = 0.5\,mm$) and B ($\delta = 1.0\,mm$).
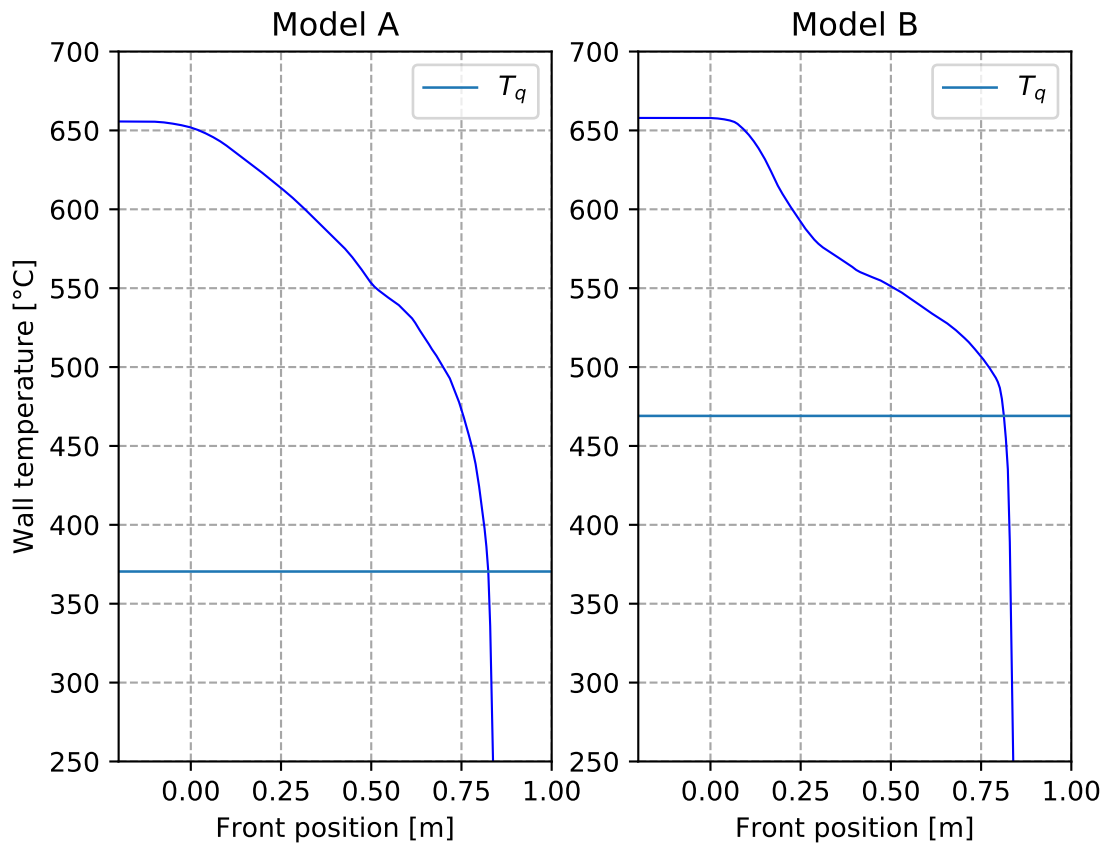
Figure 10.7: Precooling at TC2 on models A and B ($T_0 = 650\,°C$)

It can be seen from temperature profiles in Figure 10.7, that wall thickness has a significant influence on precooling of the foregoing parts of geometry. The reason for this is, that more accumulated heat within the thicker wall is responsible for greater pressure peak, while coolant reaches heated part of the tube or part, where the wall temperature is high enough to produce a significant amount of vapor (case of model C). The sudden contact of water with hot wall produces an enormous amount of vapor due to coolant momentum. The vapor production is almost constant or slightly decreases after this initial peak. In the case of model B, the precooling by vapor "explosion" is high enough to set up nearly new initial conditions from wall temperature point of view. However, the actual quenching temperature is a product of combinations all relevant variables and conditions.

10.2.1.2   Limit Temperature - True Rewetting Temperature
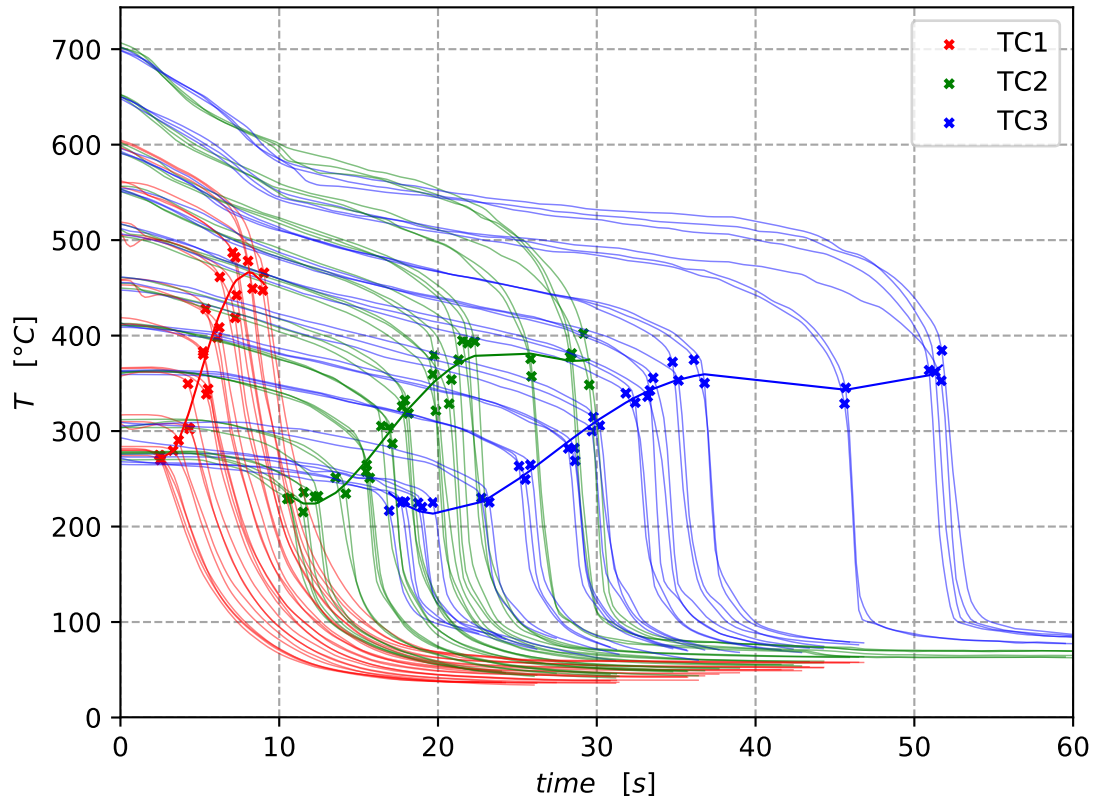
Figure 10.8: Temperature profiles of model A at $G = 80\,kgm^{-2}s^{-1}$

Another finding supporting the second order derivative approach is situation showed in Figure 10.8. It shows typical temperature profiles through all initial wall temperatures for model A with marked quenching temperatures. An existence of limit quenching temperature can be clearly seen from the figure. This is typical behavior of quenching temperatures at low flow rates and high initial wall temperatures. It fully supports the idea of rewetting temperature in its true form. It can be concluded, that this temperature limit is the true rewetting temperature because above this temperature the surface cannot be rewetted and the flooding process is prolonged until wall temperature falls below this limit. Otherwise, the "quenching" temperature below the limit is not the temperature of stable vapor film collapse, but a common transient boiling temperature of the wall for actual parameters. Eventually, rewetting/quenching temperature can be split into two temperatures, where the temperature limit will be the rewetting temperature and below the limit, the temperature will be called the quenching temperature. Unfortunately, the present study has not enough data for low flow rates and high initial wall temperatures to fully investigate and correlate the rewetting temperature limits. But it is a promis-

ing topic for future basic research on the rewetting phenomenon and it is supposed in recommendations.

10.2.1.3 Quenching Temperature Correlation

Quenching temperature was checked for dependency on material and global experimental parameters. The dependence on initial global parameters proved to be the reliable way how to correlate experimental data. Variables, which are not investigated e.g. inlet coolant temperature (remains almost constant through all experiments), are not present in correlation from this reason. All variables and its units and correlation results are listed in Table 10.1. Figure 10.9 shows the linear dependency of quenching temperature on resulting combination of initial experiment parameters.
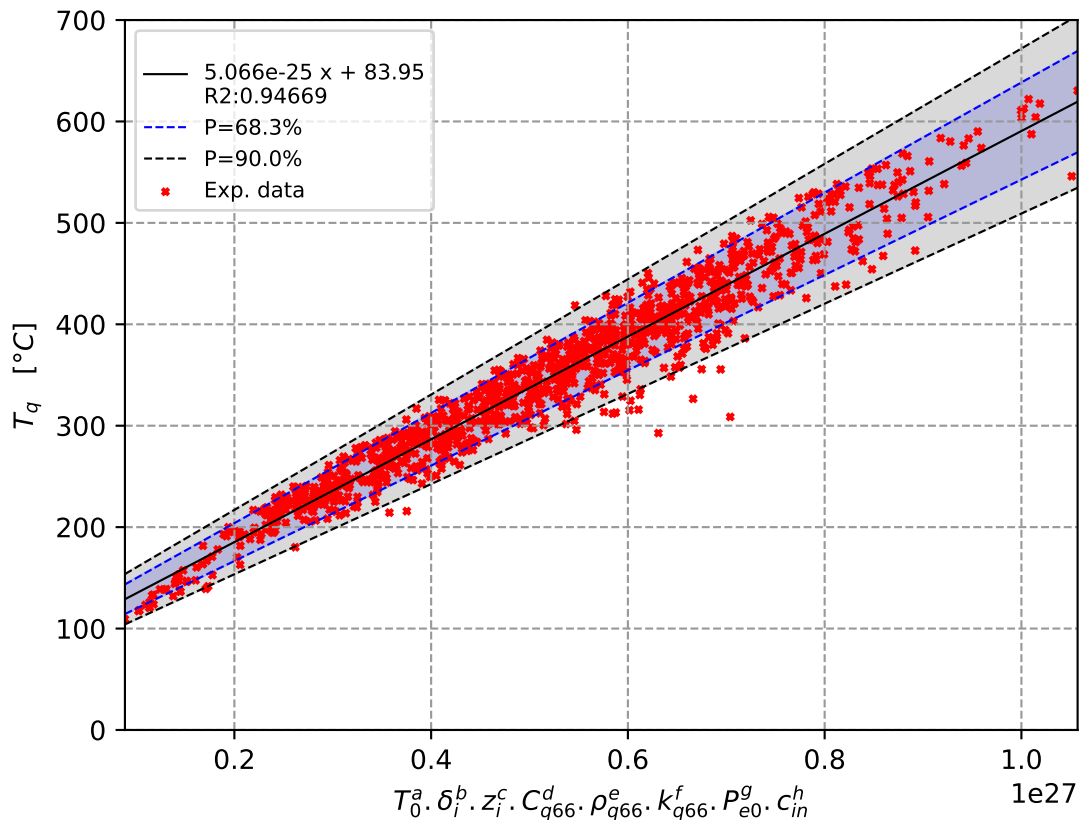

Figure 10.9: Quenching temperature data correlation

Material properties were included in the simplified form as parameters at 66 % of initial wall temperature in order to avoid further temperature iteration and reflect its temperature dependency in reasonable form.

Table 10.1: Exponents of quenching temperature correlation

Variable	Unit	Exponent	Optimized value	Rounded value
T_0	$°C$	a	2.0084324	2.01
δ_i	m	b	-0.14643548	-0.15
z_i	m	c	-0.19332843	-0.19
C_{q66}	$J.kg^{-1}.K^{-1}$	d	-1.73060197	-1.73
ρ_{q66}	$kg.m^{-3}$	e	7.44157239	7.44
k_{q66}	$W.m^{-1}.K^{-1}$	f	-2.48221125	-2.48
P_{e0}	$MW.m^{-3}$	g	-0.02443836	-0.024
c_{in0}	$m.s^{-1}$	h	0.1503645	0.15
Slope			$5.066e-25$	$5.066e-25$
Intercept			83.95	84

Equation 10.1 bellow solves quenching temperature for all measured models, all flow rates and all initial wall temperatures:

$$T_q = T_0^{2.01} \cdot \frac{[(5426e-7)\rho_{q66}]^{7.44}}{C_{q66}^{1.73} k_{q66}^{2.48}} \cdot \frac{c_{in0}^{0.15}}{\delta_i^{0.15} z_i^{0.19} P_{e0i}^{0.024}} + 84 \qquad [°C] \qquad (10.1)$$

where T_0 is the initial wall temperature, c_{in0} is the initial coolant inlet velocity, δ_i is the wall thickness (i is for thermocouple's index), z_i is the position along geometry relative to heated length and P_{e0i} is the initial value of internal heat source (in this study Equation 9.31 is used). Material properties are calculated through Equations 6.8, 6.9, 6.10, 6.11, 6.14 and 6.15 (pages 68-69) for temperature of $\frac{2}{3}T_0$. Units for all variables are summarized in Table 10.1. The relative error of the correlation is $\pm 9\%$ for $P = 68.3\%$, and $\pm 15\%$ for $P = 90\%$. The linear regression of the relative error is in Equation 10.2 bellow.

$$T_{qErr} = \pm \left(T_0^{2.01} \cdot \frac{[(35e-5)\rho_{q66}]^{7.44}}{C_{q66}^{1.73} k_{q66}^{2.48}} \frac{c_{in0}^{0.15}}{\delta_i^{0.15} z_i^{0.19} P_{e0}^{0.024}} + 6.4 \right) \qquad [°C] \qquad (10.2)$$

The main lack of this result and results of experimental studies in general is, that it tries to put together rewetting and/or quenching temperature as it was described on page 122. If quenching temperature will be assumed as solid-liquid contact temperature regardless of the existence of a stable vapor film, then it rises naturally with increasing initial wall temperature. On the other hand, once the surface temperature is above the temperature limit introduced in section 10.2.1.2 part "Limit Temperature" (page 122), the quenching temperature ceases to be dependent on initial wall temperature and the quench front advance must "wait" for stable vapor layer collapse. It is difficult or almost impossible to affect the independence in one correlation and moreover, there is not enough experimental data to do so. But the presence of this limit is evident. There are several outliers in Figure 10.9 from this reason, especially between "x" values of $(0.5 \div 0.7)e + 27$. These points belong to Model A at low flow rates and high initial wall temperatures. Another region of overestimated quenching temperatures lies bellow "x" value of $0.2e + 27$. This region consists of measured points of TC1 on model C, where initial wall temperature is relatively low and no boiling region is visible in this case.

However several conclusions on quenching temperature behavior can be based just on presented correlation result:

- It strongly depends on initial wall temperature. This influence is clear up to limit temperature as it was described above.

- It rises with rising flow rate which is in agreement with Baumeister and Simon [1], i.e. stronger flow disturbs forming vapor layer at quench front and the surface can be rewetted at a higher temperature.

- It decreases with increasing wall thickness. This influence is less evident at the first sight and it is closely tied to other parameters. The effect of wall thickness on precooling was mentioned in section 10.2.1.1 on page 120

- Influence of position on cooled geometry goes with quenching delay and thus with greater precooling of the wall.

- The effect of the internal heat source is also less evident. The value of heat source is dependent on initial wall temperature in this study because reflood process is started by the steady state of initial wall temperature and silica glass surface temperature.

Higher generated heat heats up the wall and decreases the pre-cooling effect. It can be equal to precooling effect or even greater at high initial wall temperatures.

As can be seen from these conclusions, the only true parameter, that can cause rewetting at higher wall temperatures is coolant flow rate for given model.

It must be also noted, that Equation 10.1 includes the effect of precooling caused by pressure peaks described in sections 10.2.1.1 and 10.1.1. Another integral part of the solution is the effect of spacers which are part of the test channel.

10.2.2   Nucleate Boiling Temperature

Nucleate boiling temperature represents a temperature limit, where the last two phase boiling regime is present. The temperature is found via maximum second order derivative of the temperature profile. The nucleate boiling point separates two-phase boiling regimes, i.e. regions, where coolant has a saturation temperature, and single phase rewetted region. Definition of nucleate boiling correlation offers the possibility to create three-regional heat transfer coefficient map in combination with known quenching temperature.
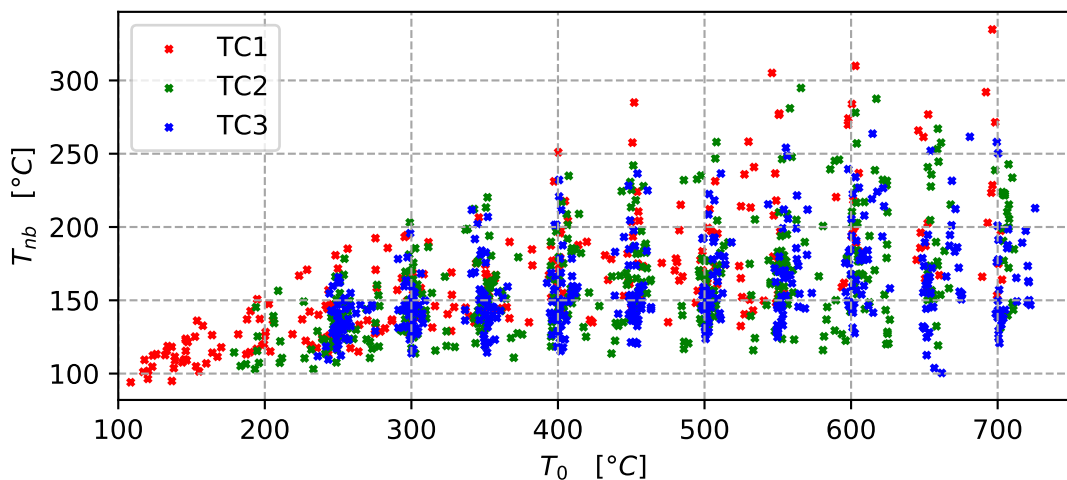
Figure 10.10: Nucleate boiling temperatures for all models and flow rates

Figure 10.10 shows, that nucleate boiling temperature is close to saturation temperature for low initial wall temperatures and rises slightly with experimental conditions. However, most of these values lie on temperature level around $150\,^\circ C$. The nucleate temperature is burdened by considerable uncertainty due to the difficult identification of the point in second-order derivatives of the temperature profile. While "quenching edge" of the profile is relatively sharp, the curvature beyond the nucleate boiling point is much milder in most cases. This makes its finding harder.

Figure 10.11: Nucleate boiling temperature data correlation

Despite the considerable scattering of values, a correlation of nucleate boiling temperature has been established in order to obtain an approximate idea of its value. The correlation scatter plot is sh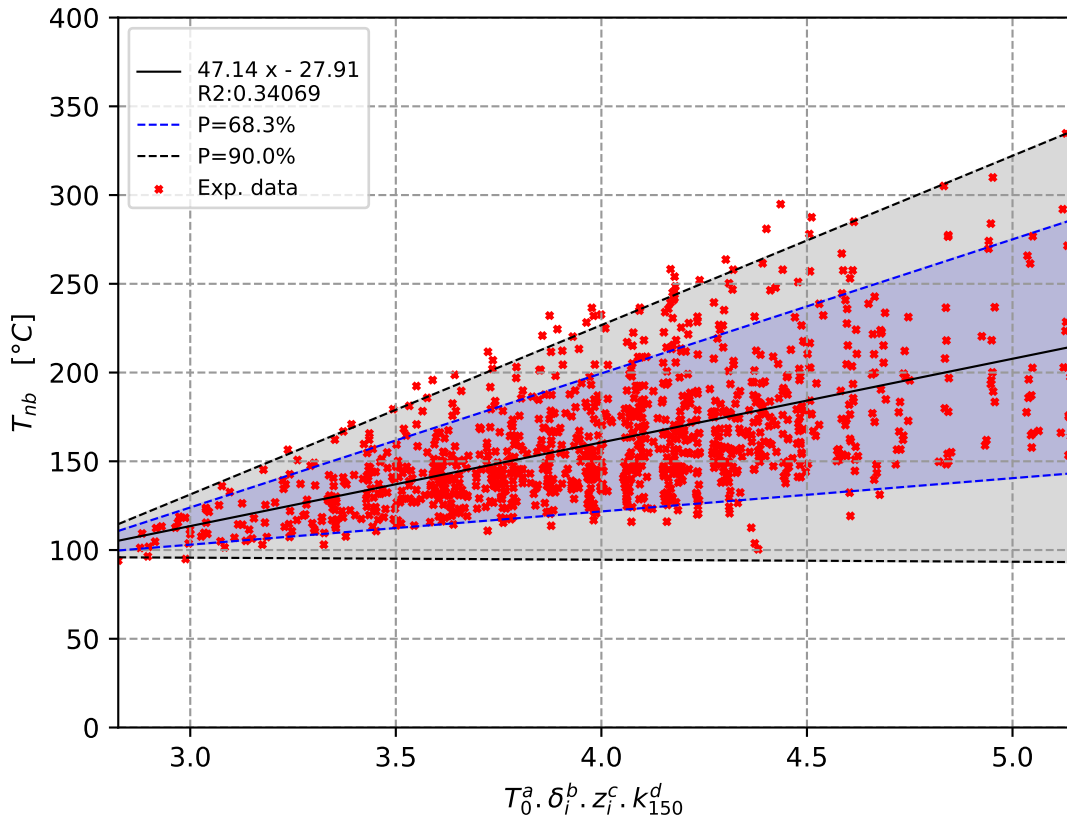own in Figure 10.11 and resulting equation is in Equation 10.3. Surprising was the fact, that the temperature turned out to be almost independent on the coolant velocity. For this reason, the velocity term was neglected in the final equation as well as the internal source term. The internal source term is actually subject to initial wall temperature.

$$T_{nb} = 47.1 \frac{T_0^{0.25}}{z_i^{0.1} \delta_i^{0.13} k_{150}^{0.35}} - 28 \qquad [°C] \tag{10.3}$$

where T_0 is the initial wall temperature, δ_i is wall thickness and z_i is axial position. The heat conduction k_{150} was calculated for $150\,°C$. The mean relative error is $\pm 20\%$ for $P = 68.3\%$, and $\pm 34\%$ for $P = 90\%$ or it can be calculated using Equation 10.4.

$$T_{nbErr} = \pm \left(16 \frac{T_0^{0.25}}{z_i^{0.1} \delta_i^{0.13} k_{150}^{0.35}} - 42 \right) \qquad [°C] \tag{10.4}$$

10.3 Heat Transfer Coefficients

Results from heat transfer calculation described in Section 9.8 are presented in this section. These results contain dependence of heat transfer coefficient on given position, flow rate and initial wall temperature.

10.3.1 Semi-Spatial View on HTC

Semi-spatial heat transfer coefficients were defined as a value of HTC, which depends on relative distance to quench front. The positive value of QF distance in presented results means a position behind the front and negative otherwise. As it was mentioned in Section 9.8 the coolant temperature up to the nucleate boiling point was taken as $100\,°C$ and behind this point, the coolant temperature was calculated through "cascade" algorithm.

The thermocouple TC2 (position $0.835\,mm$) for all three models with mass flux of $80\,kg.m^{-2}.s^{-1}$ was taken as a representative sample of resulting data. At this low flow rate are clearly visible all common features of the time-spatial dependence of heat transfer coefficient.

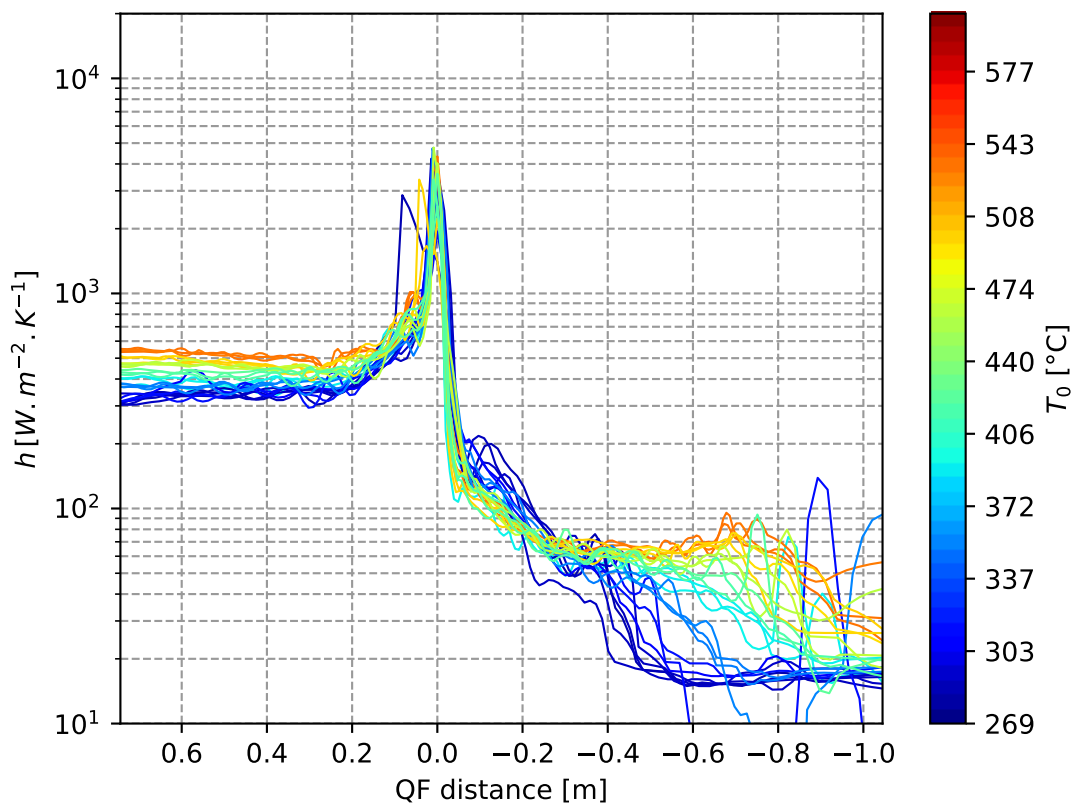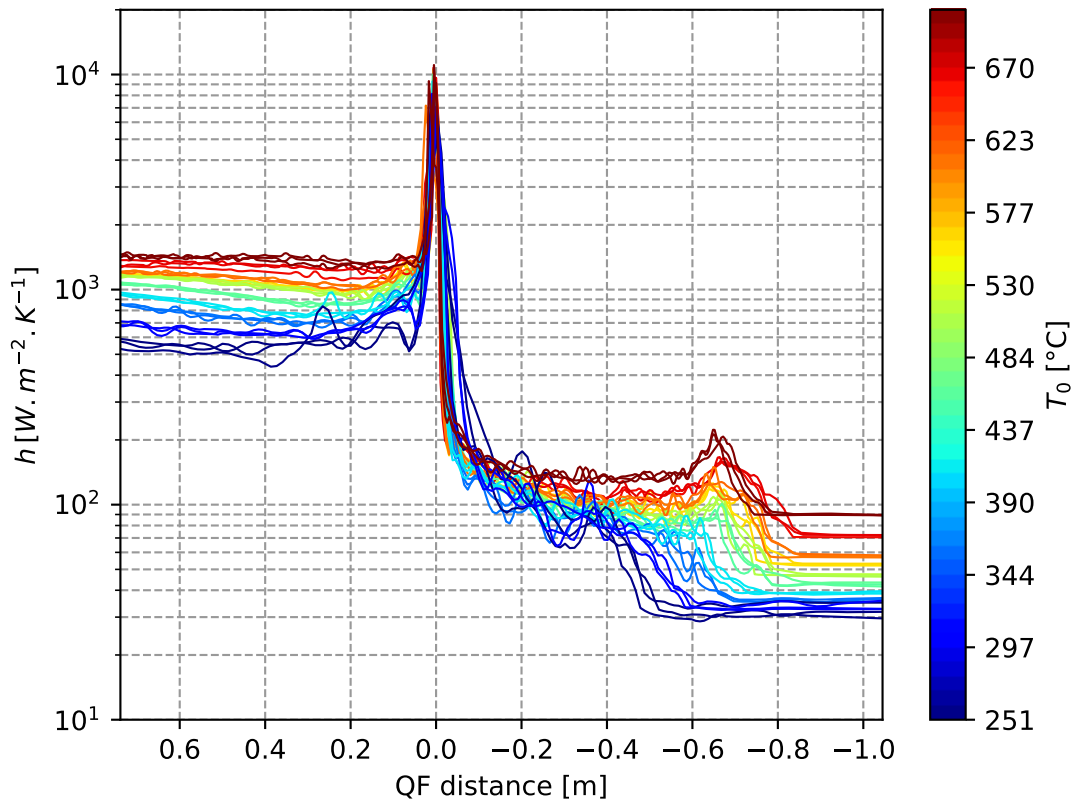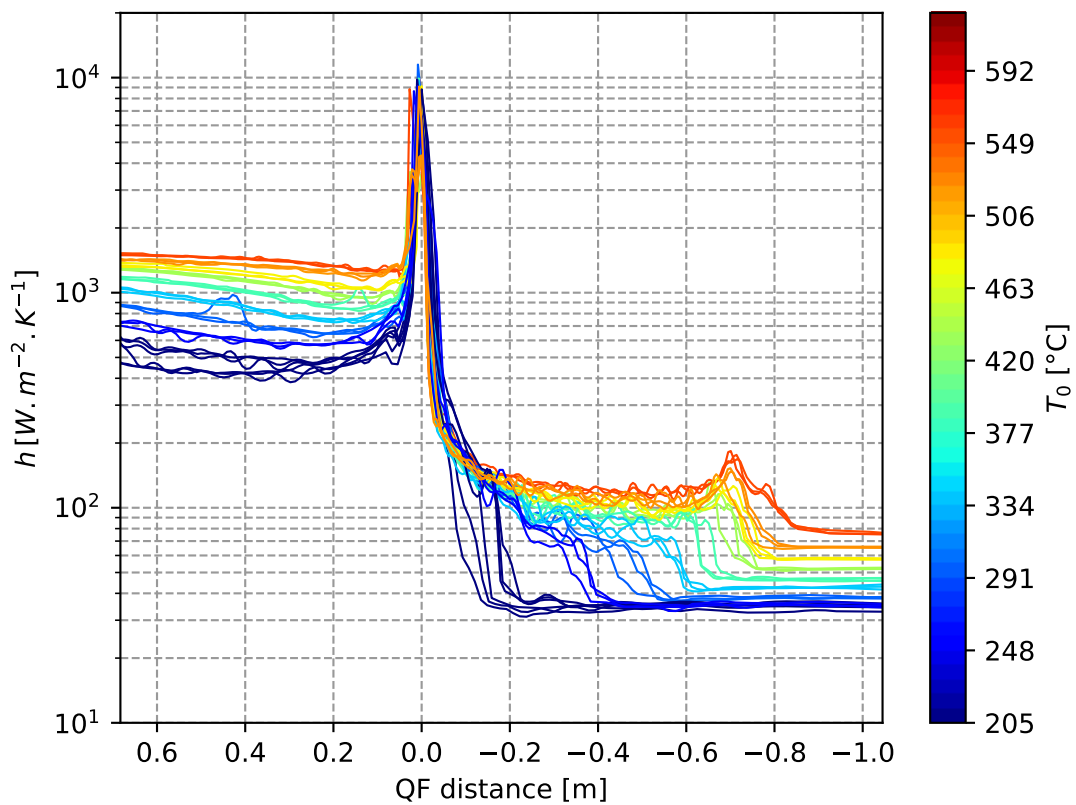Figure 10.12: TC2: HTC vs distance to quench front (Model A, $G = 80\,kg.m^{-2}.s^{-1}$)

Figure 10.13: TC2: HTC vs distance to quench front (Model B, $G = 80\,kg.m^{-2}.s^{-1}$)

Figure 10.14: TC2: HTC vs distance to quench front (Model C, $G = 80\,kg.m^{-2}.s^{-1}$)

Figures 10.12, 10.13 and 10.14 show the dependence of HTC on distance to quench front (negative values represent positions in front of the QF and positive values otherwise) for middle thermocouple TC2 for all three models. All three plots can be divided into three separated regions. The first region in front of the quench front, second one near the front (between quenching and nucleate boiling point) and the last one behind the front.

- The region in front of the quench front is cooled only by steam and sputtered water droplets. With rising initial wall temperature we can observe rising heat transfer coefficient value. This increase is caused by increased amount of evaporated water at the quench front, which moves at higher speed through the channel. This one-phase vapor cooling creates a constant plateau along the dry region. An HTC peak is present at the beginning edge of the plateau. This peak is formed by rapid steam generation, while water meets the hot surface at the beginning of the flooding phase. The plateau is followed by the increasing slope right in front of the quench front, where the heat transfer coefficient is increased by sputtered droplets.

  At very low initial wall temperatures, a very low HTC region can be observed in front of the single-phase plateau. The behavior is clearly visible in Figure 10.14, which shows HTC for the variable tube. In its case, no vapor is generated because no quench front is formed yet. Until coolant meets enough hot surface (it depends on electric current and actual wall thickness), the heat transfer coefficient remains very low. In this case, the surface is cooled by heat radiation.

- The second region is characterized by the sharp peak of heat transfer coefficient. Its value is dependent on the amount of accumulated heat i.e. wall thickness and specific heat of the tube. The surprising fact is, that value of critical HTC is not unambiguously dependent on initial wall temperature for given flow rate. At higher temperature levels the critical temperature is also higher and thus the resulting heat flux (assuming saturated two-phase mixture as a coolant) has to be lower. Related results are presented in the next sections. HTC values from presented figures show, that Model C has a slightly lower value of critical HTC than Model B and Model A has half CHF value than other two models. The similarity between Model B and Model C is caused by similar wall thickness at the given axial position. The HTC values are in good agreement with actual wall thicknesses (considering almost identical specific heats).

- The third region is single-phase region behind the front, i.e. region cooled by water. The actual heat transfer coefficient value within the region is mainly dependent on the electrical resistance of the tube, which results in higher heat flux and thus in coolant temperature in this region. As the quench front advances forward, flow rate slightly decreases and this causes higher coolant temperature and slightly rising heat transfer coefficient. Remaining fluctuations can be caused also by varying coolant inlet temperature during the experiment run.

10.3.2 Local Heat Transfer Coefficients

10.3.2.1 HTC at Critical Heat Flux Point

The critical heat flux point is located at the point, where the maximum value of the first order derivative reaches its maximum value (absolute value). This point is located right behind the quenching/rewetting point, so the wall is already rewetted. In this region, a heat flux rapidly rises up and this causes intense extraction of accumulated heat from the wall (internal heat source is insignificant compared to accumulated heat change, see Figure 9.10 on page 99).
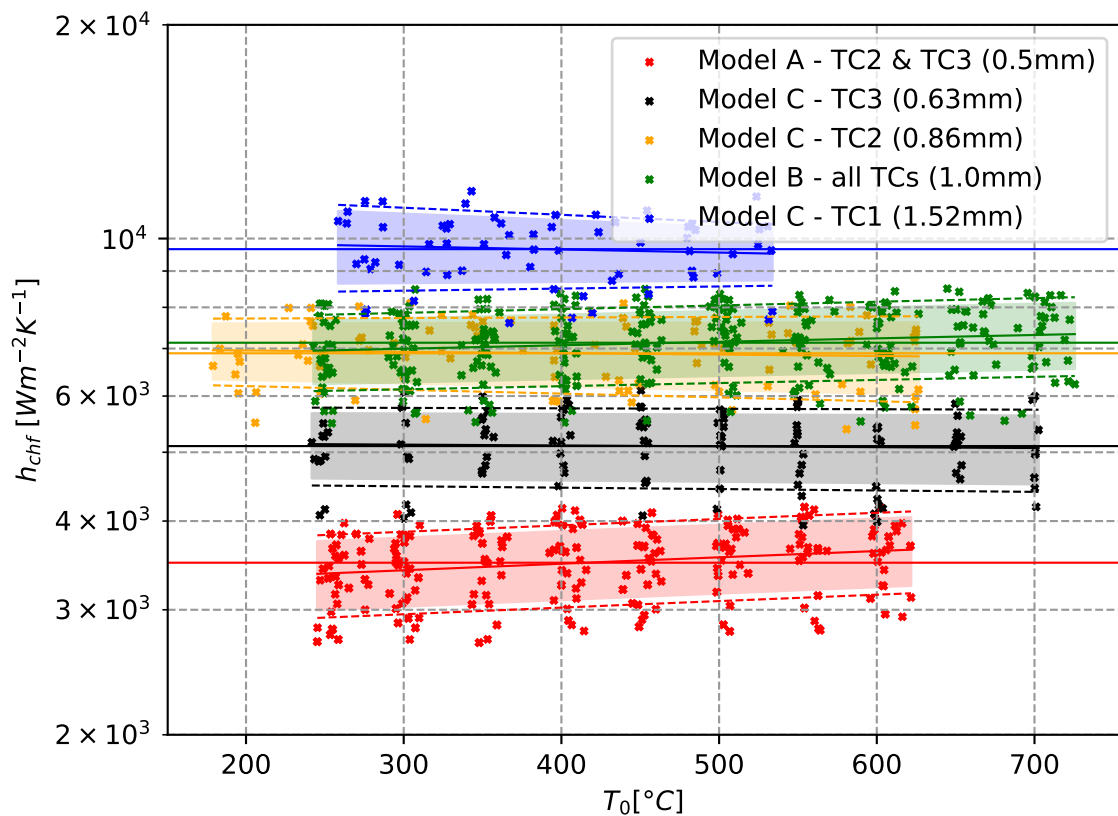

Figure 10.15: Complete sets of CHF heat transfer coefficients vs initial wall temperature

All heat transfer coefficients in this region were checked for their dependence on initial wall temperature, flow rates and position along the geometry. The only provable dependence of the critical heat flux heat transfer coefficient is dependence on accumulated heat, i.e. dependence on wall thickness, density, and specific heat. The product of density, capacity and wall thickness can be understood as a ability to accumulate heat per area of the wall. A term "area-specific heat" was used for this ability. This result is in agreement with the claim in the previous paragraph. These HTCs are showed in Figure 10.15. The dependence of HTC on wall thickness is clearly appreciable. It can be noted, that dependence on wall thickness provides an opportunity to use thermocouples on Model C as three measured points. This approach was applied in Figure 10.15 already.

NOTE: Because of inconsistent behavior of TC1 in Model A caused by the wrong installation of the thermocouple, its results are not presented in the section. Moreover, the thermocouple was destroyed during experiments at high temperatures, so its results at initial wall temperatures above 600°C are excluded from results
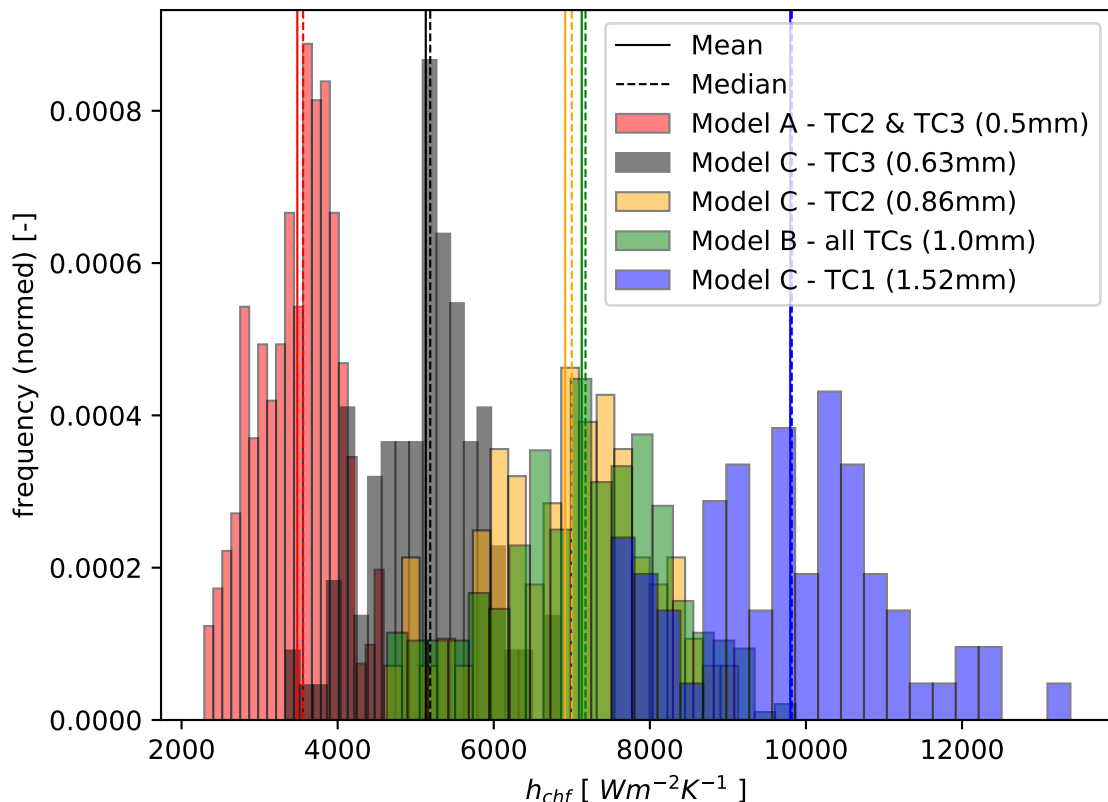

Figure 10.16: Histogram of critical HTC

The scattering of heat transfer coefficients shows normal distribution of experimental

data. This scattering is showed in Figure 10.16. In the case of TC1 on Model C, a greater scattering of experimental data can be observed. This scattering is caused by lower quenching temperatures which causes a faster quenching of the point. Thus more interpolating points were applied.
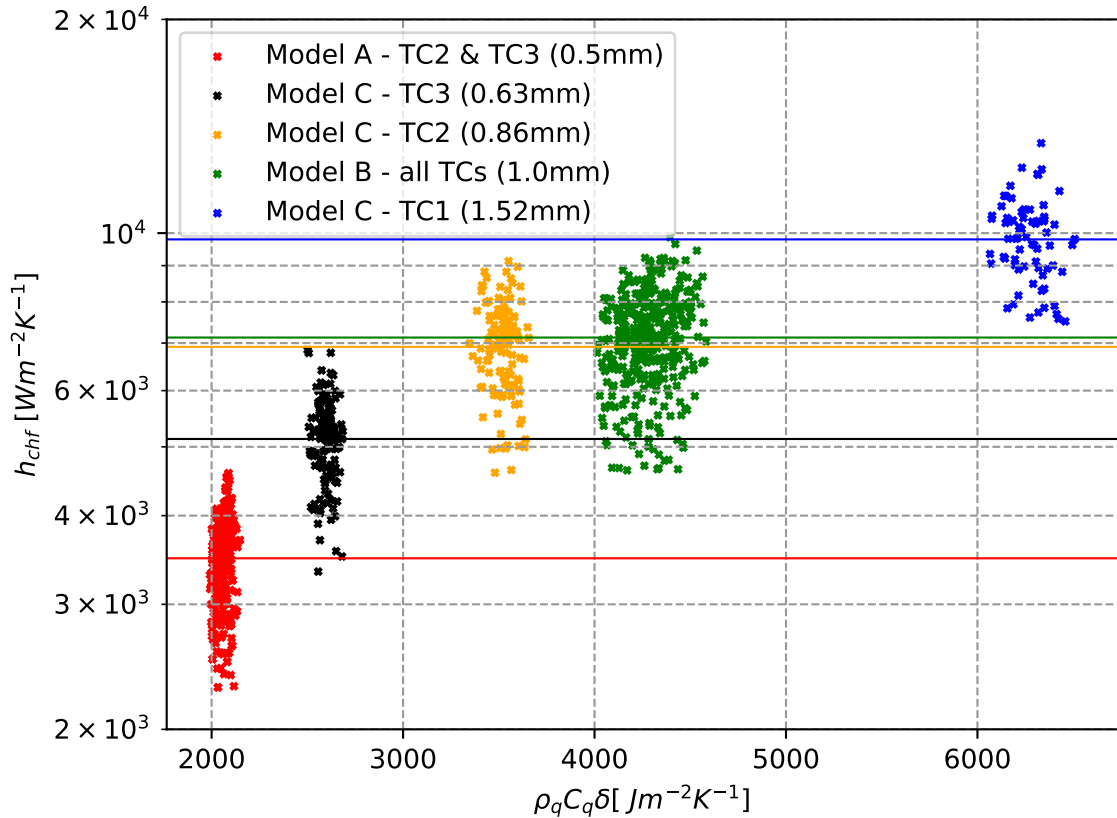
Figure 10.17: Dependence of critical HTC on area-specific heat

Critical CHFs are plotted against area-specific heat in Figure 10.17. This chart gives a good connection to the mentioned statement, that critical HTC is dependent on wall thickness (characteristic length), density and specific heat. The values of density and specific heat are calculated for the critical temperature of the wall via material property equations for the corresponding material of the model. Horizontal scattering is caused by the uncertainty of critical temperature detection. It is clearly visible, that $1.52\,mm$ wall thickness has approximately three times higher heat transfer coefficient than the point with $0.5\,mm$ wall thickness.

The data were approximated using second order least square polynomial fit. The resulting approximation is shown in Figure 10.18 and its equation is in Equation 10.5. The material properties were taken for quenching temperature, since quenching temperature is already solved in Equation 10.1 (page 124) and it can be assumed, that temperature

properties will be changed insignificantly between these two points.

$$h_{chf} = -(1.7\mathrm{e}{-}4) \cdot (\rho_q C_q \delta_i)^2 + 2.8 \cdot (\rho_q C_q \delta_i) - 1290 \qquad [Wm^{-2}K^{-1}] \qquad (10.5)$$

where $\rho_q \, [kg.m^{-3}]$ is the wall density, $C_q \, [J.kg^{-1}.K^{-1}]$ is the specific heat of the wall and $\delta \, [m]$ is the wall thickness. All temperature dependent parameters correspond to properties at critical temperature.

The relative error of the dependence is $\pm 13\%$ for $P = 68.3\%$, and $\pm 22\%$ for $P = 90\%$ of the HTC (h_{chf}) value.
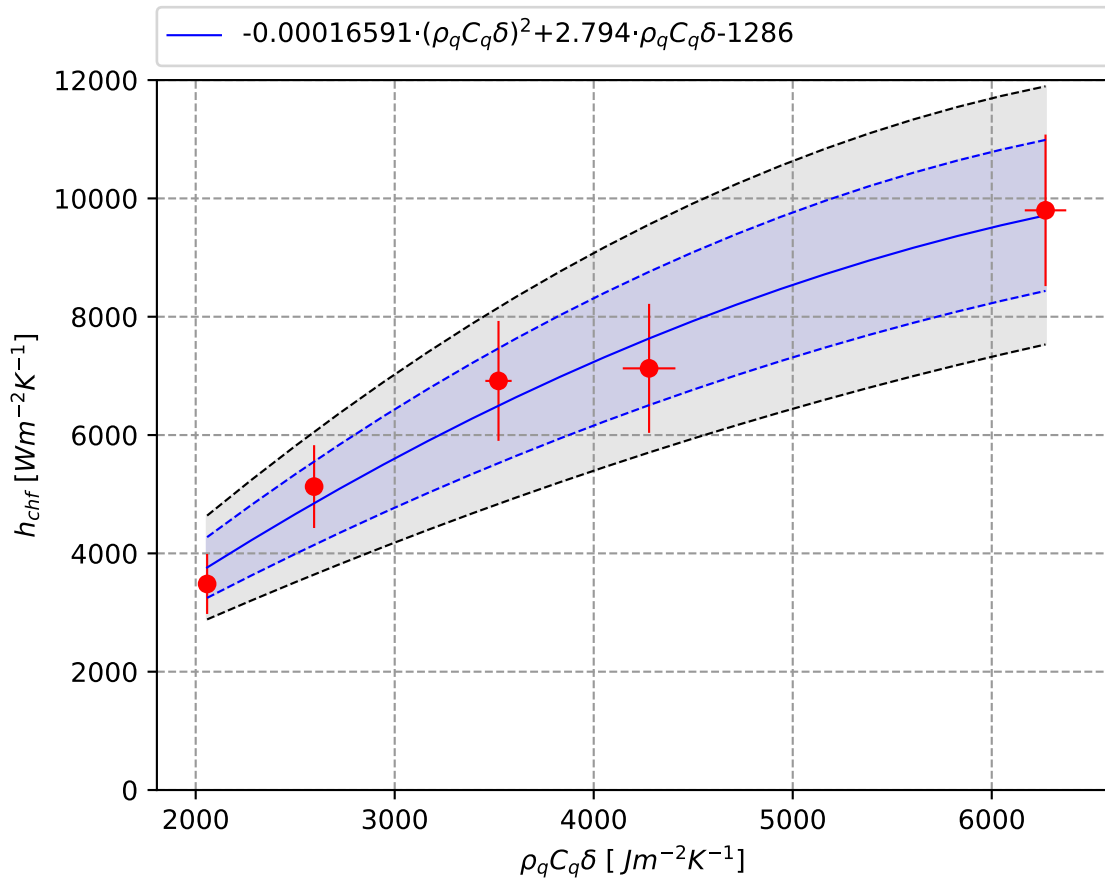

Figure 10.18: Correlated dependence of critical HTC on area-specific heat

10.3.2.2 HTC at Quenching Point

The heat transfer coefficient at quenching point was correlated in a similar way as HTC at critical heat flux point. The point is located at the minimum value of the second-order derivative of the measured temperature profile. From quenching point of view, the

point is located at the head of the quench front, i.e. where the vapor film collapses and water meets the surface. Physically, a relatively high axial conduction takes place due to prompt change of the axial temperature gradient. This axial conduction peak can be also observed in Figure 9.10 on page 99. This behavior supports the concept of conduction controlled rewetting because the conduction is responsible for the definitive collapse of the vapor layer.

A dependence of quenching heat transfer coefficient results from this consideration and this dependence was proved consequently. Besides the quench point HTC dependence, the dependence of HTC at CHF point is not influenced by density and capacity or the influence is insignificant.
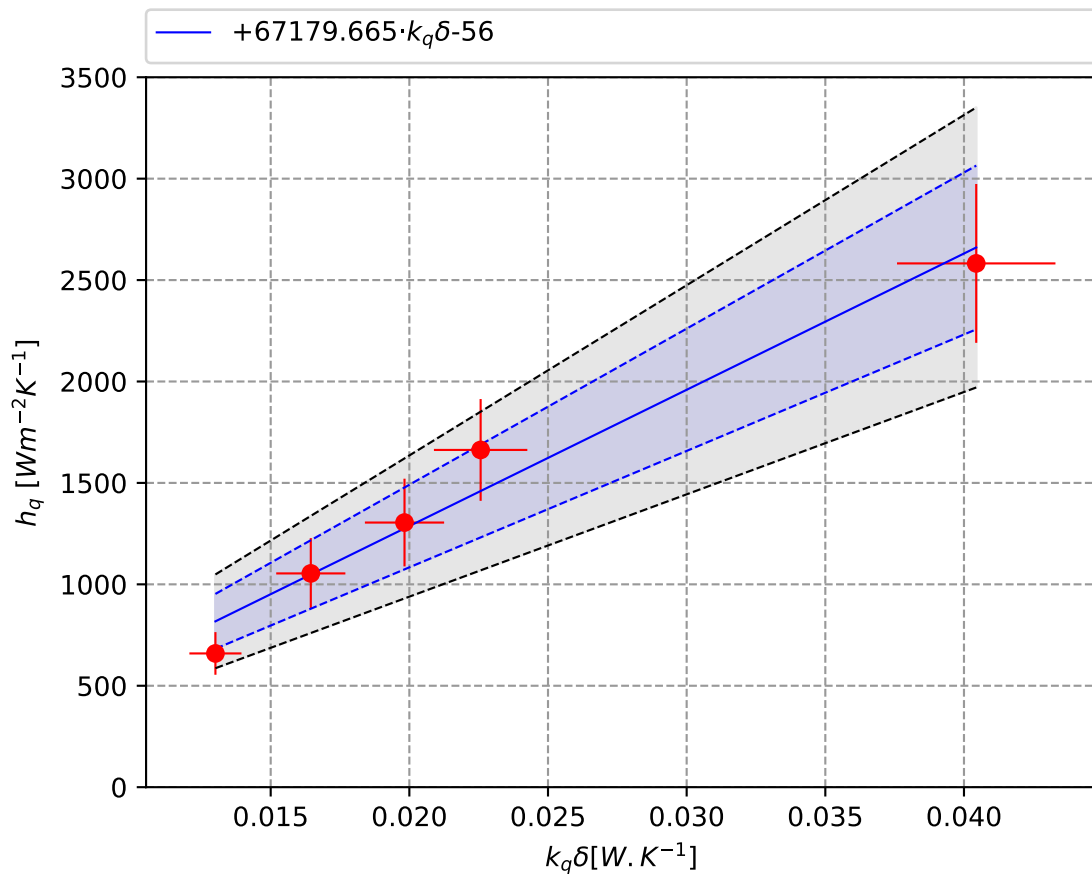
Figure 10.19: Correlated dependence of quenching HTC on heat conduction

Heat transfer coefficients at quenching point are plotted in Figure 10.19. Five red points represent five measured points (two for model A and B and other three points for model C). A value of CHF rises hand in hand with heat conduction coefficient and wall thickness, i.e. conducted amount of heat power per temperature difference. The value of heat conduction coefficient was calculated for according quenching temperature via

material properties of the wall material.

These data were approximated by linear regression in the form:

$$h_q = 67180 \cdot k_q \delta_i - 56 \qquad [Wm^{-2}K^{-1}] \tag{10.6}$$

where $k_q \, [Wm^{-1}K^{-1}]$ is the heat conduction coefficient and $\delta_i \, [m]$ is the wall thickness.

The resulting error of the regression is $\pm 15.6\%$ for $P = 68.3\%$, and $\pm 27\%$ for $P = 90\%$ of the value.

10.3.3 Mean Heat Transfer Coefficients

Following sections contain solutions for mean heat transfer coefficients in three regions: dry region, region between quenching and nucleate boiling point and wet region. These results show dependency on input parameters and they can be used in three regional rewetting models.

10.3.3.1 Mean HTC in Dry Region

As a part of the solution of the three-regional model of the process, a solution for mean dry region heat transfer coefficient was constructed. Heat transfer coefficient in the dry region is actually a combination of radiation and convective heat transfer via vapor and water droplet interaction. Radiation heat transfer alone can be assumed in dry test channel without flowing vapor, i.e. state before flooding initiation at high temperatures. Once the coolant enters the test section a significant amount of vapor is generated at the quench front and the vapor flows through the channel at high speed. The value of heat transfer coefficient proved to be dependent especially on initial wall temperature, and mass flow rate of the coolant.
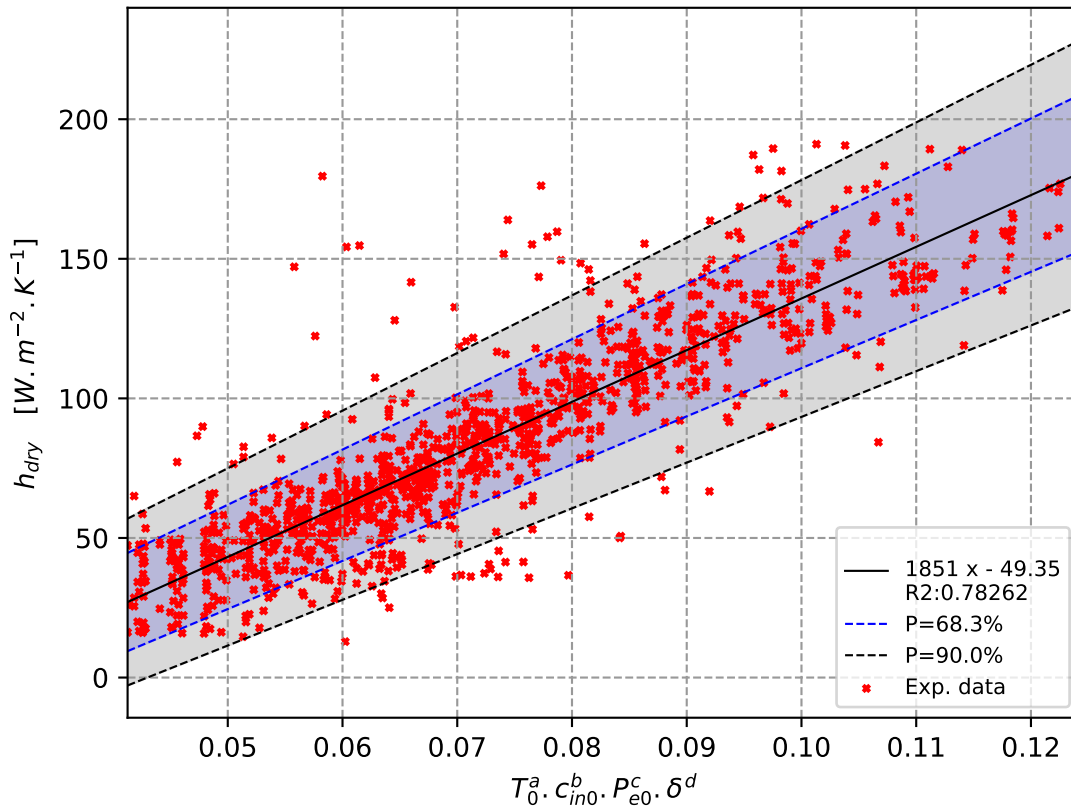
Figure 10.20: Correlated data of mean dry region HTC

Figure 10.20 dependence on chosen set of experiment parameters and Equation 10.7 shows its optimized result. The heat transfer coefficients for the dry region are burdened with a relatively high scattering due to very chaotic and dynamic behavior at the quench front. Because of intense boiling at the front, an uncertain amount of vapor is driven through the channel at the time. The low values of HTC in Figure 10.20 belongs to model C with low initial wall temperature. The coolant begins to boil further from the inlet and this is responsible for very low HTC values. The effect is visible in Figure 10.14 on page 129.

$$h_{dry} = 1851 \cdot \frac{c_{in0}^{0.11} P_{e0}^{0.29} \delta^{0.44}}{T_0^{0.013}} - 50 \qquad [Wm^{-2}K^{-1}] \qquad (10.7)$$

where $c_{in0} \, [m.s^{-1}]$, $P_{e0} \, [MW.m^{-3}]$ and $T_0 \, [°C]$ are initial parameters of the experiment - coolant velocity, internal heat source and wall temperature. The mean relative error of the correlation is $\pm 17\%$ for $P = 68.3\%$, and $\pm 29\%$ for $P = 90\%$ of the value.

10.3.3.2 Quenching to Nucleate Boiling Mean HTC

Mean heat transfer coefficient correlation was developed in a similar way as for critical HTC. Its purpose is to serve as mean heat transfer coefficient in the three-regional model. The only difference between CHF and this correlation is, that it requires the inclusion of heat conduction coefficient due to the presence of peripheral coefficients (influenced by relatively high axial conduction) near the quenching and nucleate boiling point.
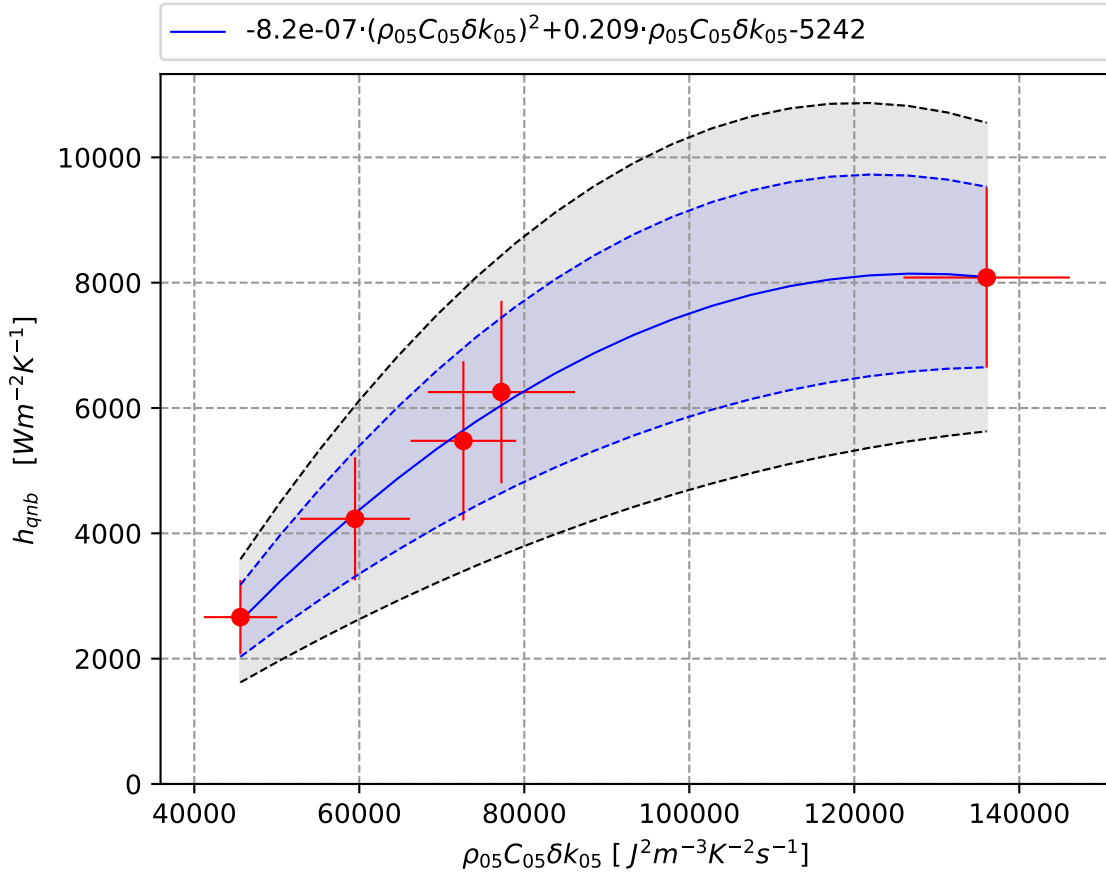
Figure 10.21: Dependence of quenching to nucleate boiling HTC

$$h_{qnb} = -(8.2\mathrm{e}{-}7) \cdot (\rho_{05} C_{05} \delta_i k_{05})^2 + 0.21 \cdot (\rho_q C_q \delta_i k_{05}) - 5242 \qquad [W m^{-2} K^{-1}] \qquad (10.8)$$

Figure 10.21 shows the dependence of mean heat transfer coefficient between quenching and nucleate boiling point on the product of density, capacity, wall thickness, and conductivity. Mentioned parameters were calculated for $50\,\%$ of initial wall temperature. Equation 10.8 approximates the mean HTC values. Its mean relative error is $\pm 20\%$ for $P = 68.3\%$, and $\pm 34\%$ for $P = 90\%$.

10.3.3.3 HTC Behind Nucleate Boiling Point

The region behind nucleate boiling point, i.e. behind nucleate boiling temperature of the wall defined through maximum second order derivative of the temperature profile, is cooled by single-phase water. The flow regime in this region is laminar ($Re < 2300$). The first attempt was to solve heat transfer coefficient through existed correlation (e.g. Mills). It yields good results for low internal heat source value, but with rising heat source and thus surface heat flux (electrically generated heat is equal to heat transferred to coolant in this region), heat transfer coefficient increased. The increase is probably caused by the narrow channel and by the presence of spacers. However, a correlation for single-phase region was constructed as a function of Reynolds number, Prandtl number, internal heat source and wall thickness. The result is showed in Figure 10.22 and in Equation 10.9.
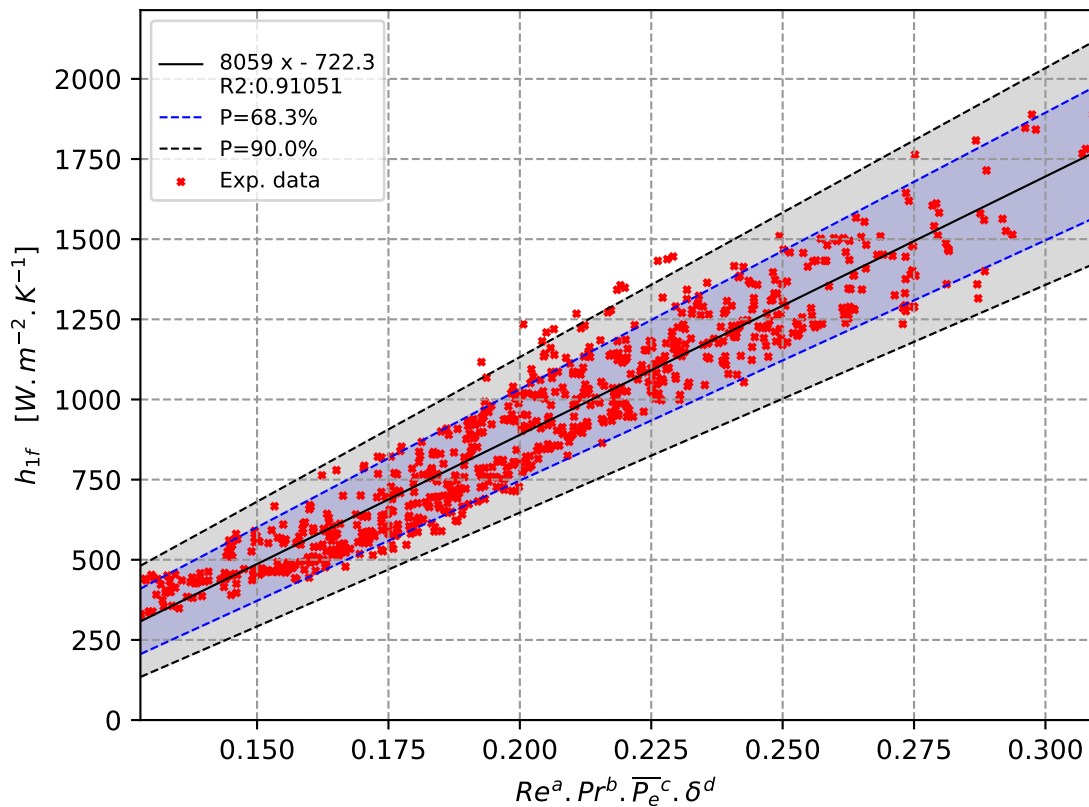

Figure 10.22: Correlated data of post nucleate boiling HTC

$$h_{1f} = 8059 \cdot Re^{0.156} Pr^{0.124} P_e^{0.16} \delta_i^{0.47} - 722 \qquad [W m^{-2} K^{-1}] \qquad (10.9)$$

where

$$Re = \frac{c_{in} \cdot D_h}{\nu} \qquad [-] \qquad (10.10)$$

Prandtl number was taken from IAPWS97 tables, $q_e\,[MW.m^{-3}]$ is internal heat source, $\delta_i\,[m]$ is the wall thickness, $D_h\,[m]$ is hydraulic diameter of annular channel (see Table 6.5 on page 66), $c_{in}\,[m.s^{-1}]$ is the inlet velocity of the coolant and $\nu\,[Pa.s]$ is kinematic viscosity of the coolant. The mean relative error is $\pm15\%$ for $P = 68.3\%$, and $\pm25.5\%$ for $P = 90\%$.

10.4 Three-Regional 1-D Model

10.4.1 Definition of Regions and Boundary Points

A three-regional model was developed based on results from previous sections. This model consists of the dry region in front of the quench front, quenching-to-nucleate boiling region and single-phase region with forced convection. The graphical representation of the model is in Figure 10.23.
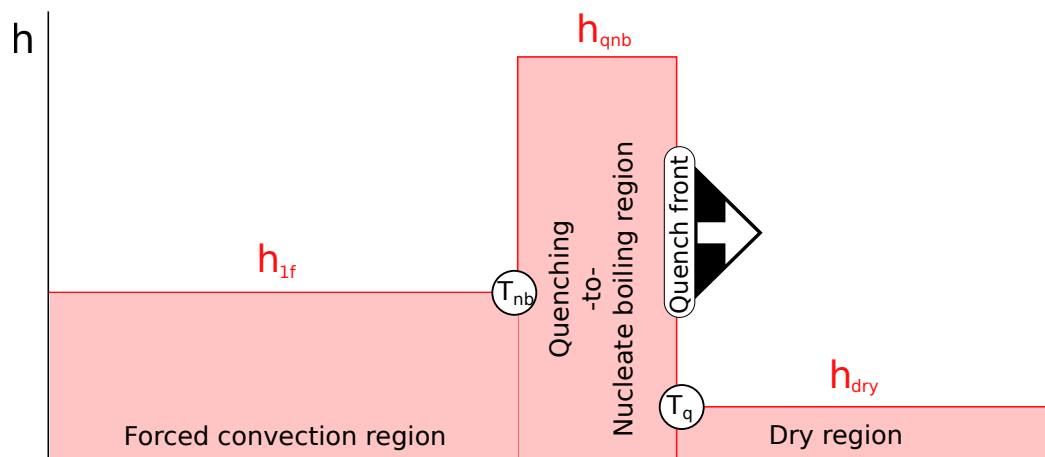
Figure 10.23: Three-regional model suitable for present study

The model is defined by two boundary temperatures:

- Quenching temperature T_q - Equation 10.1, p.124

- Nucleate boiling temperature T_{nb} - Equation 10.3, p.127

and three mean heat transfer coefficients, one for each region:

- Dry region HTC - h_{dry} - Equation 10.7, p.137

- Quenching to nucleate region HTC - h_{qnb} - Equation 10.8, p.138

- Forced convection region HTC - h_{1f} - Equation 10.9, p.139

10.4.2 1-D Calculation

The three regional model was employed into simple numerical calculation through hybrid 1-D non-stationary case. Model A with the initial wall temperature of $600\,°C$ and with the flow rate of $80\,kg.m^{-2}.s^{-1}$ has been chosen as a representative sample. The Crank-Nicolson finite difference method was applied in solution in finite element heat balance procedure. Initial parameters were set to the same values as the compared experimental ones. Solved total flooding time was $50\,s$ with the time step of $0.066\,s$. Quenching temperatures, nucleate boiling temperatures and all heat transfer coefficients were calculated via equations described in the previous sub-section.

Boundary conditions (BCs) were defined as:

- Adiabatic boundary condition at inner surface

- Adiabatic at endpoints

- h_{dry} if $T_0 > T_w > T_q$; $T_{cool} = 100\,°C$

- h_{qnb} if $T_q \geq T_w \geq T_{nb}$; $T_{cool} = 100\,°C$

- h_{1f} if $T_{nb} > T_w$; $T_{cool} = 30\,°C$
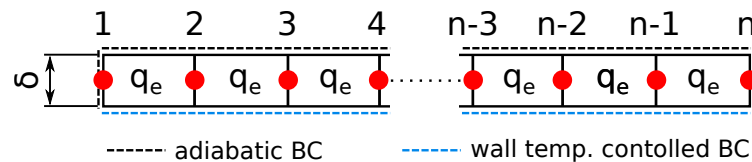
Figure 10.24: 1-D Nodalization of the wall

The nodalization of the domain is shown in Figure 10.24. Figure 10.25 contains spatial solutions of temperatures through time (black line). As can be seen, the domain consists of $1.5\,m$ long "wall" and $0.4\,m$ long upstream region for process development. Influence of initial conditions fades away in this region until front reaches the first TC (probe). Flooding process in the domain was initialized by definition of cold nodes at the beginning.
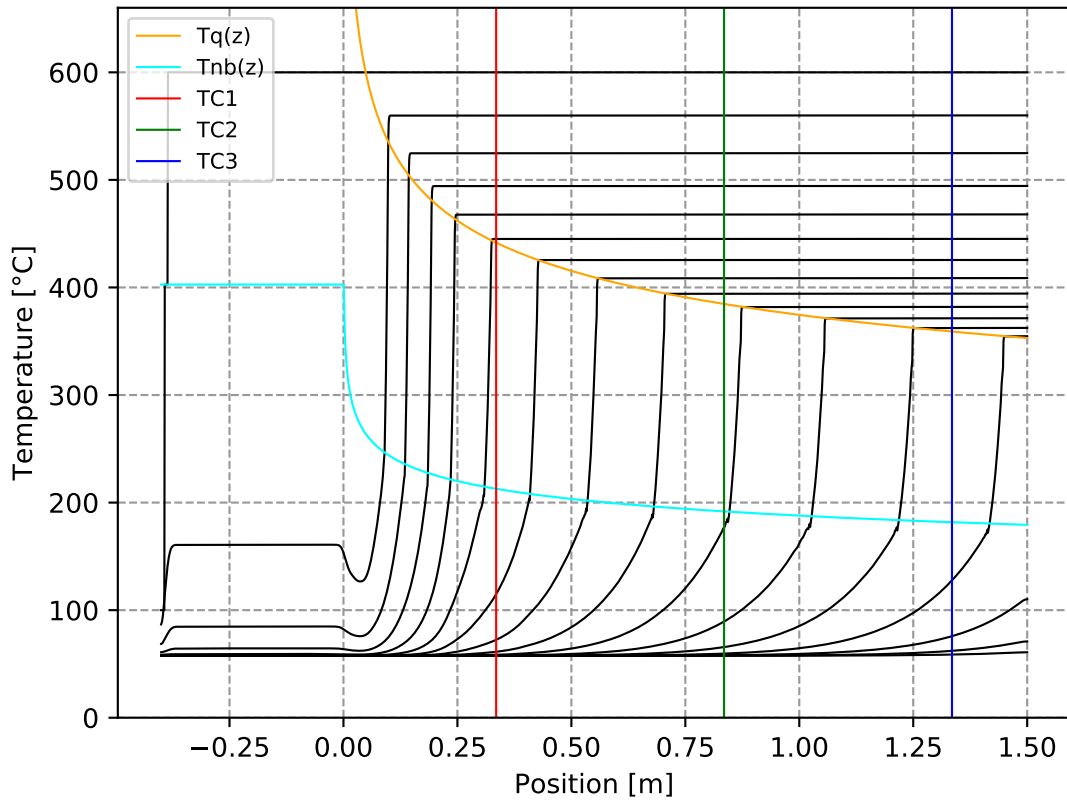
Figure 10.25: Solution of temperature profiles along the domain through time
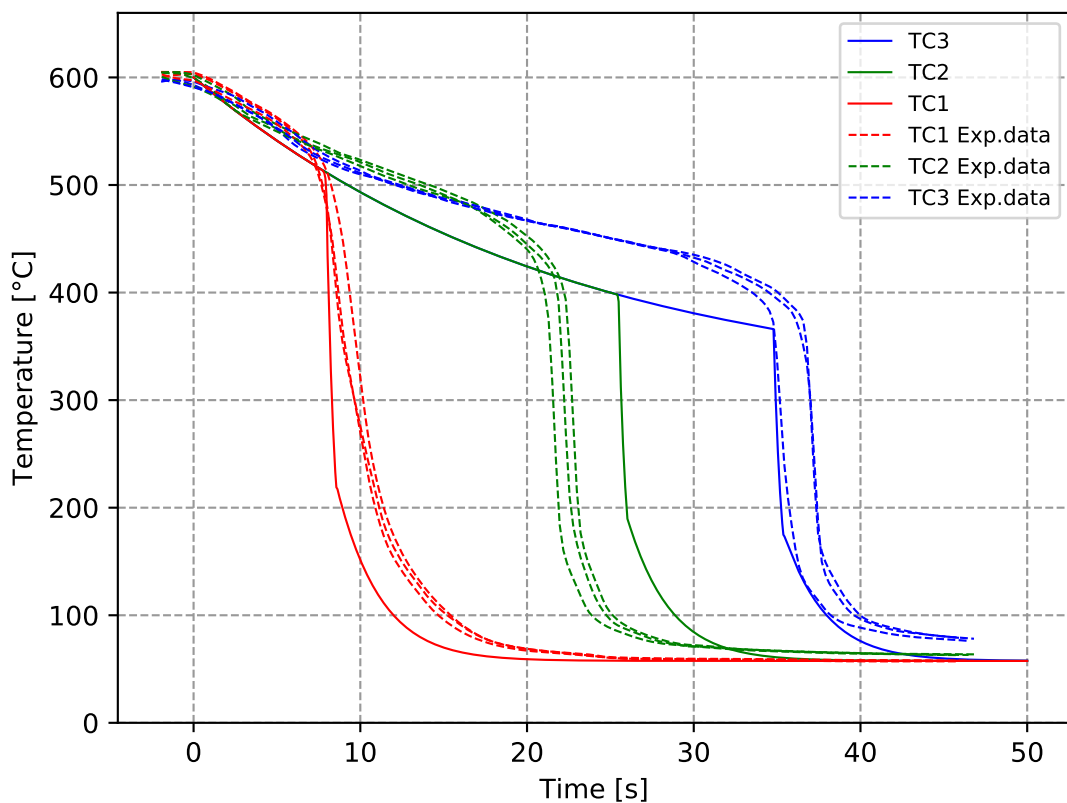
Figure 10.26: Resulting temperature profiles at specified points

Heat profile solutions for specified points (the same axial positions as positions of thermo-couples in the test section) is plotted in Figure 10.26. It shows relatively good agreement, despite the simplicity of the task, with experimental data with the sharp-edge profile at quench points. This sharp edge is a product of 1-D definition of the case and forced control of boundary conditions. This sudden change in boundary conditions simply does not include the sputtering effect. Moreover, the temperature deflection in dry region is possibly cased by constant stream coolant temperature (including absence of droplets). On the other hand temperature profile behind nucleate boiling temperature shows good agreement with experimental data. Other time deviations are probably consequences of spacers neglection, which can't be easily reflected in the case definition.

10.5 Quench Front Velocity

10.5.1 Absolute Velocity

The mean quench front velocity for each model and temperature level was obtained through Equation 9.9 on page 92. This value gives us information on the front velocity between thermocouples TC1 and TC3, i.e. the heated position of $0.335\,m$ and $1.335\,m$. Results for each model type are plotted in Figures 10.27, 10.28 and 10.29. In general, an apparent influence of initial wall temperature and coolant mass flux is evident from these results. This behavior is in good agreement with expectations. [A3], [A4]

The results were approximated by the least square method with automated polynomial order search for the lowest fitting error. From standard deviation and corresponding Student's coefficient of these values, a weighted error range was calculated.

The error range is greater at lower temperatures and high flow rates in most of the cases. High wall temperatures (over $400\,^\circ C$) have a tendency to stabilize the flooding process. At lower temperatures, a physical quench front profile is much more chaotic and this causes greater scattering of measured values. Moreover, in the case of high coolant flow rates (especially at $270\,kg.m^{-2}.s^{-1}$), the greater error range is caused by lower time density of scanned data. For this reason, the interpolated temperature profiles and its derivatives are responsible for its resulting uncertainty.
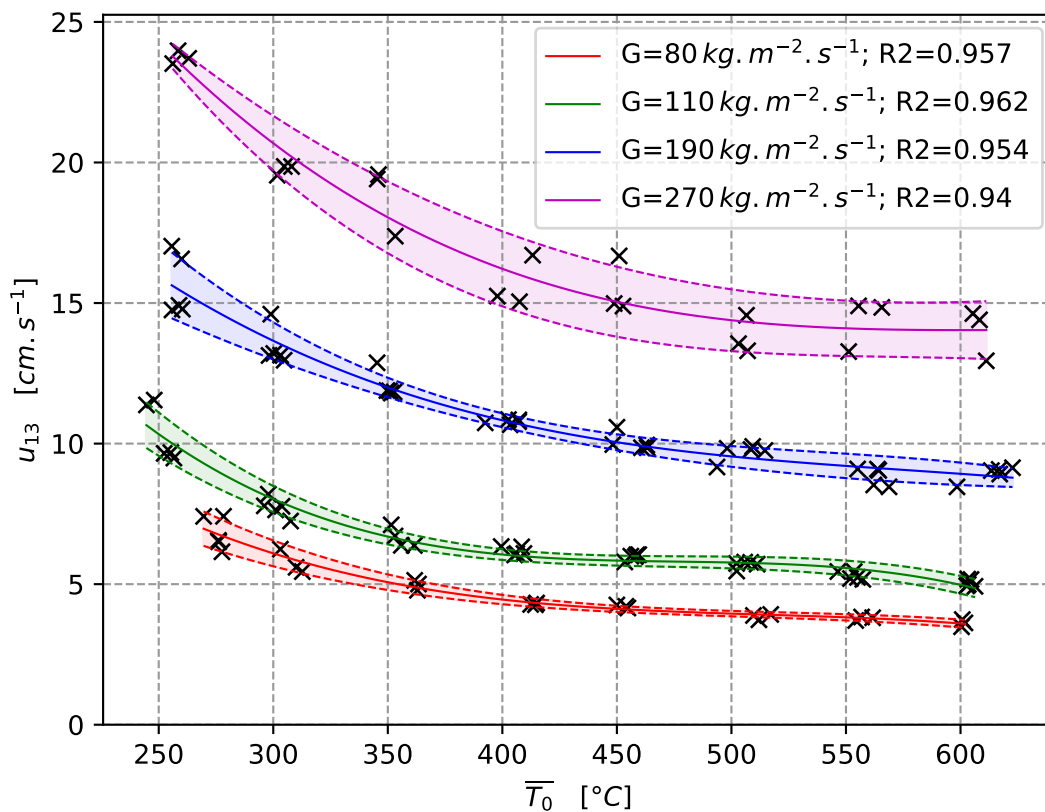
Figure 10.27: Mean quench front velocity for Model A
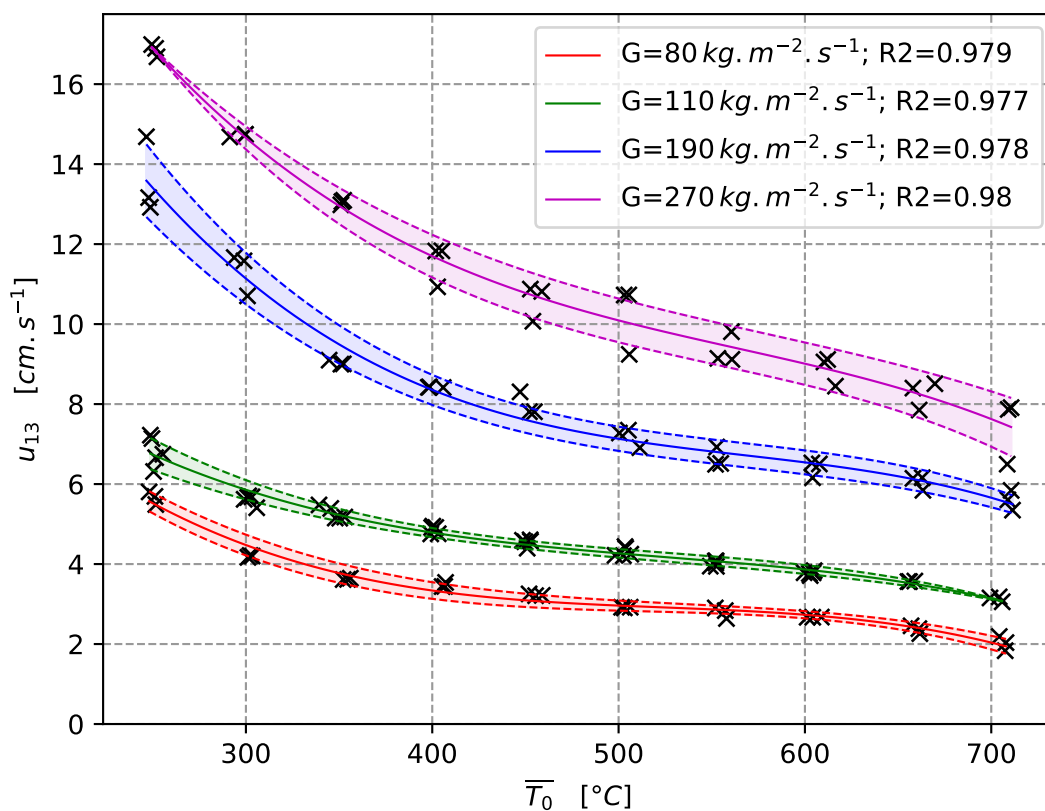
Figure 10.28: Mean quench front velocity for Model B
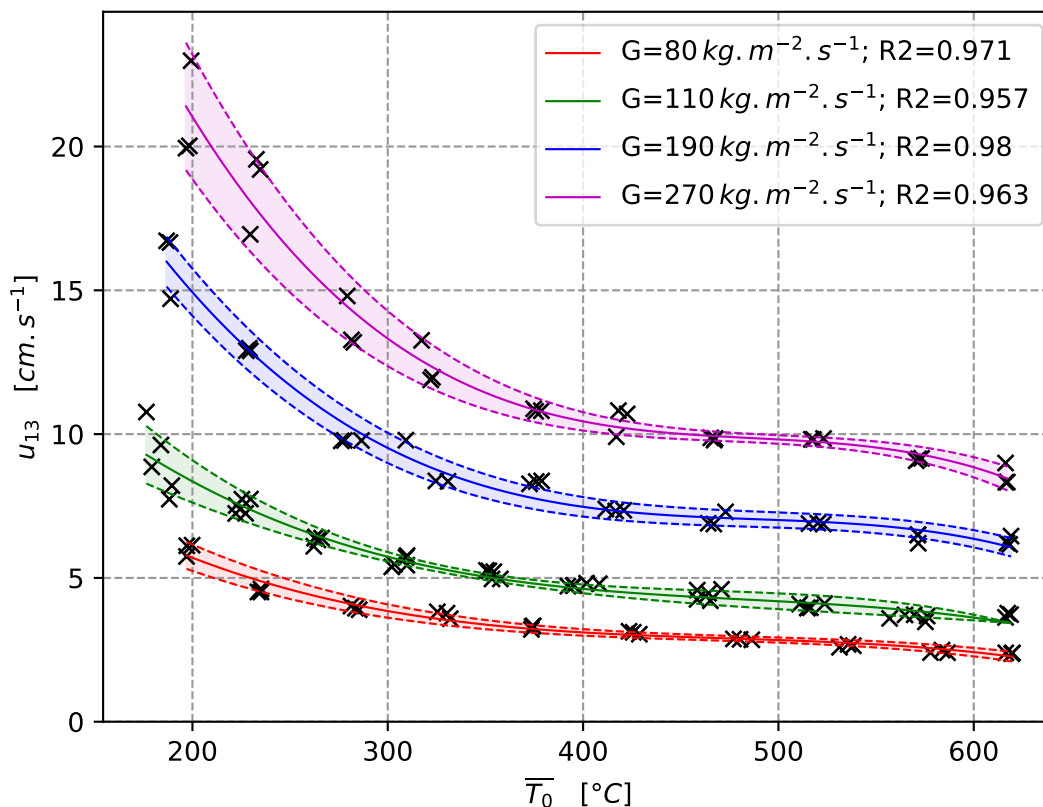
Figure 10.29: Mean quench front velocity for Model C

From all three previous figures (Figure 10.27, 10.28, 10.29) it can be concluded, that quench front velocity decreases with rising initial wall temperature and this decrease is almost constant above $400\,^{\circ}C$. At lower temperature levels the decrease is relatively much bigger. This behavior is evident for tubes with constant wall thickness. Quench front velocity is also strongly dependent on wall thickness. With thicker wall more accumulated heat needs to be removed and this slows down the flooding process.

In the case of variable wall thickness, the initial wall temperature was set at the last thermocouple (TC3), where electric current density and thus wall temperature are the highest. This means, that lower part of the tube has a much lower temperature. The quench front meets different conditions along the tube and this causes strongly spatially dependent front velocity. Equations 10.11 and 10.12 show the relative velocity calculation.

10.5.2   Relative Velocity

The first step was a definition of dimensionless quench front velocity. Very basic idea was to check quench front velocity as a portion of coolant inlet velocity as:

$$U_{13} = \frac{u_{13}}{c_{in13}} \qquad [-] \qquad\qquad (10.11)$$

where

$$c_{in13} = \frac{\int_{t_1}^{t_3} c_{in}(t)dt}{\Delta t_{13}} = \frac{\int_{t_1}^{t_3} \frac{G(t)}{\rho(t)}dt}{\Delta t_{13}} \qquad [m.s^{-1}] \qquad\qquad (10.12)$$
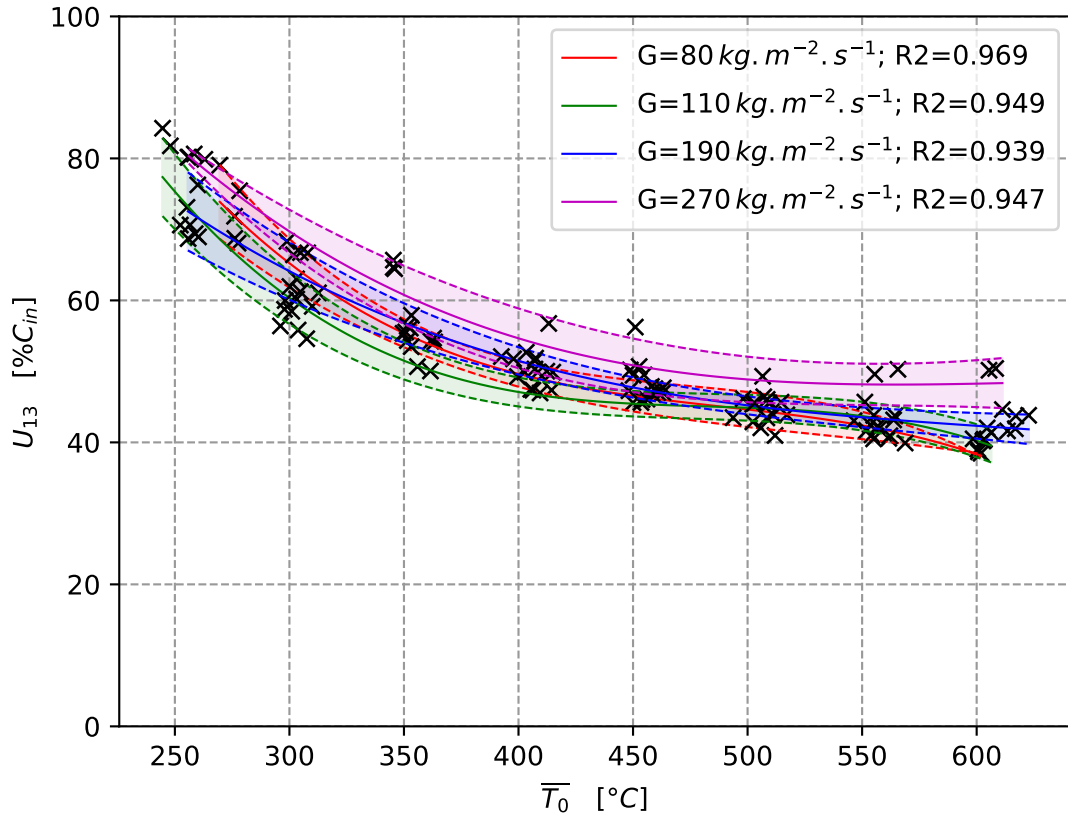
Figure 10.30: Mean relative quench front velocity for Model A

In Figure 10.30, there are plotted relative velocities for all coolant mass fluxes for Model A. A surprising finding is, that consideration of relative front velocity is not dependent on coolant flow rate. Relative quench front velocity scattering is relatively high compared to other two models (Figures 10.31 and 10.32 below). More accumulated heat stabilizes and polishes the flooding process and thus value scattering is much lower. Assuming this evident independence on coolant flow rate, three relative velocity profiles (one for each model) can be constructed. These results are in Figure 10.33 on page 148.
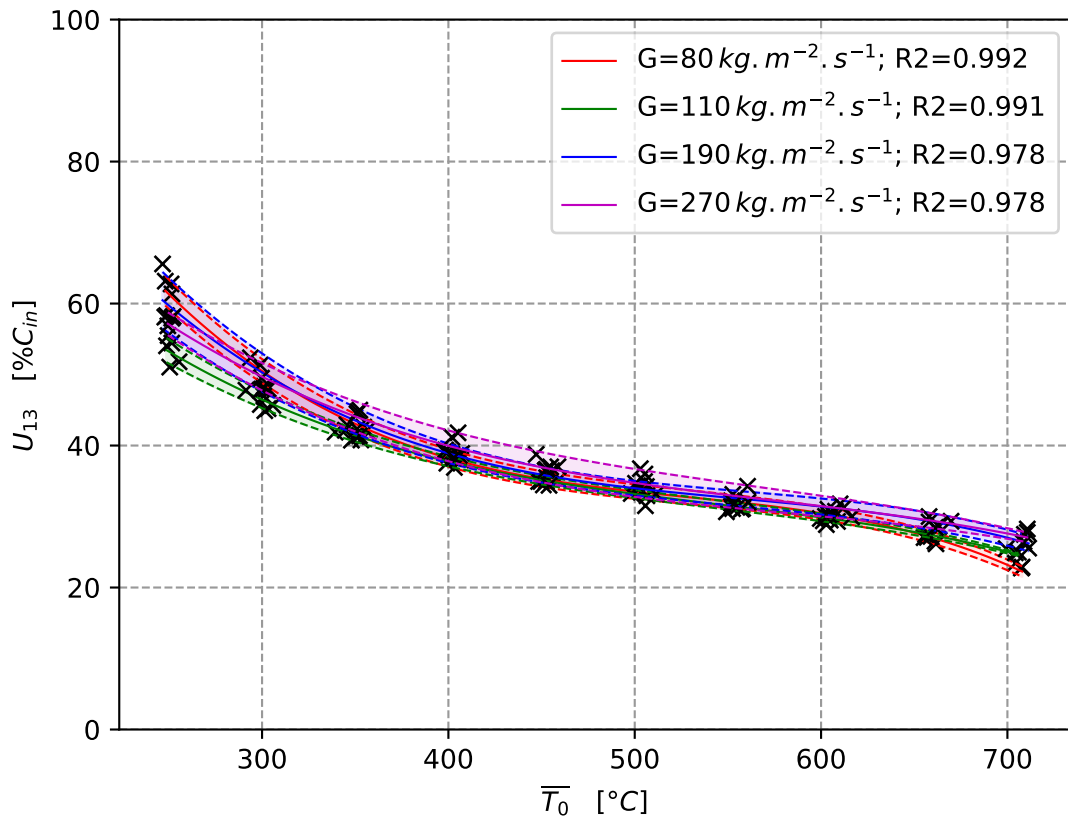
Figure 10.31: Mean relative quench front velocity for Model B
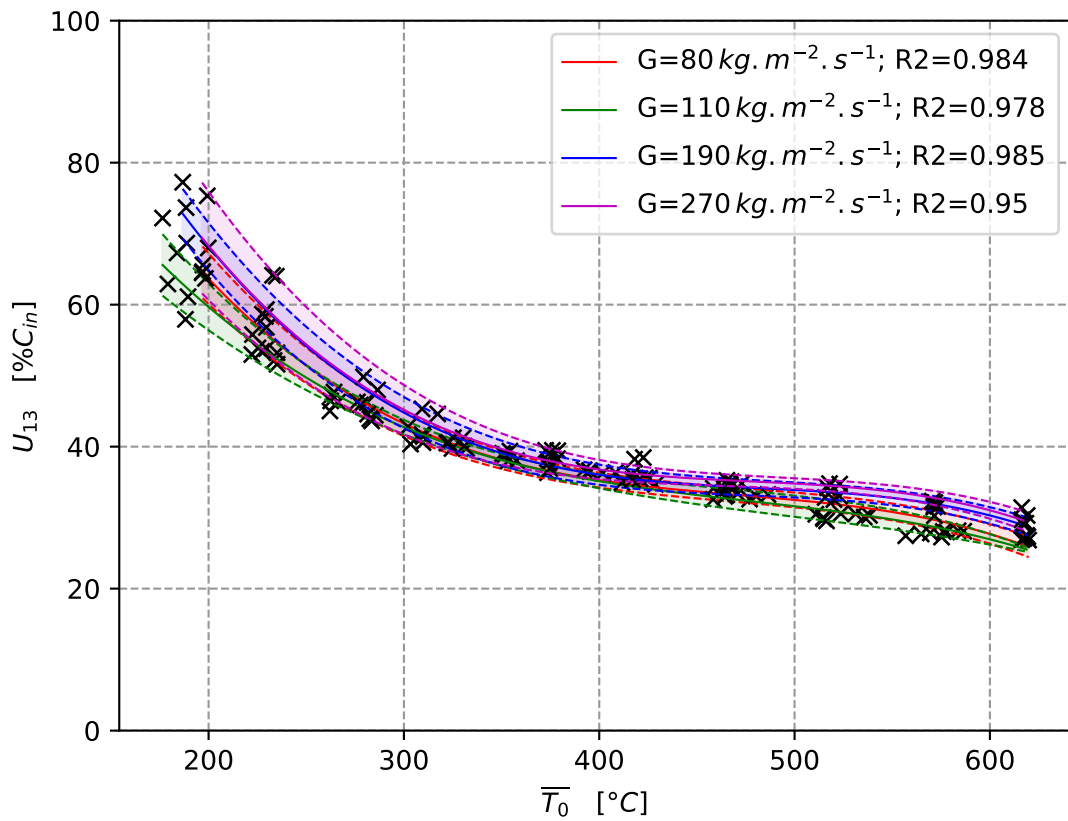
Figure 10.32: Mean relative quench front velocity for Model C
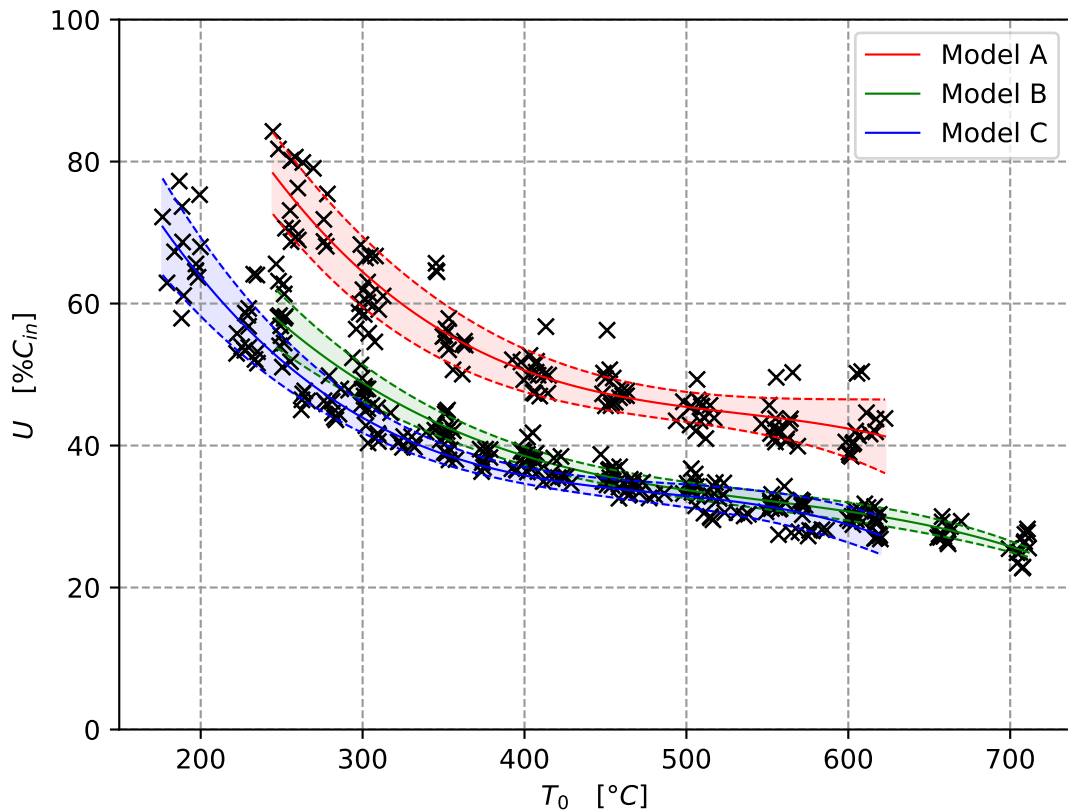
Figure 10.33: Mean relative quench front velocity for all models (TC1 to TC3)

Three dependencies of quench front velocity on initial wall temperature are shown in Figure 10.33. From their trends we can conclude, that Model B has the almost identical shape from temperature level of $400\,°C$ with Model C. At lower temperatures the variable tube has significantly lower initial temperature than other two models. This causes the deflection compared to Model B. Decreasing actual initial wall temperature with the thicker wall in the bottom part of the Model C simply results in higher velocities of the quench front. The Model A suffers from bigger uncertainty due to lower accumulated heat. On the other hand, this lower accumulated heat is also responsible for higher quench front velocity.

10.6 Quench Front Velocity Correlation

A quench front velocity correlation was developed based on presented experimental quench front velocity data from Section 10.5.2. Data shown in Figure 10.33 were correlated incorporating selected variables which are listed below. These variables were chosen through sensitivity analysis of quench front velocity on various variables. The quench front velocity proved to be dependent on these three variables:

- Mean initial wall temperature $\overline{T_0}\,[°C]$

- Mean quenching temperature $\overline{T_q}\,[°C]$

- Mean characteristic length - Wall thickness $\overline{\overline{\delta}}\,[m]$

These variables were chosen based on "All-in-One" correlation test, where other variables were excluded as variables without influence or with negligible influence on the result. Moreover, these variables were chosen as averaged values from all three thermocouples. It must be noted, that most of the material properties are included in the quenching temperature definition which is one of the chosen variables and it is solved by Equation 10.1.

Figure 10.34: Correlated relative quench front velocity for all models (TC1 to TC3)

Figure 10.34 shows the resulting correlation between the chosen variables and relative quenching velocity. The correlation is shown in Equation 10.13 bellow:

$$U_{13} = -0.2363A^3 + 1.587A^2 - 3.701A + 3.327 \quad where \quad A = \overline{T_0}^{-0.83}(\frac{\overline{\overline{\delta}}}{\overline{T_q}})^{1/3} \qquad [-]\ (10.13)$$
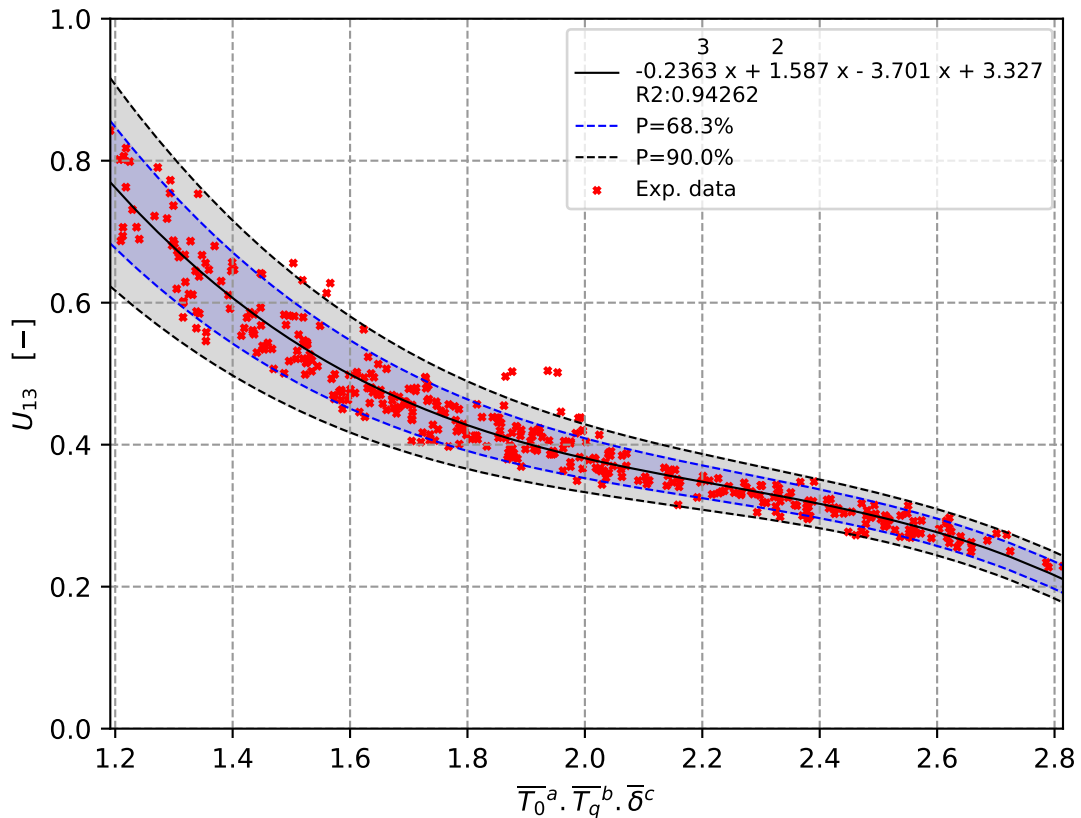
Relative mean average error of the correlation is $\pm 6.5\%$ for $P = 68.3\%$, and $\pm 11.1\%$ for $P = 90\%$. (Meaning of each term and its unit was described in previous paragraphs). The absolute mean quench front velocity is then:

$$u_{13} = U_{13} \cdot c_{in13} \qquad [cm.s^{-1}] \tag{10.14}$$

Based on these results, a partial conclusion can be formulated. For example, the relative velocity of 25 % means, that 75 % of coolant will be evaporated during the reflood process. This also means that we need four times more coolant in order to reflood the geometry than is the volume of the channel. This finding is crucial for applications such as emergency reactor cooling system from water stack point of view.

10.6.1 Quench Front Velocity Validation

Quench front velocity correlation in final form from Equations 10.14 and 10.13, supplemented by Equation 10.1, was validated against experimental data. From this comparison a overall uncertainty is calculated and the result is compared with correlation by Saxena, (2001)[56] (Equation 4.3, p. 51). The mentioned main equations for current study are recapitulated bellow:

$$u_{ab} = U_{ab} \cdot c_{inab}$$

$$U_{ab} = -0.2363A^3 + 1.587A^2 - 3.701A + 3.327$$

$$A = \overline{T_0}^{-0.83}(\frac{\overline{\delta}}{\overline{T_q}})^{1/3}$$

$$\overline{T_q} = \frac{1}{n} \cdot \sum_{i=1}^{n} (T_0^{2.01} \cdot \frac{[(5426e-7)\rho_{q66}]^{7.44}}{C_{q66}^{1.73} k_{q66}^{2.48}} \cdot \frac{c_{in0}^{0.15}}{\delta_i^{0.15} z_i^{0.19} P_{e0i}^{0.024}} + 84)$$

All terms in these equations are described in corresponding sections. Original index 13 was replaced with more general index ab. Where a is the lower quenched point and b is the upper quenched point. This adjustment was introduced as a result of a good agreement of predicted quench front velocity also for other two regions, not only for the region between thermocouples TC1 and TC3. Based on this result, it can be assumed, that prediction capability will be valid for other chosen regions.

Results are plotted against experimental data and correlation by Saxena, (2001)[56] applied to acquired experimental data. The study by Saxena was evaluated on the experimental loop with annular flow channel with the internal heated tube with $1.5\,mm$ wall thickness and with the outer diameter of $15\,mm$. The inner diameter of the outer barrier was $19\,mm$. The temperature range of the study was $200-500\,°C$. Its values were calculated using Equation 4.3 on page 51. As it is evident, the experimental loop has slightly different geometrical and thus hydraulic parameters, but it is one of several studies close enough with the experimental setup to the current study.
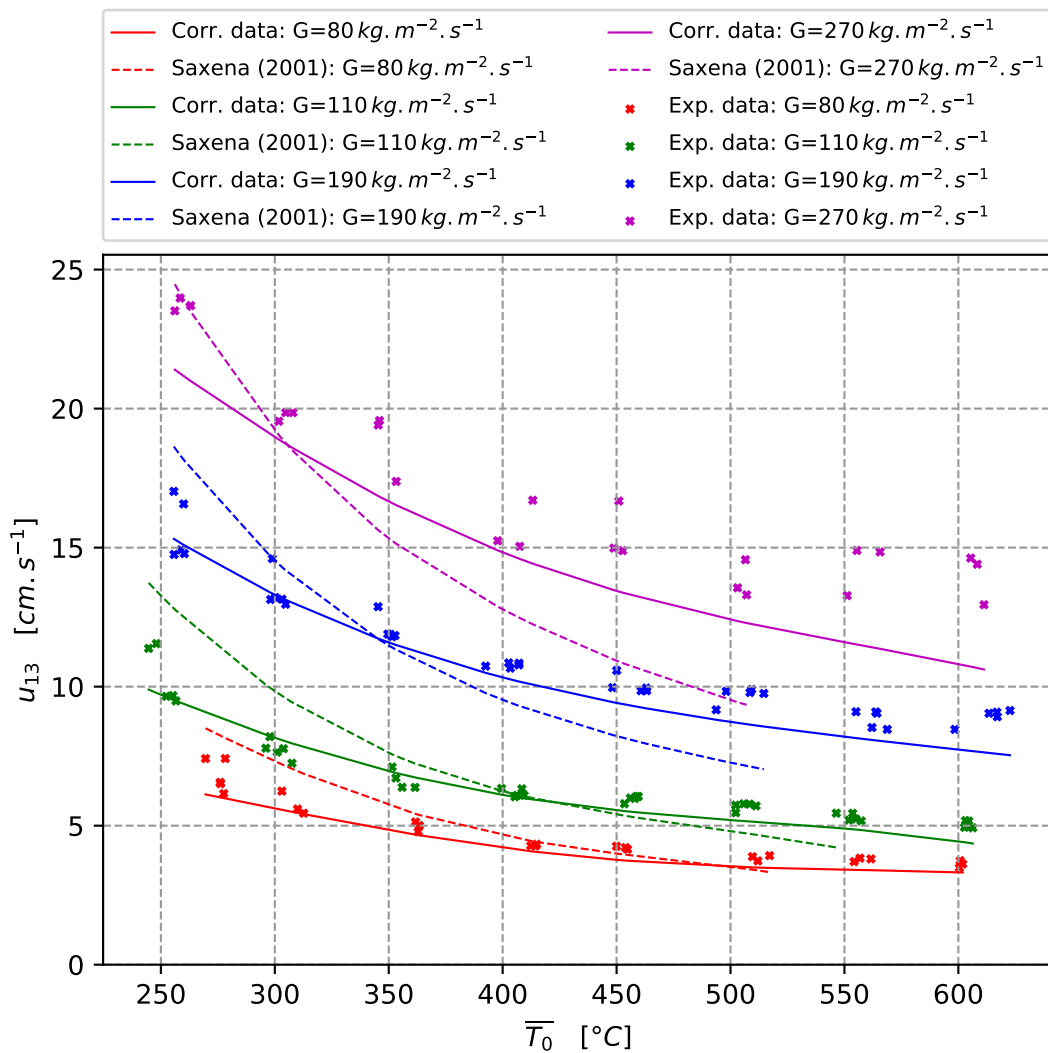
Figure 10.35: Comparison of experimental data and current correlation for Model A

Figure 10.35 shows good agreement with experimental data. The predicted quench front velocity slightly underestimates the real velocity approximately, which is caused primarily by uncertainty in quenching temperature calculation. The relative mean absolute error of quench front velocity prediction is dependent on flow rate and its results are listed

in Table 10.2. As can be seen, the velocity is underestimated more at high initial wall temperatures and for high flow rates.

Table 10.2: RMAE for quench front velocity prediction for Model A

Flow rate $[kg.m^{-2}.s^{-1}]$	RMAE $[\pm\%](P = 68.3\%)$	RMAE $[\pm\%](P = 90\%)$
80	9.2	15.6
110	7.6	13
180	8.0	13.6
270	14.9	25.3
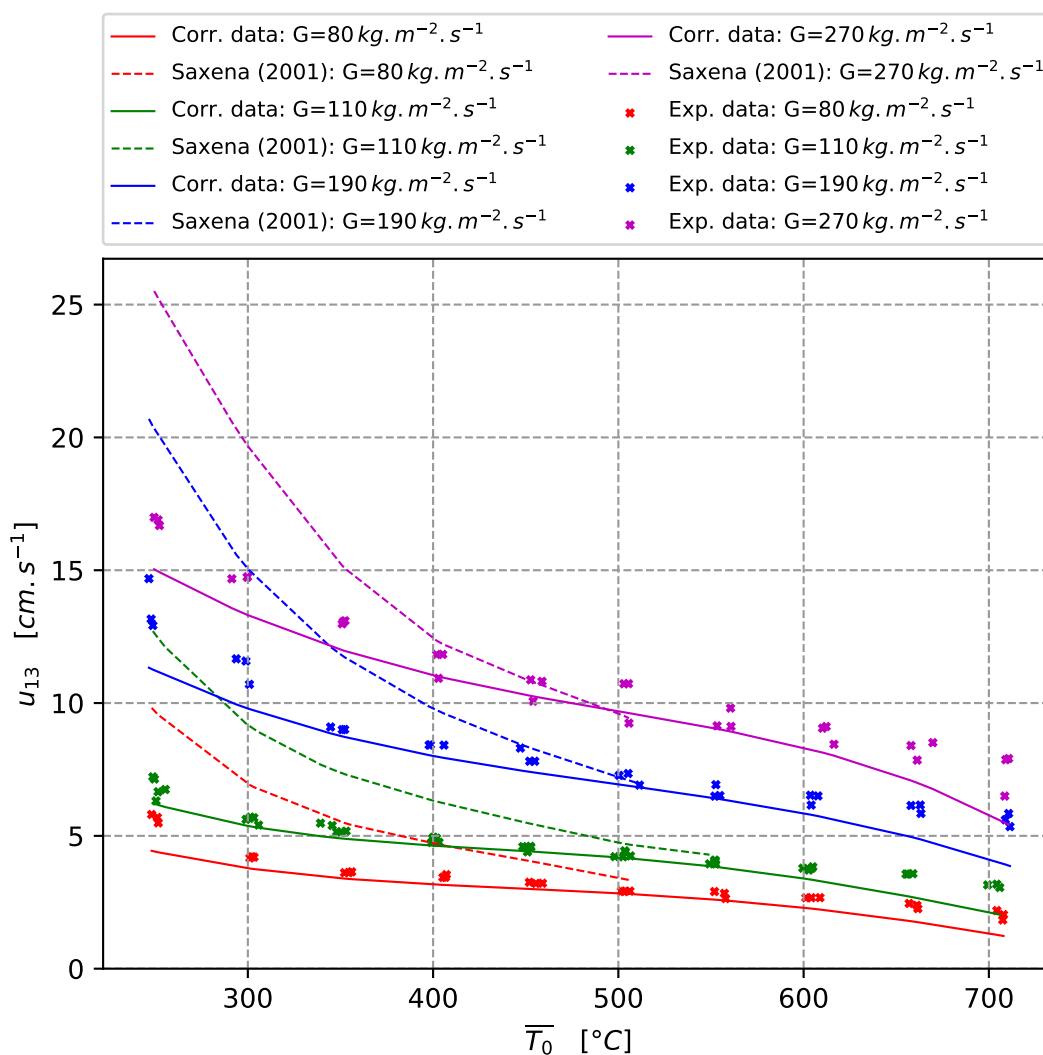
Figure 10.36: Comparison of experimental data and current correlation for Model B

Prediction capability for model B in Figure 10.36 shows lower precision than for model

A (see Table 10.3), but the agreement with experimental data is suitable. On the other hand, the deflection at high initial wall temperatures is lower than in the case of model A.

Table 10.3: RMAE for quench front velocity prediction for Model B

Flow rate $[kg.m^{-2}.s^{-1}]$	RMAE $[\pm\%](P = 68.3\%)$	RMAE $[\pm\%](P = 90\%)$
80	21.2	36
110	11.0	18.7
180	14.5	24.6
270	12.8	21.8
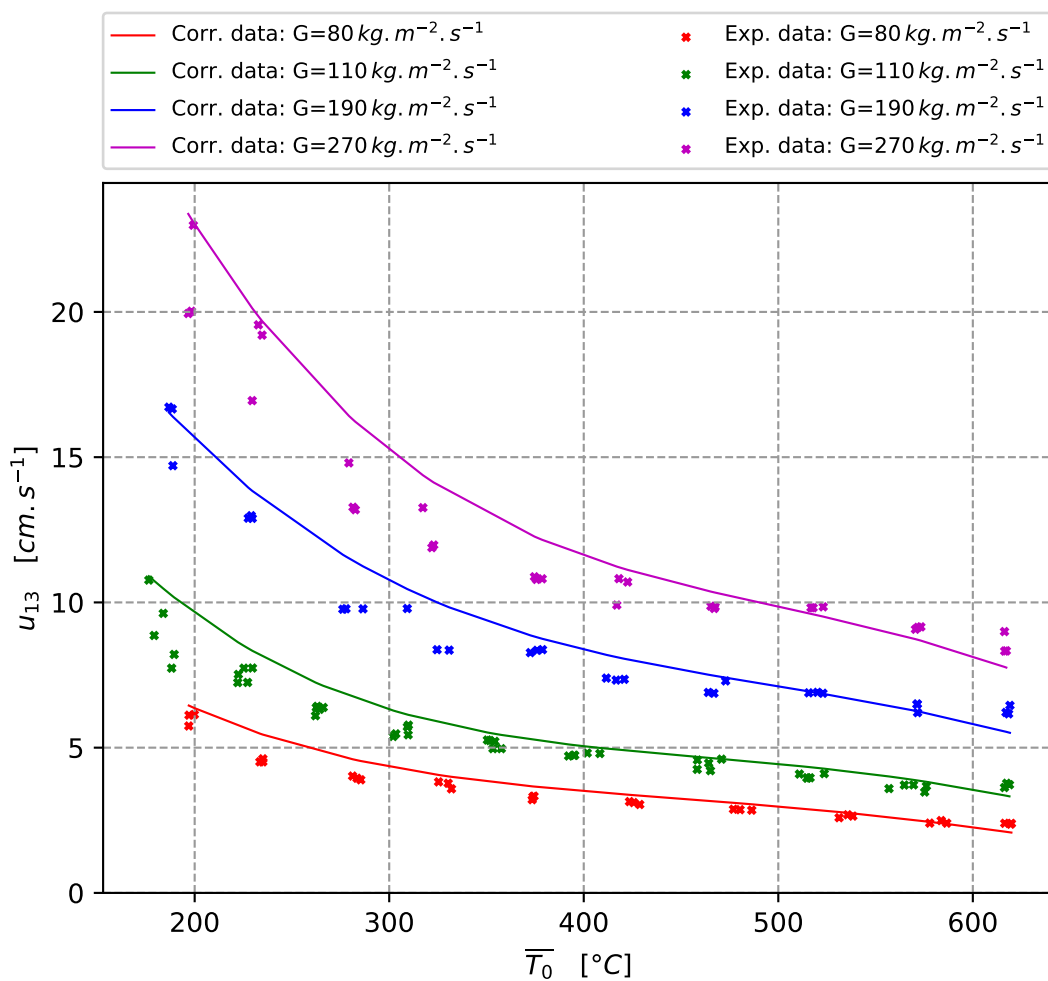
Figure 10.37: Comparison of experimental data and current correlation for Model C

Results showed in Figure 10.37 shows also a very good agreement with experimental

data. Its relative mean average errors are listed in Table 10.4. This model is quite unique so it is not compared to other models. Compared to other two models, the prediction for model C is slightly overestimated especially at higher temperature levels. This is caused by the very different behavior of lower part of the model at low initial wall temperatures.

Table 10.4: RMAE for quench front velocity prediction for Model C

Flow rate $[kg.m^{-2}.s^{-1}]$	RMAE $[\pm\%](P = 68.3\%)$	RMAE $[\pm\%](P = 90\%)$
80	8.8	15.0
110	5.8	9.9
180	9.5	16.2
270	9.2	15.6

10.7 Conclusion

Based on the presented comparison of results from correlation developed in this study with experimental data proves a good agreement with real data. These results were compared to correlation by Saxena, (2001)[56]. The comparison showed good accordance at initial wall temperatures on the level $350 - 500\,°C$. Lower temperatures show overestimated velocities, which is possibly caused by slightly different hydraulic conditions. Overall relative mean absolute error of the presented correlation is about $10\,\%$ and actual error are listed in tables 10.2, 10.3 and 10.4. Presented results are evaluated for the region between thermocouples TC1 $(0.335\,mm)$ and TC3 $(1.335\,mm)$. However, the correlation is capable to predict quench front velocity also for other regions at different axial positions within the range from $0.335\,m$ to $1.335\,m$.

Chapter 11

Recommendations

The experimental part of the study was performed on the testing loop with parameters described in Section 6. As it was mentioned in Section 10.2.1.2, a quenching temperature is not dependent on initial wall temperature from specific initial temperature level. It seems, that the limit temperature is dependent only on actual flow rate and wall thickness. Unfortunately, it is observable only at high initial wall temperatures and low flow rates. For this reason, a new experimental effort has to be done to confirm this hypothesis. This experiment should include temperatures above $700\,^{\circ}C$ and coolant inlet velocities under $5\,cm.s^{-1}$.

The current experimental loop is equipped with annular flow channel with changeable heated models. The main advantage of this technical solution is, that we can visually observe the process and take pictures or video record if needed. On the other hand, an outer barrier such as silica glass tube represents unheated heat conducting wall with poorly estimated influence on the process. A more coherent way how to catch the flooding process is the inverse problem where coolant flows inside the heated tube. Moreover, in the case of the inverse channel, a large number of thermocouples can be positioned along the geometry because they are no more geometrically limited by model from the installation point of view.

Another recommendation is a usage of a different flow meter for high flow rates, due to relatively low scanning frequency in the case of frequency based flow meter. However, the turbine flow meter proved to be very suitable for low flow rates.

Chapter 12

Conclusions

The presented experimental study was focused on the rewetting phenomenon in the annular channel with bottom flooding configuration. Over 400 experiments were performed in order to obtain sufficient information about the process. Results showed the complexity of the process and helped to deepen knowledge of the investigated phenomenon.

Experiments were performed on three electrically heated models (tubes) at ten initial wall temperature levels (from 250 to 700 $°C$), moreover, four flow rate levels were included in these experiments.

The main goal was to collect experimental data and using this data to develop a set of correlations for the description of the flooding process. Based on individual results it can be concluded, that the goal was completely fulfilled with many additional findings.

Experimental data were processed completely with custom-built scripts. These scripts have several key features such as "cascade" algorithm for calculation of heat transfer coefficient behind the quench front, locating the quench front via the second-order derivative of temperature with node heat balance sub-routine. As an output of this basic data processing is converted raw data and over three thousands individual plots describing all relevant measured and calculated variable. On top of that, a superior autonomous batch processing script is capable to manage individually processed data and search through variables and its influence on the investigated parameter for the purpose of correlation development.

The most important results are solutions for quenching and nucleate boiling temperature, which is accompanied by correlations for heat transfer coefficients in the main individual points and regions along the flooded geometry.

Quenching temperature correlation is also main input for the solution of quench front

velocity prediction. A surprising finding related to quench front velocity is, that relative front velocity to inlet velocity of the coolant is not dependent on actual flow rate. It follows that the percentage inlet velocity value can be calculated only through initial wall temperature, quenching temperature, and wall thickness. The quenching temperature is, therefore, most important and the most complex output of the study. The set of correlations developed in this study showed good agreement with acquired experimental data through all models and initial parameters.

In general, quench front velocity decreases with rising initial wall temperature and with more accumulated heat (thicker wall) regardless of flow rate from the relative velocity point of view

Moreover increasing initial wall temperature and flow rate goes with significant pressure pikes. These pressure pikes strongly influence the hydraulic characteristic of the heated channel and this leads to a big pressure drop in the channel. These effects hand in hand with higher quench front velocity at low initial wall temperatures can lead to unevenness of water flow through the core during LOCA. The unevenness can lead to coolant flowing around the central area of the core, where the surface temperature is higher, and the central area of the core can be cooled down distinctly later. On the other hand, geometrical elements, such as spacer grids, create secondary quench fronts moving along the fuel rod. Due to these secondary quench fronts, the last rewetted point can't be clearly determined. In other words, the water presence above the core doesn't mean that the rest of the core is rewetted and cooled down. [A2]

As a side product of these results is the three-regional model which can be used as an input for further analytical studies in the field.

Chapter 13

Future Work and Remarks

Presented study and final recommendations give a solid base for future experimental efforts in the field. The results of the study are not only given correlations and detailed view on the rewetting phenomenon, but also a reasonable approach for experiment setup and data evaluation. The methodology and the processing logic are described in detail in the study and all acquired data and evaluation python scripts are provided on the optical disc.

All outlined goals were fulfilled and these beneficial results are:

- New experimental loop with $1.7\,m$ high test section

- Large number of new experimental data for a wide range of initial wall temperatures, flow rates, and wall thickness

- Set of new, fully automated scripts for data processing, with custom-built correlation script

- Improved detection of important temperature points and data approximation/filtration

- Heat transfer coefficients for every measured point throughout the time-spatial scale

- Correlations for HTC at important temperature points (quenching, critical heat flux, nucleate boiling)

- Correlations for HTC within each region between important temperature points

- Correlations for quenching and nucleate boiling temperature

- Suggestion of three regional rewetting model

- All-embracing quench front velocity correlation

- Pointed out the effect of pressure peaks

- Briefly described the effect of spacers

Moreover, the experimental study has several side benefits, that could help to improve efforts in the field in the future. The main resulting remarks are listed below.

- Experimental part

    - Thermocouple placement within the wall gives the best view on the wall temperature

    - Direct electrical current heating is an easy and suitable method of wall heating

    - Turbine flow meter is easily readable and sufficient method for flow rate measuring

    - Spacers are an integral part of the process and their positioning must take this in mind

- Data evaluation part

    - The maximum second order derivative of the surface temperature is the clearly determined point of the rewetting onset

    - Analogically, the minimum second order derivative of the surface temperature is the nucleate boiling point

    - The Piecewise Cubic Hermite Interpolating Polynomial (PCHIP) is the best method for data interpolation due to its conservation of data features without overestimation near edges

    - Proposed cascade algorithm gives good results of coolant temperature in the wett region

    - Developed custom-built correlation script is comfortable and easy to understand way how to correlate complex data

Chapter 14

References

[1] K. J. Baumeister and F. F. Simon. "Leidenfrost Temperature - Its Correlation for Liquid Metals, Cryogens, Hydrocarbons and Water". In: *ASME Journal of Heat Transfer* 95 (1973), pp. 166–173.

[2] R. Karyampudi and W.Y. Chon. "Effect of Thermal Radiation of Top Spray Emergency Coolant". In: *Nuclear Engineering and Design* 36 (1976), pp. 27–36.

[3] D.C. Groenveld and C.W. Snoek. "A Comprehensive Examination Heat Transfer Correlations Suitable for Reactor Safety Analysis". In: *Nuclear Multiphase Science and Technology* 2 (1986), pp. 181–271.

[4] S. Nukiyama. "The Maximum and Minimum Values of the Heat Q Transmitted from Metal to Boiling Water under Atmospheric Pressure". In: *Journal Japan Soc. Mech. Engrs* 37 (1934), pp. 367–374.

[5] N.E. Todreas and M. Kazimi. *Nuclear Systems Volume I.: Thermal Hydraulic Fundamentals*. CRC Press, 2011, p. 68. ISBN: 978-1560320517.

[6] K.H. Sun, G.E. Dix, and C.L. Tien. "Effect of Precursory Cooling on Falling Film Rewetting". In: *Journal of Heat Transfer, ASME, Series C* 97 (1975), p. 360.

[7] G. Hache and H.M. Chung. "The History of LOCA Embrittlement Criteria". In: *28th Water Reactor Safety Information Meeting*. Bethesda, 2001, pp. 1–32.

[8] S.K. Sahu, P.K. Das, and S. Bhattacharyya. "Analytical and Semi-Analytical Models of Conduction Controlled Rewetting, A State-of-the-Art Review". In: *THERMAL SCIENCE* 19.5 (2015), pp. 1479–1496.

[9] E. Elias and G. Yadigaroglu. "A General One Dimensional-Model for Conduction-Controlled Rewetting of a Surface". In: *Nuclear Engineering and Design* 42 (1977), pp. 185–194.

[10] R. Semeria and B. Martinet. "Calcification Spots on a Heating Wall:Temperature Distribution and Resorption". In: *Proceedings, Institute of Mechanical Engineers* 180 (1965), pp. 192–205.

[11] A. Yamanouchi. "Effect of Core Spray Cooling in Transient State After Loss of Coolant Accident". In: *Journal of Nuclear Science and Technology* 5 (1968), pp. 547–558.

[12] D. Andréoni. "Eschanges Thermiques Lors du Renoyage d'un Coeur de Reacteur à Eaudans le Cadre de l'Accident". PhD thesis. National polytechnique de Grenoble, 1975, pp. 137–141 (IV.29).

[13] C. L. Tien and L. S. Yao. "Analysis of conduction-controlled rewetting of a vertical surface". In: *ASME J. Heat Transfer* 97 (1975), pp. 161–165.

[14] K.H. Sun, G.E. Dix, and C.L. Tien. "Cooling of a Very Hot Vertical Surface by a Falling Liquid Film". In: *Journal of Heat Transfer, ASME, Series C* 96.2 (1974), p. 126.

[15] S. Olek. "On the Two Region Rewetting Model with a Step Change in the Heat Transfer Coefficient". In: *Nuclear Engineering and Design* 108 (1988), pp. 315–322.

[16] M.H. Chun and W.Y. Chon. "Analyses of Rewetting in Water Reactor Emergency Core Cooling Inclusive of Heat Transfer in the Unwetted Region". In: *ASME Winter Annual Meeting*. Vol. 30. 75. Houston, 1975, pp. 1 nn.

[17] P. Case et al. "The Rewetting Process of Hot Surfaces by Bottom Flooding". In: *European Two-Phase Flow Group Meeting at Brussels*. Brussel, 1973, pp. 1 nn.

[18] M. Ishii. "Study on Emergency Core Cooling". In: *J. British Nuclear Energy Society* 14 (1975), pp. 237–242.

[19] A.W. Bennett et al. *The Wetting of Hot Surfaces by Water in a Steam Environment at High Pressure*. Tech. rep. Harwell, England: Atomic Research Establishment, 1966, pp. 1 nn.

[20] T.S. Thompson. "An Analysis of the Wet-Side Heat Transfer Coefficient During Rewetting of a Hot Dry Patch". In: *Nuclear Engineering and Design* 22.2 (1972), p. 212.

[21] R. B. Duffey and D.T.C. Porthouse. "Experiments on the Cooling of High Temperature Surfaces by Water Jets and Drops". In: *Proceedings CREST Specialist Meeting on ECC in LWRs*. Vol. 1. Munich, 1972, pp. 1 nn.

[22] E. Elias and P. Chambré. "The Development of a Cooling Wave on a Hot Surface". In: *Nuclear Engineering and Design* 55 (1979), pp. 9–15.

[23] R. B. Duffey and D.T.C. Porthouse. "The Physics of Rewetting in Water Reactor Emergency Core Cooling". In: *Nuclear Engineering and Design* 25 (1973), pp. 379–394.

[24] B.D.G. Piggott and D.T.C. Porthouse. *Water Reactor Emergency Core Cooling: The Effect of Pressure, Subcooling and Surface Condition on the Rewetting of Hot Surfaces*. Tech. rep. RD/B/N2692. Gloucestershire, England: Berkeley Nuclear Laboratories, 1973, pp. 1 nn.

[25] G.F. Hewitt, J.M. Delhaye, and N. Zuber. "Post/Dryout Heat Transfer". In: *Multiphase Science and Technology* (2000), pp. 39 nn.

[26] M. Salcudean, T.M. Bui, and Y. Lee. "A Three-Dimensional Analysis for the Rewetting Process of Hot Channels". In: *ASME Winter Annual Meeting*. San Francisco, 1978, pp. 1 nn.

[27] M. Salcudean and M. Rahman. "Analytical Solution for the Heat Conduction During Rewetting of Hot Horizontal Channels". In: *Trans. CSME* 6 (1980), pp. 106–114.

[28] M. Sawan and H. Temraz. "A Three-Region Semi-Analytical Rewetting Model". In: *Nuclear Engineering and Design* 64 (1981), pp. 319–327.

[29] H. Bonakdar and Jr. E. V. McAssey. "A Method for Determining Rewetting Velocity Under Generalized Boiling Conditions". In: *Nuclear Engineering and Design* 66 (1981), pp. 7–12.

[30] C.H. Hsu, C. H. Chieng, and T. Hua. "Two-Dimensional Analysis of Conduction Controlled Rewetting with Internal Heat Generation". In: *4th International Conference on Numerical Methods in Engineering*. 1983, pp. 176–200.

[31] A.R. Edwards and D.J. Mather. "Some UK Studies Related to the Loss of Coolant Accident". In: *Topical Meeting on Water Reactor Safety* (1973), pp. 720–737.

[32] S.S. Dua and C.L. Tien. "A Generalized Two-Parameter Relationship for Conduction Controlled Rewetting of Hot Vertical Surface". In: *International Journal of Heat Mass Transfer* 20 (1977), pp. 174–176.

[33] M. Hirano and Y. Asahi. "Analysis of Precursory Cooling in Quenching Phenomena". In: *Journal of Nuclear Science and Technology* 17.5 (May 1980), pp. 339–350.

[34] S. Olek. "The Effect of Precursory Cooling no Rewetting of Slab". In: *Nuclear Engineering and Design* 108 (1988), pp. 323–330.

[35] S. Olek. "Wiener-Hopf Technique Solution to a Rewetting Model with Precursory Cooling". In: *Nuclear Engineering and Engineering* 105 (1990), pp. 271–277.

[36] S.H. Chan and W. Zang. "Rewetting Theory and the Dryout Heat Flux of Smooth and Grooved Plates with Uniform Heating". In: *ASME Journal of Heat Transfer* 116 (1994), pp. 73–179.

[37] J.A. Platt et al. "An Analytical Investigation of Transient Effects on Rewetting of Heated Thin Plates". In: *ASME Winter Annual Meeting*. NASA-TM-106120. New Orleans, La. USA, 1993, pp. 145–153.

[38] A. K. Satapathy and R.K. Sahoo. "Rewetting of an Infinite Slab With Uniform Heating Under Quasi-Steady Conditions". In: *Journal of Heat Transfer* 124 (Oct. 2002), pp. 875–880.

[39] S.K. Sahu, P.K. Das, and S. Bhattacharyya. "Rewetting Analysis of Hot Surfaces with Internal Heat Source by the Heat Balance Integral Method". In: *Journal of Heat Transfer* 44.10 (2008), pp. 1247–1256.

[40] M. Sawan et al. "A Three-Regions Rewetting Model with Heat Generation and Sub-Cooling". In: *Atomenergie* 34 (1979), pp. 199–204.

[41] R. K. Bera and A. Chakrabarti. "The Sputtering temperature of a Cooling Cylindrical Rod Without and with Insulated Core in a Two-Fluid Medium". In: *Journal of Australian Mathematical Society, Series B* 38 (1996), pp. 87–100.

[42] S. Olek and Y. Zvirin. "The Effect of Temperature Dependent Properties on the Rewetting Velocity". In: *International Journal of Multiphase Flow* 11 (1985), pp. 577–581.

[43] S.K. Sahu, P.K. Das, and S. Bhattacharyya. "A Three-Region Conduction-Controlled Rewetting Analysis by the Heat Balance Integral Method". In: *International Journal of Thermal Sciences* 48 (2009), pp. 2100–2107.

[44] D. Durack and B. Wendroff. "Computing a Two-Dimensional Quench Front". In: *Nuclear Engineering and Design* 64 (1977), pp. 187–191.

[45] A.W. Gurcak, A. C. Spencer, and T. Porsching. "Implicit Isotherm Migration: A NumericalMethod for the Two Dimensional Quench Front Problem". In: *Nuclear Engineering and Design* 61 (1980), pp. 25–31.

[46] S. Olek and E. Elias. "An Analytical Solution to a Problem with Position Dependent Heat Transfer Coefficient". In: *The 25th Israel Conference on Mechanical Engineering*. 1994, pp. 345–347.

[47] D.V. Evans. "A Note on the Cooling of a Cylinder Entering a Fluid". In: *IMA J. Appl. Math* 33 (1984), pp. 49–54.

[48] R. K. Bera and A. Chakrabarti. "The Sputtering Temperature of a Cooling Cylindrical Rod Without and with an Insulated Core in a Two-Fluid Medium". In: *Journal of Australian Mathematical Society* 38 (1996), pp. 87–100.

[49] S.K. Sahu, P.K. Das, and S. Bhattacharyya. "HOW GOOD IS GOODMAN'S HEAT-BALANCE INTEGRAL METHODFOR ANALYZING THE REWETTING OF HOT SURFACES?" In: *THERMAL SCIENCE* 13.2 (2009). DOI: 10.2298, pp. 97–112.

[50] M.W.E. Coney. "Calculations on the Rewetting of Hot Surfaces". In: *Nuclear Engineering and Design* 31 (1974), pp. 246–259.

[51] J.G.M. Andersen and P. Hensen. *Two-Dimensional Heat Conduction in Rewetting Phenomena*. Tech. rep. NORHAV-D-6. Riso, Denmark: AEC Research Establishment, 1974, pp. 1 nn.

[52] J. M. Blair. "An Analytical Solution to a Two-Dimensional Model of the Rewetting of a Hot Dry Rod". In: *Nuclear Engineering and Design* 32 (1975), pp. 159–170.

[53] H. C. Yeh. "An Analysis of Rewetting of a Nuclear Fuel Rod in Water Reactor Emergency Core Cooling". In: *Nuclear Engineering and Design* 34 (1975), pp. 317–322.

[54] S.K. Sahu, P.K. Das, and S. Bhattacharyya. "A Comprehensive Analysis of Conduction-Controlled Rewetting by the Heat Balance Integral Method". In: *International Journal of Heat Mass Transfer* 49 (2006), pp. 25–26.

[55] G.L. Shires, A.R. Pickering, and P.T. Blacker. *Film Cooling of Vertical Fuel Rods*. Tech. rep. AEEW-R343. UKAEA Reactor Group, 1964, p. 60.

[56] A.K. Saxena, V. Venkat Raj, and V. Govardhana Rao. "Experimental Studies on Rewetting of Hot Vertical Annular Channel". In: *Nuclear Engineering and Design* 208 (2001), pp. 283–303.

[57] S. Cho et al. "Spacer Grid Effects during a Reflood in an Annulus Flow Channel". In: *Journal of Nuclear Science and Technology* 44.7 (2007). doi.10.1080, pp. 967–976.

[58] B.D.G. Piggott and R. B. Duffey. "The quenching of irradiated fuel pins". In: *Nuclear Engineering and Design* 32 (1975), pp. 182–190.

[59] B.D.G. Piggott and D.T.C. Porthouse. "A Correlation of Rewetting Data". In: *Nuclear Engineering and Design* 32 (1975), pp. 171–181.

[60] Y. Lee, W.J. Chen, and D.C. Groenveld. "Rewetting of Very Hot Vertical and Horizontal Channels by Flooding". In: *Proceedings 6th International Heat Transfer Conference*. Vol. 5. 95. Torronto, Aug. 1978, pp. 95–100.

[61] M.K. Chung et al. "Reflood Experiments with Horizontal and Vertical Flow Channels". In: *Journal of the Korean Nuclear Society* 12.3 (1980), pp. 153–162.

[62] S. Neti and J.C. Chen. "Study of Quench Front Velocities in a Reflood Experiment". In: *AIChE Symposium Ser. Heat Transfer*. Milwaukee, 1981, pp. 1 nn.

[63] S.G. Bankoff and N.H. Afgan. *Heat Transfer in Nuclear Reactor Safety*. New York: Mc Graw-Hill, 1982, p. 964.

[64] Y. Lee and W.D. Shen. "Effect of coolant vapour quality on Rewetting Phenomena". In: *International Journal of Heat Mass Transfer* 28 (1985), pp. 139–146.

[65] T.C. De Boer and S.B. Van Der Molen. "Heat Transfer to a Dispersed Two-Phase Flow and Detailed Quench Front Velocity Research". In: *Safety of Thermal Water Reactors* (1985), pp. 135–149.

[66] T. Yonomoto, Y. Koizumi, and K. Tasaka. "Core heat transfer analysis during a BWR LOCA simulation experiment at ROSA-III". In: *Nuclear Engineering and Design* 103 (1987), pp. 239–250.

[67] S. Muto et al. "An experimental study on rewetting phenomenon in transient conditions of BWRs". In: *Nuclear Engineering and Design* 120 (1990), pp. 311–321.

[68] K. Tuzla, C. Unal, and J.C. Chen. "An experimental study of bottom rewetting in a rod bundle geometry". In: *Nuclear Engineering and Design* 125 (1991), pp. 189–200.

[69] Y. Barnea, E. Elias, and I. Shai. "Flow and heat transfer regimes during quenching of hot surfaces". In: *International Journal of Heat Mass Transfer* 37 (1994), pp. 1441–1453.

[70] X.C. Huang, G. Bartsch, and D. Schroeder-Richter. "Quenching experiments with a circular test section of medium thermal capacity under forced convection of water". In: *International Journal of Heat Mass Transfer* 5 (1994), pp. 803–818.

[71] T. Igushi, S. Ohmizu, and Y. Anoda. "Grid Spacer Effect on Reflood Behavior Observed at Reflood Experiment with 5x5 Bundle Test Section Under Wide Pressure Condition". In: *JSME, ICONE-7 proceedings*. 7230. Tokyo, Japan, 1999, p. 4252.

[72] S. Cho et al. "Core Thermal Hydraulic Behavior During the Reflood Phase of Cold-Leg LBLOCA Experiments Using the ATLAS Test Facility". In: *Nuclear Multiphase Science and Technology* 41.10 (2009), pp. 1263–1274.

[73] J. Stuckert et al. "Experimental and calculation results of the integral reflood test QUENCH-14 with M5 cladding tubes". In: *Annals of Nuclear Energy* 37 (2010), pp. 1036–1047.

[74] L.E. Hochreiter et al. *RBHT Reflood Heat Transfer Experiments Data and Analysis*. Tech. rep. NUREG/CR-6980. U.S.NRC, 2012, pp. 7 nn.

[75] N. Lymperea, Nikoglou A., and E.P. Hinis. "An Experimental Study on the Quench Front Velocity and Temperature During Rewetting of a Hot Vertical Rod". In: *NURETH-16*. Chicago, IL, USA, Aug. 2015, pp. 3525–3538.

[76] J. Sigumoto and Y. Murao. "Effect of Grid Spacers on Reflood Heat Transfer in PWR-LOCA". In: *Journal of Nuclear Science and Technology* 21 (1984), pp. 103–114.

[77] S.K. Moon et al. "Spacer Grid Effects on the Heat Transfer Enhancement During a Reflood". In: *9th Int. conf. on Heat Transfer, HEFAT12*. Malta, July 2012, pp. 1729–1736.

[78] Special Metals Corporation. *MONEL alloy K-500*. 2004.

[79] Sandvik Group. *SANDVIK 6R35 Tube and Pipe, Seamless*. www.smt.sandvik.com, 2015.

[80] KEYSIGHT Technologies Inc. *Keysight 34970A Data Acquisition/Switch Family*. www.keysight.com/find/34970A, 2017.

[81]   MathWorks Inc. *Filtering and Smoothing Data*. `https://www.mathworks.com/help/curvefit/smoothing-data.htm`. Accessed: 2018-02-05. 2018.

[82]   Y. Sibamoto et al. "Core Heat Transfer Coefficients Immediately Downstream of the Rewetting Front during Anticipated Operational Occurrences for BWRs". In: *Journal of Nuclear Science and Technology* 48/3 (Jan. 2012), pp. 440–453.

Author's References Related to the Study

A1 J. Stepanek, V. Blaha, V. Dostal, *The Effect of Spacer Grid's Elements on the Rewetting Velocity*, Proceedings of Lemtech - Low Emission Technologies Conference, Prague, Czech Republic, November, (2014), pp:1nn

A2 J. Stepanek, V. Blaha, V. Dostal, P. Burda, *The Effect of Spacer Grid's Elements on the Rewetting Velocity*, Proceedings of Int. conf. ICONE-23, Chiba, Japan, Paper no.1333, doi.10.1299, May, (2015), pp:1nn

A3 J. Stepanek, V. Blaha, V. Dostal, *Quench Front Propagation in the Annular Channel*, ŠIMÁNĚ 2016: Czech-Slovak Student Conference on Nuclear Engineering, Acta Polytechnica CTU Proceedings, Vol.4, (2016), ISSN 2336-5382. ISBN 978-80-01-06069-8, pp:97-101

A4 J. Stepanek, V. Blaha, V. Dostal, S. Entler, *Effective Water Cooling of Very Hot Surfaces During the LOCA Accident*, Fusion Engineering and Design, Vol.124, (2017), doi:10.1016/j.fusengdes.2017.03.150, pp:1211-1214

Author's References Not Related to the Study

B1 J. Štěpánek, V. Železný, *CFD studie vlivu distančních mřížek a turbulizujících lopatek na proudění v experimentálním palivovém svazku s geometrií VVER-1000*, Bezpečnost jaderné energie, No.1/2, Vol.22, issn:1210-7085, (2014), pp:18-21

B2 V. Dostál, V. Petr, M. Kolovratník, T. Dlouhý, R. Škoda, L. Veselý, J. Štěpánek, T. Romsy, O. Burian, P. Zácha, V. Železný, D. Kolčaba, *Development of Supercritical Carbon Dioxide Cycle for Waste Heat Recovery*, Doosan Heavy Industries Co., Ltd., Research Report, pages:140, (2015)

B3 J. Štěpánek, *Virtuální Cenelín*, Technicall, url: https://issuu.com/tecnicall2012/docs/2015_2, Vol.2, pp:20, August, (2015)

B4 R. Škoda, J. Škarohlíd, J. Štěpánek, P. Zácha, V. Železný, V. Dostál, L. Veselý, *ATHR cycle optimisation*, North West University, South African Republic, Research Report, pages:37, (2016)

B5 J. Štěpánek, L. Veselý, V. Dostál, *Supercritical Carbon Dioxide Heat Cycle Optimization Code*, Software, url: http://energetika.cvut.cz/RIV/software, (2016)

B6 L. Veselý, V. Dostál, J. Štěpánek, *Effect of Gaseous Admixtures on Cycles With Supercritical Carbon Dioxide*, ASME Turbo Expo 2016: Turbomachinery Technical Conference and Exposition, Vol.9, (2016), doi:10.1115/GT2016-57644, isbn:978-0-7918-4987-3, pp:459–467

B7 J. Štěpánek, R. Škoda, *Optimization of electron beam irradiation at HELCZA experiment*, Fusion Engineering and Design, Vol.124, (2017), doi:10.1016/j.fusengdes.2017.03.149, issn:0920-3796, pp:321-323

B8 P. Zácha, L. Veselý, J. Štěpánek, *Design of the divertor targets shielding frame of the HELCZA high heat flux experimental complex*, Fusion Engineering and Design, Vol.124, (2017), doi:10.1016/j.fusengdes.2017.03.019, issn:0920-3796, pp:360-363

Chapter 15

Appendix

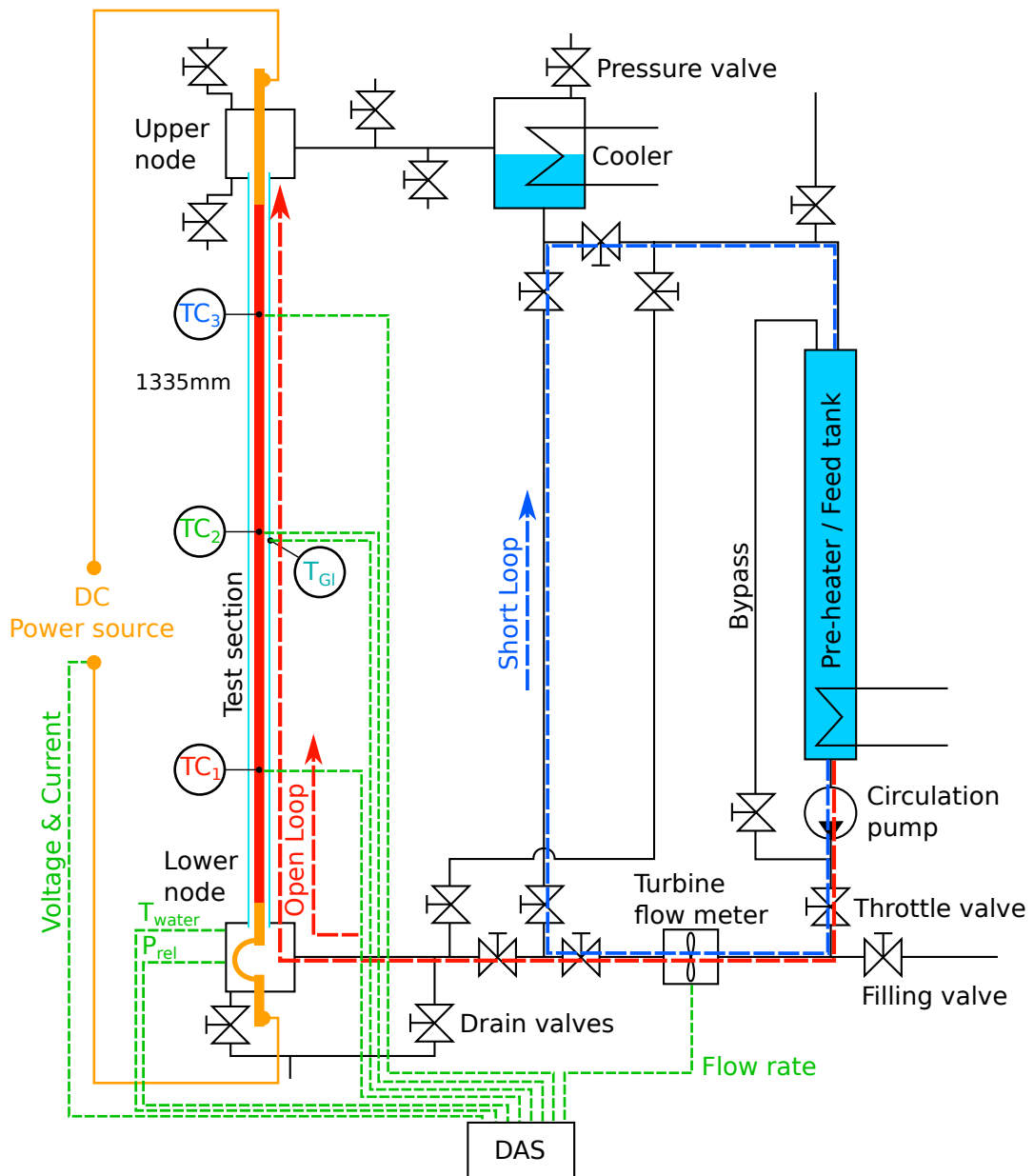## 15.1 Full Experimental Loop Scheme

Figure 15.1: Experimental loop scheme

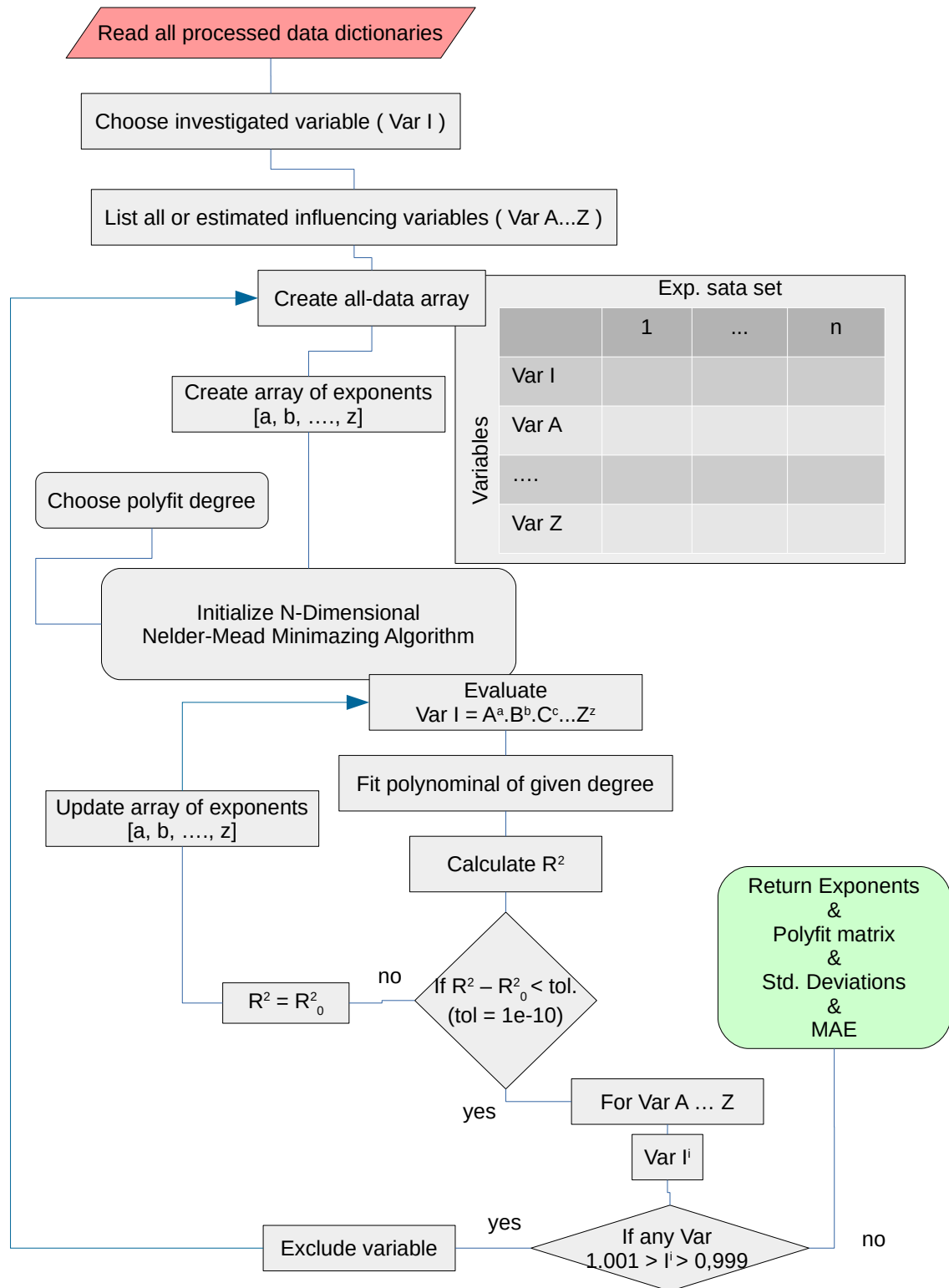## 15.2   Correlation Custom-Built Script

Figure 15.2: Self-Operational correlation algorithm simplified scheme